

SYNGAS PRODUCTION OVER REDUCIBLE METAL OXIDES

A THESIS SUBMITTED TO
THE GRADUATE SCHOOL OF NATURAL AND APPLIED SCIENCES
OF
MIDDLE EAST TECHNICAL UNIVERSITY

BY

ATALAY ÇALIŞAN

IN PARTIAL FULFILLMENT OF THE REQUIREMENTS
FOR
THE DEGREE OF MASTER OF SCIENCE
IN
CHEMICAL ENGINEERING

JANUARY 2013

Approval of thesis:

SYNGAS PRODUCTION OVER REDUCIBLE METAL OXIDES

submitted by **ATALAY ÇALIŞAN** in partial fulfillment of the requirements for the degree of **Master of Science in Chemical Engineering Department, Middle East Technical University** by,

Prof. Dr. Canan Özgen
Dean, Graduate School of **Natural and Applied Sciences**

Prof. Dr. Deniz Üner
Head of Department, **Chemical Engineering**

Prof. Dr. Deniz Üner
Supervisor, **Chemical Engineering Dept., METU**

Examining Committee Members:

Prof. Dr. Güngör Gündüz
Chemical Engineering Dept., METU

Prof. Dr. Deniz Üner
Chemical Engineering Dept., METU

Prof. Dr. Saim Özkar
Chemistry Dept., METU

Assoc. Prof. Dr. Halil Kalıpçılar
Chemical Engineering Dept., METU

Dr. Harun Koku
Chemical Engineering Dept., METU

Date: 25.01.2013

I hereby declare that all information in this document has been obtained and presented in accordance with academic rules and ethical conduct. I also declare that, as required by these rules and conduct, I have fully cited and referenced all material and results that are not original to this work.

Name, Last name: Atalay ÇALIŞAN

Signature :

ABSTRACT

SYNGAS PRODUCTION OVER REDUCIBLE METAL OXIDES

Çalışan, Atalay
M. Sc. Department of Chemical Engineering
Supervisor: Prof. Dr. Deniz Üner

January 2013, 106 pages

The scope of this thesis was to study thermodynamics of lead oxide and cobalt oxide as the chemical looping agent for oxygen. Furthermore, the theoretical results were verified experimentally. Ellingham diagrams were constructed for the selected oxides. Then, detailed thermodynamic analysis was conducted for stability analysis at different temperatures and pressures. Equilibrium product compositions for various reactions involving these oxides were calculated via Gibbs free energy minimization analysis. Finally, it was shown that cobalt, lead and their oxide forms can be used for syngas production.

In the experimental part PbOx, CoOx, Pt-doped CoOx and Pt-doped cobalt alumina, and mixed lead cobalt oxides were synthesized. In addition, technical grade cobalt oxide and lead rods were also used. XRD analysis indicated that Co₃O₄, Pb₂O₃ and α-PbO were the main crystal structures. Oxygen evolution from mixed oxides was monitored by TPD in a home built system. Re-oxidation of the reduced metals was successfully conducted using CO₂ and H₂O as oxidizing agents. Oxygen TPD studies indicated that oxygen evolution rates and amounts were higher and started at lower temperatures when two oxides were together. These observations were consistent with the predictions obtained from thermodynamics. In a series packed bed reactor, evolved oxygen from the mixed oxides were used to react with coal packed upstream of the oxides. It was found that coal oxidation can be achieved around 400°C and 600°C by using Pb/Co=3 (wt./wt.) looping media with almost no CO₂ formation. It was also found that desired product selectivity (CO) can be increased by controlling reactive agent (O₂) concentration in reaction environment.

Keywords: Syngas, thermodynamic analysis, coal oxidation, metal oxide, lead oxide, cobalt oxide

ÖZ

İNDİRGENEBİLİR METAL OKSİTLERDEN SENTEZ GAZI ELDESİ

Çalışan, Atalay
Yüksek Lisans, Kimya Mühendisliği Bölümü
Tez Yöneticisi: Prof. Dr. Deniz Üner

Ocak 2013, 106 sayfa

Bu tez kapsamında kobalt oksit ve kurşun oksitin oksijen için kimyasal döngü maddesi olarak kullanımının termodinamik analizi çalışılmıştır. Yapılan teorik çalışmalar deneysel olarak da doğrulanmıştır. Seçilen oksitler için Ellingham diyagramları oluşturulmuştur. Daha sonra, seçilen oksitlerin değişik sıcaklıklarda ve basınçlarda stabilite analizleri detaylı termodinamik analizlerle gerçekleştirilmiştir. Çalışılan bu oksitlerin değişik reaksiyonlar sonucunda oluşturdukları ürün dağılımı dengede Gibbs serbest enerji metodu ile hesaplanmıştır. Yapılan bu çalışma sonunda kobalt, kurşun ve bu metallerin oksit formlarının sentez gazı üretiminde kullanılabileceği gösterilmiştir.

Deneysel çalışmaların yapıldığı bölümde, PbOx, CoOx, Pt-yüklenmiş CoOx ve Pt-yüklenmiş kobalt alumina, ve kurşun kobalt alaşım oksitleri sentezlenmiştir. Sentezlenen maddelere ek olarak, teknik saflıkta kobalt oksit ve kurşun çubuklar kullanılmıştır. XRD çalışmaları, kullanılan oksitlerin kristal yapılarının çoğunlukla Co₃O₄, Pb₂O₃ ve α-PbO oluştuğunu göstermiştir. Bu oksitlerin yapılarından sıcaklığa bağlı oksijen salma deneyleri ev yapımı bir sistemde gerçekleştirilmiştir. İndirgenmiş metal oksitler CO₂ ve H₂O ile başarıyla tekrar oksitlenmiştir. Sıcaklığa bağlı oksijen salma deneyleri, iki metal oksit çiftinin beraber kullanıldığında oksijen salma hızı ve salınan oksijen miktarının yükseldiğini, ayrıca oksijen salınımının düşük sıcaklıkta başladığı görülmüştür. Bu bulgular termodinamik çalışmalardan elde edilen varsayımlarla tutarlı olduğu bulunmuştur. Seri dolgulu yatak reaktörü ile sıcaklıkla ilk dolguda yer alan metal oksitin yapısından ayrılan oksijenin ikinci dolguda yer alan kömürün oksidasyonunda kullanılmıştır. Kömür oksitlenmesinin, Pb/Co=3 (wt./wt.) alaşım oksiti kullanılarak 400°C ve 600°C'lerde neredeyse hiç CO₂ oluşumu olmadan gerçekleşebileceği bulunmuştur. Ayrıca istenen ürün seçimliliğinin (CO), reaksiyon ortamında yer alan reaktif maddenin (O₂) konsantrasyonunun kontrol edilerek artırılabilceği de gösterilmiştir.

Anahtar Kelimeler: Sentez gazı, termodinamik analiz, kömür oksidasyonu, metal oksit, kurşun oksit, kobalt oksit

To my family

ACKNOWLEDGEMENTS

I would like to thank my supervisor Prof. Dr. Deniz Üner for providing and sustaining an environment where my ideas could flourish and where independence was encouraged.

I want to thank all former members of CACTUS Research Group. Main body of this thesis never will be theorized without their sleepless nights. I also wish to express my great appreciations to present members: İbrahim Bayar, Nevzat Can Aksu, Necip Berker Üner, Mustafa Yasin Aslan, Arzu Kanca, Mert Mehmet Oymak, and Hale Ay.

I would like to thank my bros; Güvenç Celal Oğulğönen, Onur Erdem, Gökhan Çelik, Okan Özkök, Halime Gül Zerze (Özer), Turan Çağrı Arı, Görkem Türkili, Ufuk Kılıçarslan, Hasan Sezgi Yürüt and Mehmet Can Pakdil for never letting me down through my life.

The technical staff of our department Süleyman Nazif Kuşhan, Ertuğrul Özdemir, Adil Demir and İsa Çağlar were greatly appreciated for their expertise in reactor manufacturing.

The Scientific and Research Council of Turkey (TUBITAK) are kindly acknowledged for 2210 M.Sc. scholarship and financial support during my graduate study.

My deepest gratitude, coming from my soul, are to my parents, my sister, my blood brother Can Aydın and last but not the least to my wife, Deniz. Their unlimited love, support, and confidence in me throughout my life made me who I am now.

TABLE OF CONTENTS

ABSTRACT.....	v
ÖZ.....	vi
ACKNOWLEDGEMENTS.....	viii
TABLE OF CONTENTS.....	ix
LIST OF TABLES.....	xi
LIST OF FIGURES.....	xii
CHAPTERS	
1. INTRODUCTION AND OBJECTIVE.....	1
1.1. Coal Gasification Technology.....	2
1.2. Chemical Looping Systems.....	7
1.3. Objectives.....	8
2. LITERATURE SURVEY.....	9
2.1. Gasification.....	9
2.2. Mechanism.....	10
2.3. Bond Dissociation Energies.....	11
2.4. Sulfur Effect on Reactivity.....	11
2.5. Catalyst Research.....	13
2.5.1. Conventional Processes.....	13
2.5.2. Chemical Looping Processes.....	13
2.6. Phase Diagrams.....	13
2.7. Thermal Decomposition.....	17
3. MATERIALS AND METHODS.....	19
3.1. Thermodynamic Analysis.....	19
3.1.1. Ellingham Diagrams.....	19
3.1.2. Predominance Diagrams.....	19
3.1.3. Gibbs Free Energy Minimization Analysis.....	20
3.2. Experimental Methods.....	22
3.2.1. Synthesis Methodology.....	22
3.2.1.1. Bulk Lead Oxide Synthesis.....	23
3.2.1.2. Bulk Cobalt Oxide Synthesis.....	23
3.2.1.3. Bulk Cobalt Oxide and Lead Oxide Synthesis.....	23
3.2.1.4. Pt doped Cobalt Oxide Synthesis.....	23
3.2.1.5. γ -Al ₂ O ₃ supported Cobalt Oxide Synthesis.....	23
3.2.1.6. Pt doped γ -Al ₂ O ₃ supported Cobalt Oxide Synthesis.....	23
3.2.2. Synthesized Material Characterization.....	24
3.2.3. Visual Observation Experiments.....	24
3.2.4. FT-IR Experiments.....	24
3.2.5. Temperature Programmed Desorption (TPD) Experiments.....	26
3.2.5.1. Coal Oxidation Experiments.....	26
4. RESULTS.....	27
4.1. Thermodynamic Analysis.....	27
4.1.1. Ellingham Diagrams.....	27
4.1.2. Predominance Diagrams.....	30
4.1.2.1. Metal Oxide Stability.....	30
4.1.2.2. Metal/Metal Oxide stability at CO ₂ /CO atmosphere.....	32
4.1.2.3. Stability of Sulfur containing Compounds.....	35
4.1.3. Energy Analysis.....	40
4.1.4. Equilibrium Analysis.....	41
4.1.4.1. C-S-O system.....	41

4.1.4.2.	C-S-O-Pb system.....	44
4.1.4.3.	C-S-O-Co system	48
4.1.4.4.	C-S-O-Fe system	51
4.2.	Experimental Results.....	51
4.2.1.	Visual Observation Experiments	53
4.2.2.	CO ₂ Reduction Experiments.....	54
4.2.3.	Coal Oxidation via Reducible Metal Oxides	54
4.2.3.1.	Characterization	55
4.2.3.1.1.	Coal Characterizations	55
4.2.3.1.2.	Metal Oxide Characterization.....	56
4.2.4.	Coal Oxidation Experiments	56
5.	DISCUSSIONS.....	61
6.	SUMMARY AND CONCLUSIONS.....	65
	REFERENCES	66
	APPENDICES	
A.	CONSTRUCTION OF PHASE STABILITY DIAGRAMS	68
B.	MATLAB CODE FOR GIBBS FREEE ENERGY MINIMIZATION	77
C.	GIBBS FREEE ENERGY MINIMIZATION RESULTS	79
D.	REACTOR DESIGN.....	96
E.	VISUAL ANALYSIS OF LEAD OXIDATION.....	98
F.	MASS SPECTROMETRY EXPERIMENTS	99
G.	TPD ANALYSIS.....	103

LIST OF TABLES

TABLES

Table 1: Classification of syngas in terms of energy content [1].....	1
Table 2: Comparison of coal gasification technologies [1]	6
Table 3: Current large scale demonstration plants	7
Table 4: Main gasification reactions.....	9
Table 5: Bond dissociation energies of certain molecules at 298K [11]	12
Table 6: Enthalpies of lead oxide decomposition reactions	40
Table 7: Enthalpies of cobalt oxide decomposition reactions.....	41
Table 8: Equilibrium analysis of C-S-O system	41
Table 9: Compounds expected to be in equilibrium for C-S-O-Pb.....	45
Table 10: Compounds expected to be in equilibrium for C-S-O-Co	47
Table 11: Compounds expected to be in equilibrium for C-S-O-Pb.....	50
Table 12: Proximate analysis.....	55
Table 13: Ultimate Analysis	55
Table 14: Thermal decomposition analysis of selected materials by TPD	57
Table 15: Gasification reaction results for performed looping material	57
Table G 2: Performance analysis of all looping material	106

LIST OF FIGURES

FIGURES

Figure 1: Syngas production via fossil fuel gasification processes [1].....	2
Figure 2: Equilibrium compositions at different temperatures and pressures [1]	3
Figure 3: Fixed bed coal gasification processes operating principles [1].....	4
Figure 4: Fluidized bed coal gasification processes operating principles [1].....	4
Figure 5: Entrained bed coal gasification processes operating principles [1]	5
Figure 6: Molten-metal-bath coal gasification processes operating principles [1].....	5
Figure 7: Chemical looping systems from raw materials to end products [4].....	8
Figure 8: Chemical looping systems; (a) Oxygen Carrier, (b) CO ₂ Carrier	8
Figure 9: Mass transport mechanism expected during coal gasification.....	10
Figure 10: Pb-O phase diagram [34]	14
Figure 11: Co-O phase diagram [35]	15
Figure 12: Fe/S phase diagram. [36]	15
Figure 13: Co/S phase diagram [36]	16
Figure 14: Pb/S phase diagram [37].....	16
Figure 15: Visual observation experimental design	24
Figure 16: Experimental setup used for FT-IR measurement.	25
Figure 17: Thermal decomposition reactions experimental design.....	25
Figure 18: Coal oxidation experiment setup	26
Figure 19: Relative oxidative strengths of some metal oxides at 1 bar.	28
Figure 20: Oxidative strengths of metal oxides when Me/O=0.75 at 1 bar.....	28
Figure 21: Oxidative strengths of generally available lead oxides and cobalt oxides at 1bar.	29
Figure 22: P(O ₂) vs. T diagram for Pb-O systems at 1bar.....	29
Figure 23: P(O ₂) vs. T diagrams for Co-O systems at 1bar.....	31
Figure 24: Fe/CO ₂ /CO system at 400°C and 1bar	31
Figure 25: Fe/CO ₂ /CO system at 700°C and 1bar	32
Figure 26: Pb/CO ₂ /CO system at 400°C and 1bar	33
Figure 27: Pb/CO ₂ /CO system at 700°C and 1bar	33
Figure 28: Co/CO ₂ /CO system at 400°C and 1bar	34
Figure 29: Co/CO ₂ /CO system at 700°C and 1bar	34
Figure 30: Predominance diagram for Fe-S-O system at 400°C and 1 bar.....	35
Figure 31: Predominance diagram for Fe-S-O system at 700°C and 1 bar	36
Figure 32: Predominance diagram for Fe-S-O system at P _{O₂} =0.21bar.....	36
Figure 33: Predominance diagram for Co-S-O system at 400°C and 1 bar.....	37
Figure 34: Predominance diagram for Co-S-O system at 700°C and 1 bar.....	37
Figure 35: Predominance diagram for Co-S-O system at P _{O₂} =0.21bar	38
Figure 36: Predominance diagram for Pb-S-O system at 400°C and 1 bar	39
Figure 37: Predominance diagram for Pb-S-O system at 700°C and 1 bar	39
Figure 38: Predominance diagram for Pb-S-O system at P _{O₂} =0.21bar	40
Figure 39: Equilibrium composition of a system of 1 mol C, 0.05 mol S and 0.5 mol O at 0.1 bars.	42
Figure 40: Equilibrium composition of a system of 1mol C, 0.05 mol S and 0.5 mol O at 1 bar	42
Figure 41: Equilibrium composition of a system of 1mol C, 0.05 mol S and 0.5 mol O at 10 bars	43
Figure 42: Equilibrium composition of a system of 1mol C, 0.05 mol S and 1mol O at 1 bar	43
Figure 43: Equilibrium composition of a system of 1mol C, 0.05 mol S and 3 mol O at 1 bar	44
Figure 44: Equilibrium composition of a system of 1mol C, 0.05mol S, 0.5mol Pb and 0.5mol O at 1bar	45
Figure 45: Equilibrium composition of a system of 1mol C, 0.05 mol S, 1mol Pb and 1mol O at 1 bar	46
Figure 46: Equilibrium composition of a system of 1mol C, 0.05 mol S, 3mol Pb and 3mol O at 1 bar	46

Figure 47: Equilibrium composition of a system of 1mol C, 0.05 mol S, 0.5mol Co and 0.5mol O at 1 bar	47
Figure 48: Equilibrium composition of a system of 1mol C, 0.05 mol S, 1mol Co and 1mol O at 1 bar	48
Figure 49: Equilibrium composition of a system of 1mol C, 0.05 mol S, 3mol Co and 3mol O at 1 bar	49
Figure 50: Equilibrium composition of a system of 1mol C, 0.05 mol S, 0.5mol Fe and 0.5mol O at 1 bar	49
Figure 51: System of 1mol C, 0.05 mol S, 1mol Fe and 1mol O at 1 bar	50
Figure 52: Equilibrium composition of a system of 1mol C, 0.05 mol S, 3mol Fe and 3mol O at 1 bar	51
Figure 53: Metallic lead oxidation in air atmosphere from 20°C to 800°C.	52
Figure 54: Metallic lead oxidation in air (left) and steam (right) atmosphere at 700°C.	53
Figure 55: CO formation band at different temperatures.	54
Figure 56: XRD characterization of PbOx, CoOx, Pb/Co=3 (wt./wt.) and 1wt.Pt% CoOx(5.5wt%)-Al ₂ O ₃	56
Figure 57: Results of thermal decomposition experiments (A); CO ₂ formation during coal oxidation experiments (B); CO formation during coal oxidation experiments (C)	58
Figure 58: Suggested scheme for syngas production via cobalt and lead oxide.....	63
Figure A 1: Equilibrium partial pressures of oxygen for Reactions 1 to 6.....	70
Figure A 2: Pb/PbO stability diagram.	70
Figure A 3: Equilibrium partial pressures of oxygen for Reactions 1 and 7 to 11.	71
Figure A 4: Stability patterns of Reactions 1, 7 to 9.	71
Figure A 5: Pb/PbO/Pb ₃ O ₄ /Pb ₁₂ O ₁₇ /Pb ₂ O ₃ stability diagram.	72
Figure A 6: Stability patterns of Reactions 1, 7 to 9 and 12 to 15.....	73
Figure A 7: Pb/PbO/Pb ₃ O ₄ stable region (raw figure).....	73
Figure A 8: Pb/PbO/Pb ₃ O ₄ stable region after trimming extra lines	74
Figure A 9: Stability patterns of Reactions 16 to 18	74
Figure A 10: Pb/PbO/Pb ₃ O ₄ /Pb ₁₂ O ₁₇ /Pb ₂ O ₃ stability diagram	75
Figure A 11: Stability patterns of Reactions 19 to 21.	75
Figure A 12: Stability diagram of lead/lead oxide compounds	76
Figure C 1: Equilibrium composition of a system of C=1mol; S=0.05mol; O=0.5mol at 0.1bar	79
Figure C 2: Equilibrium composition of a system of C=1mol; S=0.05mol; O=0.5mol at 1bar	80
Figure C 3: Equilibrium composition of a system of C=1mol; S=0.05mol; O=0.5mol at 10bar	80
Figure C 4: Equilibrium composition of a system of C=1mol; S=0.05mol; O=1mol at 0.1bar	81
Figure C 5: Equilibrium composition of a system of C=1mol; S=0.05mol; O=1mol at 1bar	81
Figure C 6: Equilibrium composition of a system of C=1mol; S=0.05mol; O=1mol at 10bar	82
Figure C 7: Equilibrium composition of a system of C=1mol; S=0.05mol; O=3mol at 0.1bar, 1 bar and 10bar.....	82
Figure C 8: Equilibrium composition of a system of C=1mol; S=0.05mol; O=0.5mol; Pb=0.5mol at 0.1bar	83
Figure C 9: Equilibrium composition of a system of C=1mol; S=0.05mol; O=0.5mol; Pb=0.5mol at 1bar	83
Figure C 10: Equilibrium composition of a system of C=1mol; S=0.05mol; O=1mol; Pb=1mol at 0.1bar	84
Figure C 11: Equilibrium composition of a system of C=1mol; S=0.05mol; O=1mol; Pb=1mol at 1bar	84
Figure C 12: Equilibrium composition of a system of C=1mol; S=0.05mol; O=1mol; Pb=1mol at 10bar	85
Figure C 13: Equilibrium composition of a system of C=1mol; S=0.05mol; O=3mol; Pb=3mol at 0.1bar	85
Figure C 14: Equilibrium composition of a system of C=1mol; S=0.05mol; O=3mol; Pb=3mol at 1bar	86
Figure C 15: Equilibrium composition of a system of C=1mol; S=0.05mol; O=3mol; Pb=3mol at 10bar	86

Figure C 16: Equilibrium composition of a system of C=1mol; S=0.05mol; O=0.5mol; Co=0.5mol at 0.1bar	87
Figure C 17: Equilibrium composition of a system of C=1mol; S=0.05mol; O=0.5mol; Co=0.5mol at 1bar	87
Figure C 18: Equilibrium composition of a system of C=1mol; S=0.05mol; O=0.5mol; Co=0.5mol at 10bar	88
Figure C 19: Equilibrium composition of a system of C=1mol; S=0.05mol; O=1mol; Co=1mol at 0.1bar	88
Figure C 20: Equilibrium composition of a system of C=1mol; S=0.05mol; O=1mol; Co=1mol at 1bar	89
Figure C 21: Equilibrium composition of a system of C=1mol; S=0.05mol; O=1mol; Co=1mol at 10bar	89
Figure C 22: Equilibrium composition of a system of C=1mol; S=0.05mol; O=3mol; Co=3mol at 0.1bar	90
Figure C 23: Equilibrium composition of a system of C=1mol; S=0.05mol; O=3mol; Co=3mol at 1bar	90
Figure C 24: Equilibrium composition of a system of C=1mol; S=0.05mol; O=3mol; Co=3mol at 10bar	91
Figure C 25: Equilibrium composition of a system of C=1mol; S=0.05mol; O=0.5mol; Fe=0.5mol at 0.1bar	91
Figure C 26: Equilibrium composition of a system of C=1mol; S=0.05mol; O=0.5mol; Fe=0.5mol at 1bar	92
Figure C 27: Equilibrium composition of a system of C=1mol; S=0.05mol; O=0.5mol; Fe=0.5mol at 10bar	92
Figure C 28: Equilibrium composition of a system of C=1mol; S=0.05mol; O=1mol; Fe=1mol at 0.1bar	93
Figure C 29: Equilibrium composition of a system of C=1mol; S=0.05mol; O=1mol; Fe=1mol at 1bar	93
Figure C 30: Equilibrium composition of a system of C=1mol; S=0.05mol; O=1mol; Fe=1mol at 10bar	94
Figure C 31: Equilibrium composition of a system of C=1mol; S=0.05mol; O=3mol; Fe=3mol at 0.1bar	94
Figure C 32: Equilibrium composition of a system of C=1mol; S=0.05mol; O=3mol; Fe=3mol at 1bar	95
Figure C 33: Equilibrium composition of a system of C=1mol; S=0.05mol; O=3mol; Fe=3mol at 10bar	95
Figure D 1: Technical drawing and manufactured picture of Reactor A.....	96
Figure D 2: Technical drawing and manufactured picture of Reactor B.....	97
Figure E 1: Water oxidation experiment with Reactor A.....	98
Figure F 1: MS setup for discontinuous experiment	100
Figure F 2: CO ₂ reduction as temperature increases.....	101
Figure F 3: Thermal Decomposition of lead oxide formed by CO ₂ reduction experiment.	102
Figure G 1: X-ray diffraction data of technical grade and synthesized cobalt oxides.	103
Figure G 2: X-ray diffraction data of synthesized lead oxide, cobalt oxide and their mixed oxides.	104
Figure G 3: Thermal decomposition of synthesized cobalt based looping material.....	105
Figure G 4: Thermal decomposition of synthesized Pb/Co mixed looping material.	105

CHAPTER 1

INTRODUCTION AND OBJECTIVE

Synthetic gas (syngas) is a gas mixture composed of CO and H₂. It is an important feedstock for production of high-value added chemicals such as methanol and ammonia. Principally, syngas can be synthesized from any carbon containing sources such as liquid hydrocarbons, natural gas, coal, municipal solid wastes and biomass. Present day technology development on syngas production aims to supply clean fuels, to increase energy efficiency, and to eliminate the emissions related problems. Syngas is classified depending on gas composition as shown in Table 1 [1]. Synthetic oil and oil derivative compounds are produced depending on energy content of produced syngas.

Synthetic fuel technologies started with the patent taken by Friedrich Bergius in 1913 [2]. First fuel production began after 1919 by direct conversion of coal. Thereafter, indirect coal gasification process as shown in Figure 1 was developed by Franz Fischer and Hans Tropsch in 1923 [3]. Germany's kerosene and gasoline demand was supplied mainly by these two processes during World War II. Technology matured during the war period. After the war, the technology was transferred to USA. First commercial synthetic fuel production plant was operated up to the first oil crisis in 1955. Then, cost competitiveness between coal and oil has become main factor that determines the attention in synthetic fuel production technologies up to now.

Table 1: Classification of syngas in terms of energy content [1]

	Low-Btu Gas	Medium-Btu Gas	High-Btu Gas
Composition	CO, H ₂ and gases whose heating values are less than 300Btu/scf	CO, H ₂ , less in amount CH ₄ and CO ₂ , and gases whose heating values are between 300 and 700Btu/scf	SNG, CH ₄ (95%), and gases whose heating values are greater than 300Btu/scf
Oxidizing agent	Air	Pure Oxygen	No agent. Result of methanation reaction

1.1. Coal Gasification Technology

Coal gasification is the process where coal is reacted with an oxidizing medium to produce valuable products such as syngas and methane. Operating conditions such as oxidizing medium, temperature and pressure depends on quality feedstock in terms of chemical composition, moisture content, volatile matter and fixed carbon amounts. Each factor has an importance for final product composition. For example, depending on the product composition, oxidizing agent can be selected as CO_2 for high CO rich product or as H_2O for a H_2 rich product. Air or pure O_2 can also be used for production of low-Btu and medium-Btu gases respectively as shown in Table 1. Thermodynamic equilibrium analysis shows the restriction of maximum operational temperature depending on desired products. Methane rich product streams are favored at low temperatures and high pressures whereas syngas formation needs low pressures and high temperatures as shown in Figure 2.

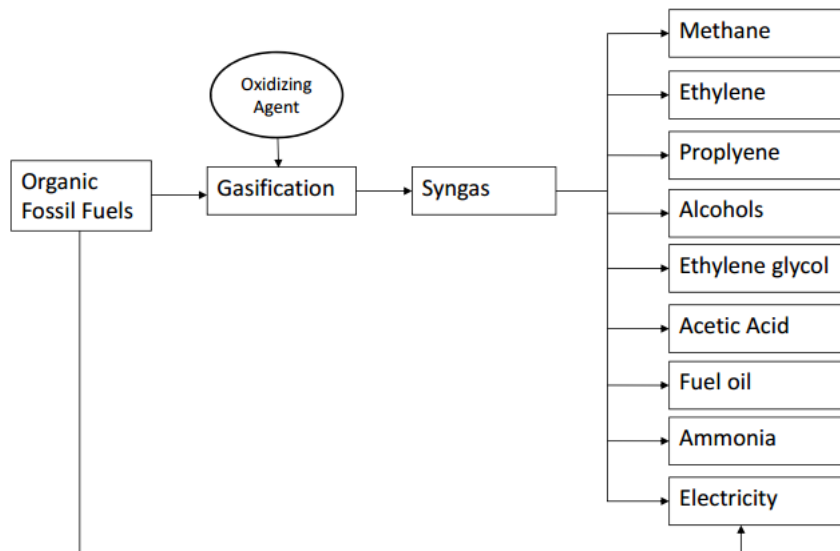


Figure 1: Syngas production via fossil fuel gasification processes [1]

Coal passes three stages during gasification. At low temperatures ($<120^\circ\text{C}$), water content of coal is eliminated. Then, volatile matter is released. Volatile matter output changes from light to heavy hydrocarbons depending on the temperature. As the temperature increases, depolymerization reactions towards metastable intermediates occur. Then, tars, oils and gases such as methane and carbon monoxide form as a result of cracking of these metastable intermediates. Coal is converted to char which has high porosity and surface area at the end of pyrolysis. The final step in gasification is the reaction of char with an oxidizing agent.

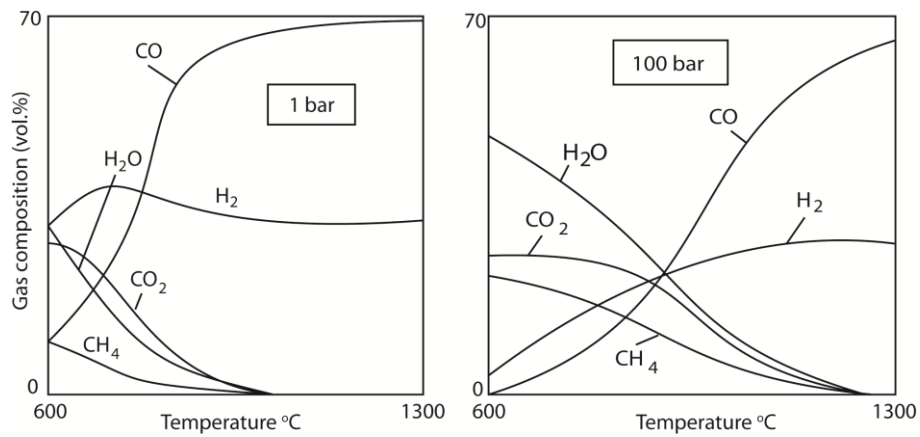


Figure 2: Equilibrium compositions at different temperatures and pressures [1]

Gasification can be broadly classified into four types; steam gasification, CO_2 gasification, hydrogasification and partial oxidation gasification. Steam gasification occurs by the reaction of steam with carbon to produce carbon monoxide and hydrogen mainly. The reaction needs high energy and excess amount of steam. CO_2 gasification processes are generally preferred for high CO content product streams. Coal is hydrogenated to produce methane during hydrogasification. The reaction is exothermic and favored at low temperatures. Nevertheless, high reaction rates are achieved at high temperatures and high pressures. Partial oxidation gasification is generally used for controlling oxygen concentration during reactions since excess oxygen can initiate unwanted combustion reactions.

Four matured gasification reactors are generally used in industry such as fixed bed (Figure 3), fluidized bed, (Figure 4), entrained bed (Figure 5) and molten-metal-bath (Figure 6). Expected temperature dependent motions of coal and gas in the reactors were also stated in Figure 3 to Figure 6. Their comparison was done and shown in Table 2.

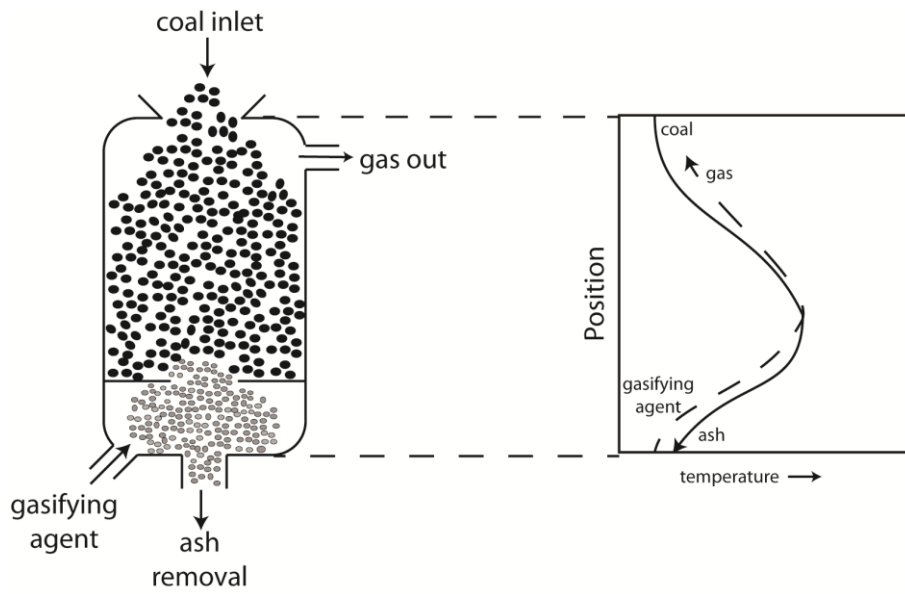


Figure 3: Fixed bed coal gasification processes operating principles [1]

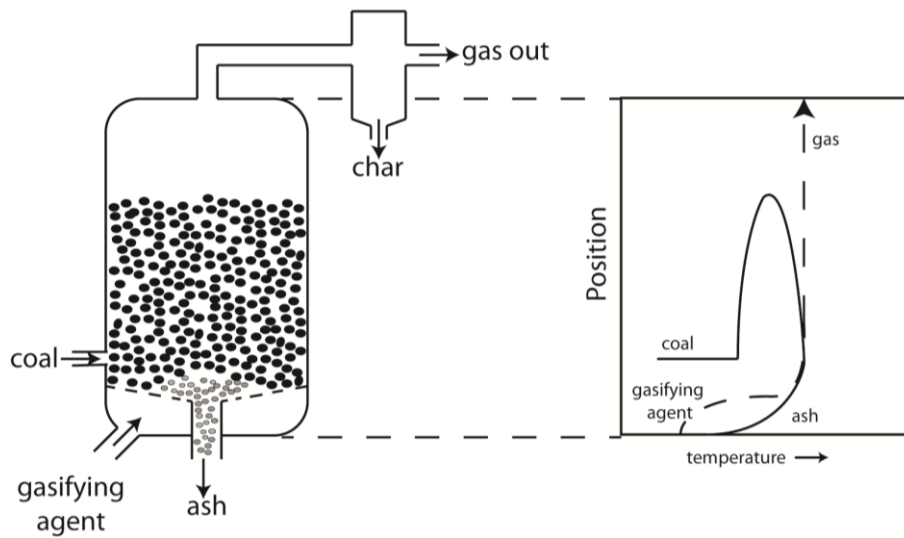


Figure 4: Fluidized bed coal gasification processes operating principles [1]

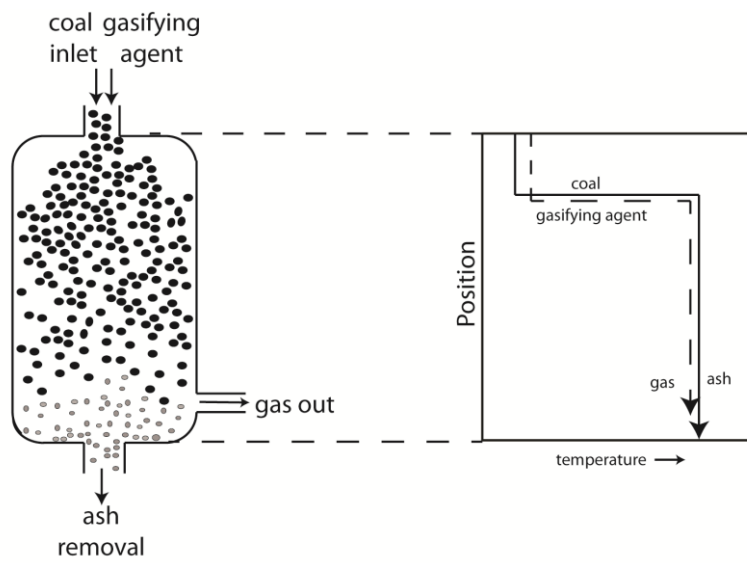


Figure 5: Entrained bed coal gasification processes operating principles [1]

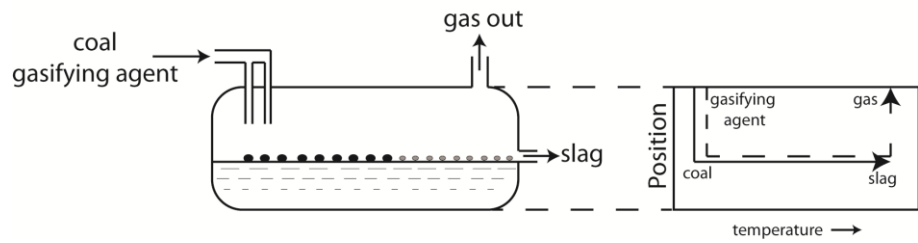


Figure 6: Molten-metal-bath coal gasification processes operating principles [1]

Table 2: Comparison of coal gasification technologies [1]

	Fixed Bed	Fluidized Bed	Entrained Bed	Molten-Metal Bath
Coal Motion	Slow	Fluid like	Very Fast	Immediately absorbed and decomposed by molten bath
Ash Removal	Dry ash or slag	Dry ash (continuously due to sintering)	Slag	Slag
Residence Time	Seconds for gases, minutes or hours for coal	Long	Short	Short
Specific Properties	Due to temperature gradient between bottom and top level of the reactor, coal exhibits drying, degassing, gasification and combustion periods respectively.	<ul style="list-style-type: none"> • Solid and gas particles interact with each other homogeneously. • Generally pulverized coal is used 	<ul style="list-style-type: none"> • Small coal particles are used • Gas and coal mixes before reactor • Due to short residence time, high carbon conversions and high temperatures are desired • Recycle stream is used 	<ul style="list-style-type: none"> • For high carbon loadings, molten bath absorbs excess carbon so it limits unreacted carbon • For high oxidizing agent loading, dissolved carbon or bath material reacts with oxidizing agent. • Molten bath absorbs sulfur and some trace elements and removes from the system in the form of slag.
Restrictions	Appropriate for no caking or limited caking coals	Problematic with caking coals	None	None
Processes	<ol style="list-style-type: none"> 1. Lurgi 2. B.G. Slagging Lurgi 3. Wellman-Galusha 	<ol style="list-style-type: none"> 1. Two-stage F.B. U-Gas 2. U-Gas 3. Hy-Gas 	<ol style="list-style-type: none"> 1. Koppers-Totzek 2. Texaco 3. Babcock&Wilcox 	<ol style="list-style-type: none"> 1. Molten Iron Bath 2. Kellogg 3. ATGAS

1.2. Chemical Looping Systems

Chemical looping processes on fossil fuel conversion and CO₂/H₂O reduction have been known over 100 years. Nevertheless, no commercial plant is in operation yet. Large scale demonstration units as shown in Table 3 are still operated to solve technical and operational difficulties.

Table 3: Current large scale demonstration plants

Organization	Process	Capacity
HUNOSA, Spain [4]	CaO-CaCO ₃ looping	2 MW _{th}
Technical University of Darmstadt, Germany [4]	Limestone based CO ₂ absorption	1 MW _{th}
Industrial Technology Research Institute, Taiwan [4]	CO ₂ capturing by Ohio State CCR	2 MW _{th}
Technical University of Darmstadt, Germany [4]	Emission free coal combustion	1 MW _{th}
Alstom, U.S. [4]	CaO-CaSO ₄ looping	3 MW _{th}
Ohio State University, U.S. [4]	Syngas production via FeO-Fe ₃ O ₄	250 kW _{th}
Chalmers University of Technology, Sweden [5]	Chemical looping combustion	10 kW _{th}

The theory behind chemical looping is based on carrying an agent between reaction environment and regeneration zone. Its ultimate goal is to increase system efficiency by decreasing heat and mass transfer related energy losses. This technology is emerging as an alternative to oxy-fuel combustion where pure oxygen is used in combustion. In this process, higher temperatures are achieved. Product gas contains CO₂ at high levels. Thus, no additional separation units are required for sequestration. It is also known that oxy-fuel combustion offers high overall efficiency mainly by increasing flame temperatures, decreasing mass and volume of flue gas. Nevertheless, the feasibility of the overall process depends strongly on the oxygen enrichment facilities those of which require high capital investments.

Chemical looping systems offer same combustion methodology by using metal oxides as oxygen carriers. Therefore, high pressure oxygen distillation facilities could be replaced by metal oxidation processes. Oxygen needed for combustion processes was supplied by metal oxides as shown in Figures 7 and 8. Nevertheless, suitable chemical looping material selection is important since its oxidation and its reduction/decomposition should be easy at system operational conditions.

Most widely used chemical looping systems are developed in the combustion and CO₂ sequestration areas. Their operational principle is shown as Figure 8. In addition to these processes, MeO/MeSO₄ looping system is used for SO_x emission reduction which has similar operational diagram as stated in Figure 8(b).

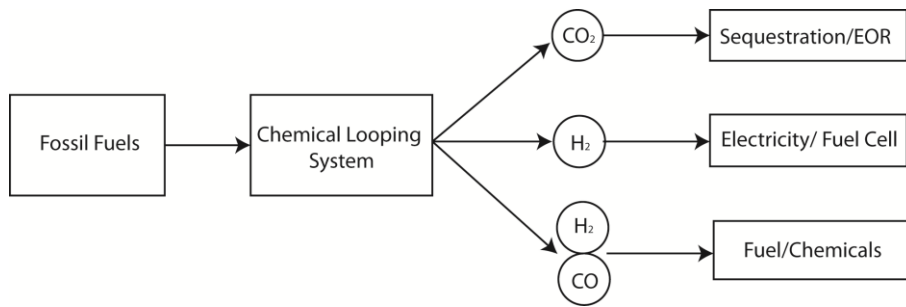


Figure 7: Chemical looping systems from raw materials to end products [4]

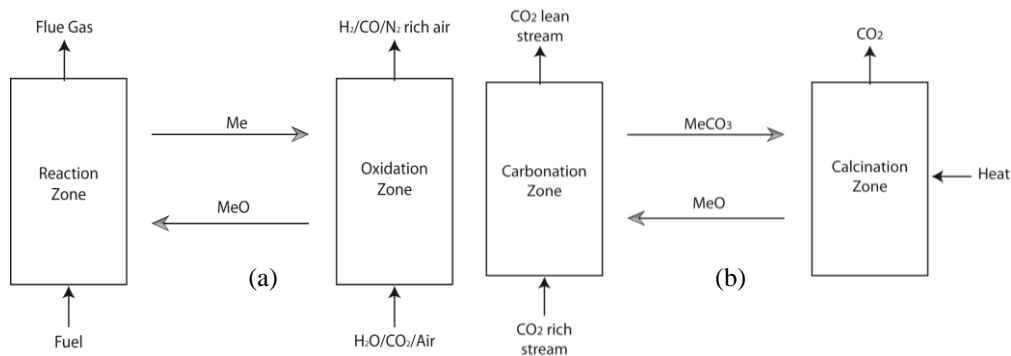


Figure 8: Chemical looping systems; (a) Oxygen Carrier, (b) CO₂ Carrier

1.3. Objectives

Uner et al. [6] demonstrated that reducible metal oxides such as cobalt and lead oxides can be used for diesel soot oxidation using the lattice oxygen. The potential for these oxides as chemical looping materials for coal oxidation was investigated by Gibbs free energy minimization methods and experimental verification of the thermodynamic predictions.

CHAPTER 2

LITERATURE SURVEY

2.1. Gasification

Carbonaceous materials originated from organic or fossil sources can be converted to high valuable products via gasification processes. Desired product composition is achieved by selecting appropriate gasifying agent with optimum operational conditions. For instance, oxygen reacts with carbon immediately in reaction environment. Therefore, oxygen concentration in reactant gas crucial for desired product yield since rate of reaction of formed CO₂ with carbon is very low [7].

Reaction enthalpies and Gibbs free energies of main gasification reactions are shown in Table 4. Product (CO, CO₂, H₂, H₂O, CH₄, etc.) of this main reactions are strongly depended on the type of coal, oxidizing medium, and thermodynamics of the system.

Table 4: Main gasification reactions

Reactions	$\Delta H_{1000^{\circ}C}^{\circ}$ * (kJ/mole)	$\Delta G_{1000^{\circ}C}^{\circ}$ * (kJ/mole)	Reaction Temperatures.
$C + H_2O \rightarrow CO + H_2$	135.7	-46.7	High
$C + CO_2 \rightarrow 2CO$	167.7	-52.3	High
$C + 2H_2 \rightarrow CH_4$	-90.3	48.9	High/Moderate
$C + O_2 \rightarrow CO_2$	-395.2	-396.1	High
$C + 0.5O_2 \rightarrow CO$	-113.7	-224.2	High
$CO + H_2O \rightarrow CO_2 + H_2$	-32.2	-5.6	High/Moderate
$CO + 3H_2 \rightarrow CH_4 + H_2O$	-225.8	95.6	Moderate/Low

* 1000°C is selected as a representative temperature for gasifying environment.

Coal contains several organic and inorganic molecules. Some of these structures such as sulfur seem undesirable for downstream processes due to poisoning effect to some valuable catalysts. Therefore, operating companies generally pretreat coal before gasification. Nevertheless, the general consequence of pretreatment becomes a decrease in kinetics no matter what a catalyst used after demineralization process [8, 9]. Therefore, promoter effect of elements (Fe, Ca, Si, Al, K, S, Na) existed in the ash were studied.

Gasification rates strongly depend on the surface structure of carbonaceous material. McKee [10] found that gasification rates increase with an increase in charring temperature up to a point. Therefore, choosing right charring temperatures for each coal type is important.

2.2. Mechanism

The kinetics relevant to coal gasification is heavily affected by the mass and heat transfer limitations. Transport of reactant gases through grains and removal of product gases from grains occur at the same time. This sequence can be visualized as in Figure 9. Firstly, oxidizing agent is transported through boundary layer, followed by pore diffusion. Thereafter, reaction is occurred and products are followed reverse pattern.

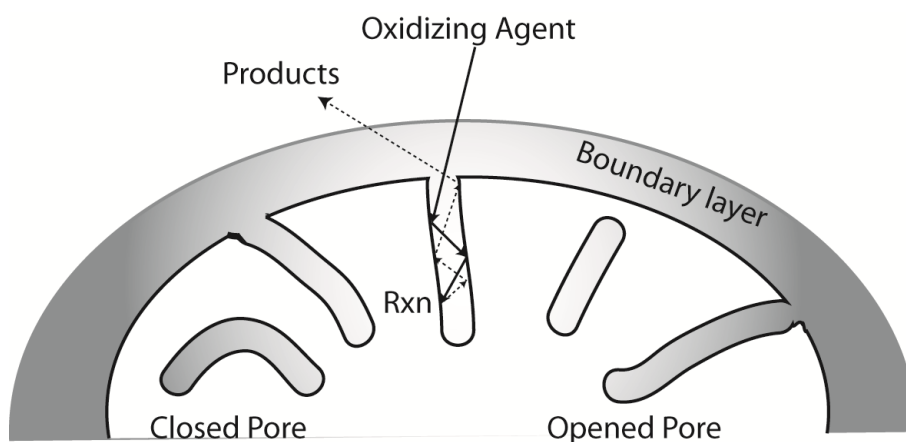
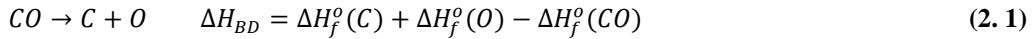


Figure 9: Mass transport mechanism expected during coal gasification

2.3. Bond Dissociation Energies

The energy required to break a bond with another atom is defined as bond dissociation energy; ΔH_{BD} . Amount of this energy mainly predicts the strongest bond which can limit reaction. Therefore, careful calculation of these bond energies is important. As an example, required energy for bond cleavage for carbon monoxide can be calculated by heat of formation of consisting atoms as in equation 2.1.



Energy requirement for breaking certain bonds is shown in Table 5. Level of this energy requirement determines the important bond which restricts reaction kinetics. For a typical coal gasification process, breaking C-C bond needs highest energy whereas C-H bond needs less. Most catalysts used in refineries are designed for attacking C-H bond in cracking units

2.4. Sulfur Effect on Reactivity

High sulfur containing fossil fuels such as coal, petroleum coke, and asphaltite are less preferable since significant portion of capital investment was done to carbon-source-pretreatment and flue-gas-separation facilities. Companies generally solve sulfur problem by using pretreatment facilities due to high energy needed for H-S and CO-S bond cleavages (Table 5). Sulfur content in the fossil fuels is generally due to organic sulfur, inorganic sulfides, and inorganic sulfates depending on geological history. Therefore, these facilities decrease inorganic sulfur content by demineralization despite conversion loss [12]. It is found that decrease in pyrite amount is the main contributor of this conversion loss [13]. In addition, it was also found that not elemental sulfur [14] or elemental iron has any significant effect. Nevertheless, increase in reactivity is only possible when two elements come together. Known activity for pyrite is explained by H_2S formation from reduction reaction to pyrrhotites (2.2) which forms and increases active metal vacancies [15, 16, 17].



Maximum conversion is achieved in a critical range ($S/Fe \leq 1$) when partial pressure of H_2S should be enough to balance formed and vanished vacancies [18]. Therefore, H_2S can dissociates at these vacancies which hydrogen can be transferred to organic compounds [19] for breaking strong bonds, removing nitrogen content and forming catalytically active minerals [20].

Table 5: Bond dissociation energies of certain molecules at 298K [11]

Bond	Reaction	ΔH_{BD}° (kJ/mole)
<i>C - C</i>	$C_2 \rightarrow C + C$	607 ± 21
	$CH_2CO \rightarrow CH_2 + CO$	342.7
	$CH_3CO \rightarrow CH_3 + CO$	46 ± 4
<i>C - H</i>	$CH \rightarrow C + H$	339 ± 2.1
	$CH_2 \rightarrow CH + H$	421.7
	$CH_3 \rightarrow CH_2 + H$	473 ± 4
	$CH_4 \rightarrow CH_3 + H$	429.9 ± 8.4
	$HCO \rightarrow CO + H$	124.7
	$H_2CO \rightarrow HCO + H$	318
<i>C - O</i>	$CO \rightarrow C + O$	1076.5 ± 0.4
	$CO_2 \rightarrow CO + O$	532.2 ± 0.4
	$CH_3OH \rightarrow CH_3 + OH$	377 ± 13
	$HCOOH \rightarrow CHO + OH$	402 ± 13
	$CH_3COOH \rightarrow CH_3CO + OH$	452 ± 21
<i>C - S</i>	$CS \rightarrow C + S$	761 ± 21
	$OCS \rightarrow CO + S$	310.5
	$CS_2 \rightarrow CS + S$	397
	$CH_3S \rightarrow CH_3 + S$	289
<i>S - H</i>	$HS \rightarrow H + S$	353.1 ± 6.3
	$H_2S \rightarrow HS + H$	381 ± 4
<i>S - O</i>	$SO \rightarrow S + O$	521.7
<i>S - S</i>	$S_2 \rightarrow 2S$	428.9 ± 6.3

2.5. Catalyst Research

2.5.1. Conventional Processes

Juntgen [21] and Nishiyama [22] studied the catalytic activity of alkali and alkaline earth metals. They observed that alkali and alkaline earth metals increases rate of gasification depending on gasifying agent and gasification conditions. Douchanov and Angelova [9] showed that K_2CO_3 , Na_2CO_3 and NaF increases gasification rate during steam gasification of char. McKee and Chatterji [23] investigated the effect of Li_2CO_3 and observed that catalytic activity increases considerably when compared with K_2CO_3 , Na_2CO_3 .

Exxon's studies [24] generally focused on the effect of alkali metals (Li, Na, K) during gasification conditions. It was shown from printed reports that when these metals were used with certain proportions, steam gasification rates increased with no coal caking. In addition, these catalysts promoted the product gas stream to have a composition close to methanation equilibrium.

Hahn and Huttinger [25] showed that reactivity of coke with steam is increased and required activation energy is decreased with an increase in iron concentration. A similar study was carried out by Otto et al [8] and they showed that nickel addition into pure carbon increases significantly reaction kinetics.

Uner et al. [6] studied on performance of lead and cobalt mixed oxides during soot oxidation. They demonstrated that Diesel soot was oxidized using the lattice oxygen in lead oxide, cobalt oxide, and mixed PbOx-CoOx catalysts at low temperatures ($<470^\circ C$). This conclusion leads to an idea about these metal oxides can also be used as oxidation agents. Therefore, this study is taken as a starting point of this thesis.

2.5.2. Chemical Looping Processes

Research on suitable chemical looping agent goes as far back as 100 years. The first patent was taken by Messerschmitt in 1910 [26]. Thereafter, technology based on Fe/FeO/Fe₃O₄ looping agent was developed by Lane [27]. Lewis and Gilliland were designed fluidized bed reactor used Cu₂O/CuO [28].

Biljetina and Tarman designed a new iron-steam process for H₂ production in 1970s [29]. Dobbyn et al. studied performances of several materials during CO₂ absorption at coal gasification pilot plants. Their report pointed out CaO/CaCO₃ material as the most suitable chemical looping agent [30]. Miyamoto *et al.* showed that germanium oxide dispersed on alumina has a significant effect on hydrogen yield during water splitting reactions [31]. Kodama *et al.* studied the reactivity of tungsten oxide during a chemical cycle; reduction by CH₄ and oxidation by water. They stated that reactivity of reduction and oxidation steps increases significantly when syngas production from methane is catalyzed by zirconia supported tungsten oxide [32]. Ryden and Lyngfelt studied the catalysts for chemical looping combustion for better heat transfer during steam methane reforming process [33].

2.6. Phase Diagrams

CoOx and PbOx behaviors depending on oxygen concentration and temperature were analyzed by the help of phase diagrams. Phase transformations of these metal oxides were shown in Figures 10 and 11 as a function of temperature and concentration.

At low temperatures, lead-oxide system has various compounds such as Pb, PbO, Pb₂O₃, Pb₃O₄, Pb₁₂O₁₇, Pb₁₂O₁₉, and PbO₂. Especially when O/Me molar ratio is in the range of 55% and 67%, lead can store more oxygen by changing its crystal structure. In addition, it was also seen that lead has low melting point around 327°C while it's most stable oxide, PbO, has 872°C.

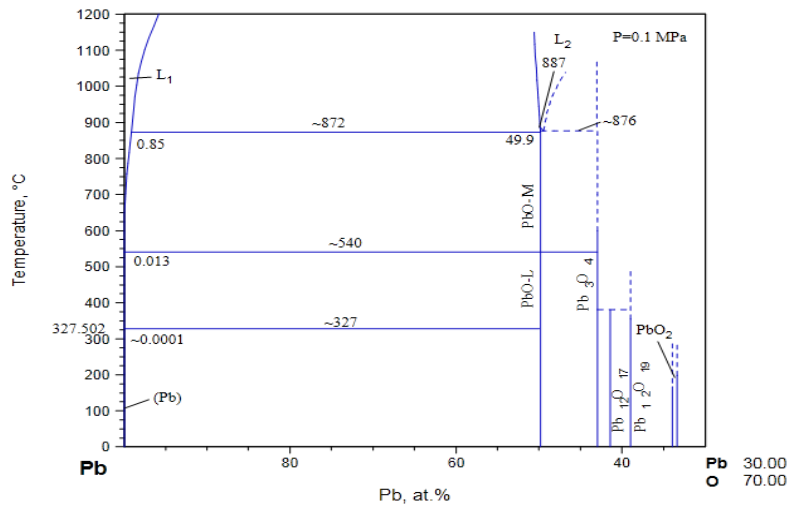


Figure 10: Pb-O phase diagram [34]

Cobalt has two most common oxide forms as CoO and Co₃O₄. Transformation between CoO and Co₃O₄ occurs when atomic oxygen concentration is around 50% as shown in Figure 11. Melting temperature of CoO is pretty high, around 1500°C.

Synergetic effect due to alloying sometimes offers an increase in catalytic activity. Therefore, eutectic point of these two metals was firstly examined by searching a phase diagram for Co-Pb-O system. Nevertheless, no eutectic point was found in the literature.

During the phase diagram examination, sulfur capture ability was also considered since sulfur has a significant effect on combustion and gasification. Therefore, sulfur involving phase diagrams of studied metals were also inspected. Fe/S based compounds are widely founded in nature. Iron has a high capability to absorb sulfur as shown Figure 12. Even in the high S concentrations such as between 48% and 68%, many forms of pyrite and pyrrhotites can be formed. Same is true for both cobalt-sulfur (Figure 13) and lead-sulfur (Figure 14) systems. Especially lead-sulfur system has similar capacity with iron-sulfur system in terms of sulfur capturing.

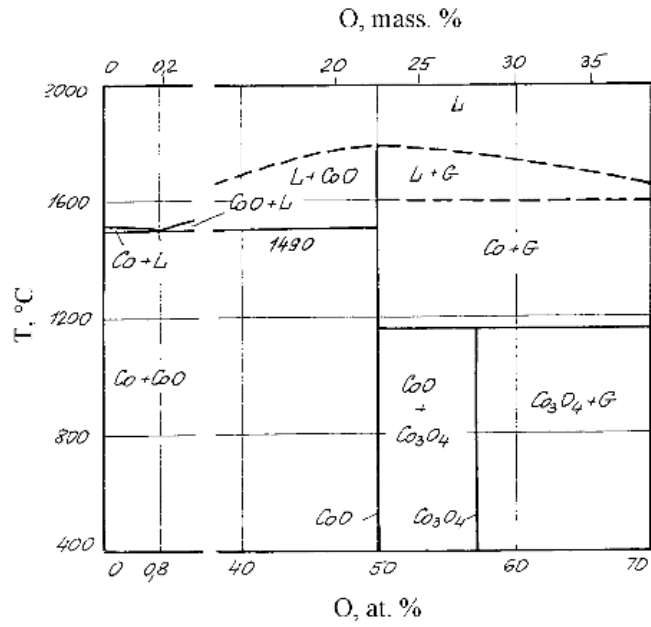


Figure 11: Co-O phase diagram [35]

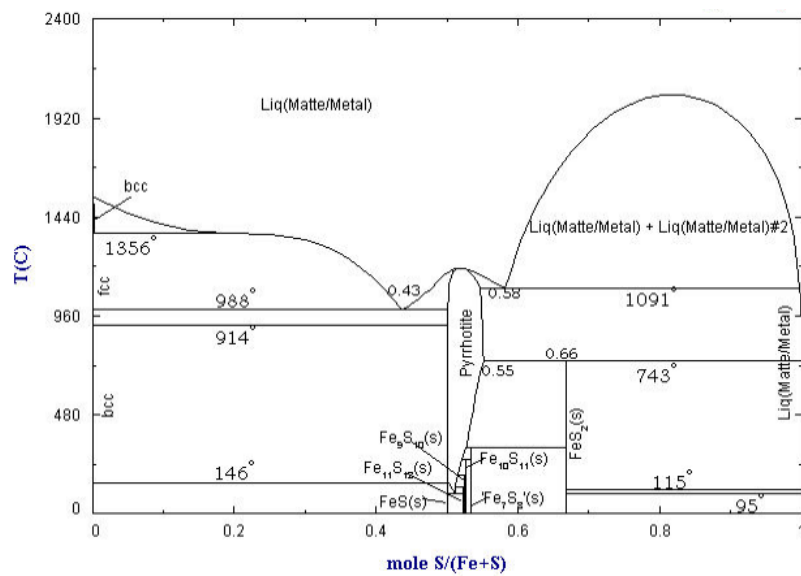


Figure 12: Fe/S phase diagram. [36]

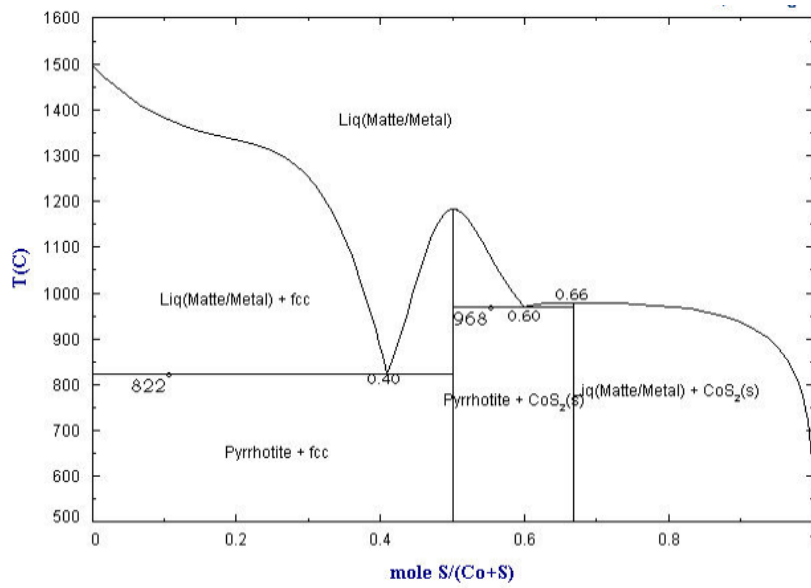


Figure 13: Co/S phase diagram [36]

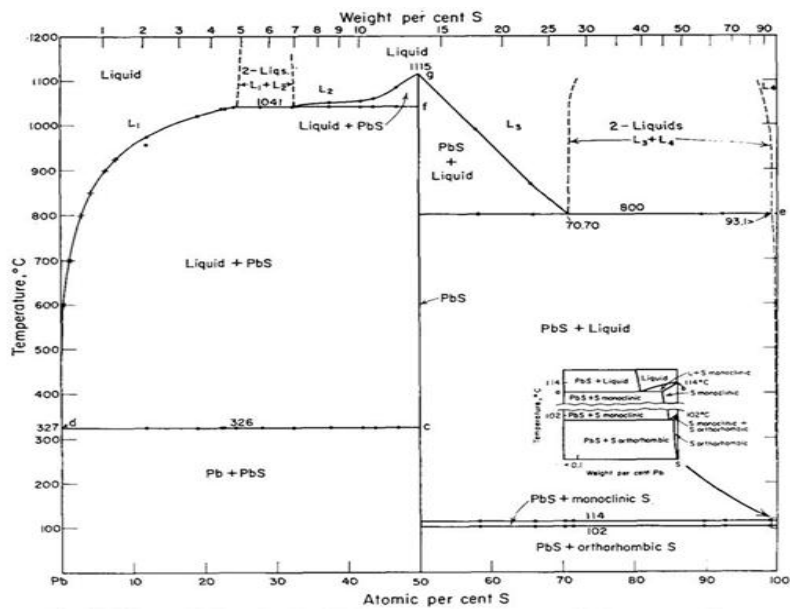


Figure 14: Pb/S phase diagram [37]

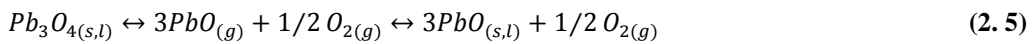
2.7. Thermal Decomposition

Self-decomposition ability at low temperatures for Co-Ox and Pb-Ox pairs is important for atomic or molecular oxygen transfer to the carbon source for gasification. Basic principle of thermal decomposition is based upon the fact that energy absorbed at the bonds becomes instable as temperature increases. Magnitude of this instability depends on both substance and system energy level. High magnitudes results with a self-decomposition reactions which stabilizes the substance by splitting into two or more compounds which means substance stabilizes itself by reducing its Gibbs free energy.

There are two well accepted reaction types when describing thermal decomposition reactions [38, 39]: congruent dissociative vaporization (CDV) and incongruent dissociative vaporization (iCDV). During the CDV, reactant decomposes into gaseous products (2.3) while in iCDV, reaction has at least one solid or liquid product (2.4).



L'vov and Ugolkov [40] show that lead tetroxide decomposes to lead monoxide around 784K. Since it follows the iCDV (2.3), this decomposition seems to be completed in a single step. However, they observed that during decomposition, crystal structure has also changed from tetragonal to orthorhombic which cannot be explained in a single step. L'vov explains this situation as such a transformation of a solid reactant into solid product is impossible without any intermediate stage related to a change of its aggregate state. [41] Therefore, according to L'vov and Ugolkov [40] all phenomena can be explained by an addition of an intermediate step where the collision of low-volatile atoms and molecules results with a condensation. (2.5, 2.6)



CHAPTER 3

MATERIALS AND METHODS

3.1. Thermodynamic Analysis

In the thermodynamic analysis part, an equilibrium analysis was conducted. For this purpose, Ellingham and predominance diagrams were constructed. Then, Gibbs free energy minimization method was applied for equilibrium compositions between oxygen, metal, metal oxide, carbon, carbon monoxide and carbon dioxide. Sulfur and sulfur dioxide were also considered in some calculations. All calculations were performed by using thermochemical data obtained from Barin [42]. Only one data source was used to maintain consistency.

3.1.1. Ellingham Diagrams

Ellingham diagrams give a comparative idea about the relative reactive strengths of certain compounds. These diagrams were constructed by firstly writing desired reactions such as $C + O_2 \leftrightarrow CO_2$ and $Pb + 1/2O_2 \leftrightarrow PbO$. Then, reaction Gibbs free energies were calculated. These calculated data were based on per mole O_2 since it exists in all reaction systems. For instance, Gibbs energy of $Pb + 1/2O_2 \leftrightarrow PbO$ at 400K is -178.7kJ. This value was divided by $1/2$, the stoichiometric coefficient of oxygen molecule, to bring the Gibbs energy for this reaction to -357.4kJ/mole O_2 reacted. The, Gibbs energy at other temperatures were also calculated and plotted for all reactions. Then, Ellingham diagram is obtained.

3.1.2. Predominance Diagrams

Predominance diagrams are used to find stable compounds in a multicomponent reactive system at equilibrium. They are actually a simple type of phase diagrams and their constructions are based on the Gibbs free energy calculations with the assumption of no mutual solubility between solid and liquid phases. In other words, all compounds in condensed phases are immiscible with each other. Detailed explanation of followed procedure during constructions is explained in Appendix A.

3.1.3. Gibbs Free Energy Minimization Analysis

Thermodynamics equilibrium condition, $dG_{T,P} \leq 0$ is taken as a starting point. The equilibrium composition can be predicted by calculating the composition that minimizes the total Gibbs free energy. Among the methods available in the literature, Gibbs free energy minimization method was selected since it does not need any reaction mechanism postulation. Therefore, it seems best by far for compounds that consist of many inorganic and organic structures. Basically, user defines the elements and molecules predicted to be in equilibrium. Then, using this method free energy combinations of the compounds are calculated to find the minimum value of system Gibbs free energy by Langrange multipliers method.

Lagrange multipliers approach is a mathematical technique for finding the minimum value of a function which consists of n variables [43].

$$\Gamma(x_1, x_2, \dots, x_n) \rightarrow \min \quad (3.1)$$

Let us define constraints as m new relation ($m < n$).

$$\phi_k(x_1, x_2, \dots, x_n) = 0 \quad k = 1, 2, \dots, m \quad (3.2)$$

Then, the minimized function is formed by integration of Langrange multipliers λ_k . The final form becomes as equation 3.3.

$$\varphi = \Gamma + \sum \lambda_k \phi_k \quad (3.3)$$

Minimum value of equation 3.3 is found by taking the derivative of φ with respect to a variable as x_i as equation 3.4. After arranging equation 3.2 and 3.4, solution of variables that minimizes equation 3.3 should be solved.

$$\left(\frac{\delta \varphi}{\delta x_i}\right) = 0 \quad i = 1, 2, \dots, n \quad (3.4)$$

For chemical processes, equations 3.1 to 3.4 have to be modified by inserting appropriate equations instead of the functions φ , Γ , ϕ . Minimized function is defined as the system Gibbs free energy at a certain temperature and pressure. Therefore, total free energy of the system is calculated by summing partial free energies all species in each phase. Since partial Gibbs free energies can be expanded as equation 3.6, system Gibbs free energy can be rewritten in the form of equation 3.7.

$$G = \sum_{j=1}^{\#P} \sum_{i=1}^{\#C} n_i^j \mu_i^j \quad (3.5)$$

$$\mu_i^j = \mu_i^o + RT \ln a_i^j \text{ where } \begin{cases} a_i^s = \gamma_i^s \cdot x_i^s \\ a_i^l = \gamma_i^l \cdot x_i^l \\ a_i^g = P \cdot y_i \end{cases} \quad (3.6)$$

$$G = \sum_{j=1}^{\#P} \sum_{i=1}^{\#C} n_i^j (\mu_i^o + RT \ln a_i^j) \quad (3.7)$$

Let function Γ in equation 3.1 be $\Gamma = G/RT$ by assuming γ_i^s, γ_i^l are equal to unity for ideal systems,

$$\Gamma = \left(\sum_{i=1}^{\#C} n_i^s \left(\frac{\mu_i^o}{RT} + \ln x_i^s \right) \right)^s + \left(\sum_{i=1}^{\#C} n_i^l \left(\frac{\mu_i^o}{RT} + \ln x_i^l \right) \right)^l + \left(\sum_{i=1}^{\#C} n_i^g \left(\frac{\mu_i^o}{RT} + \ln P + \ln y_i \right) \right)^g \quad (3.8)$$

Then, next step is to define stoichiometric constraints.

$$\emptyset_k = \beta_k - \sum_{j=1}^{\#P} \sum_{i=1}^{\#C} \alpha_{ik} n_i^j = 0 \quad k = 1, 2 \dots m \quad (3.9)$$

Then, rearrangement of equation 3.3 gives:

$$\varphi = \left(\sum_{i=1}^{\#C} n_i^s \left(\frac{\mu_i^o}{RT} + \ln x_i^s \right) \right)^s + \left(\sum_{i=1}^{\#C} n_i^l \left(\frac{\mu_i^o}{RT} + \ln x_i^l \right) \right)^l + \left(\sum_{i=1}^{\#C} n_i^g \left(\frac{\mu_i^o}{RT} + \ln P + \ln y_i \right) \right)^g + \sum_{k=1}^m \lambda_j \left(\sum_{j=1}^{\#P} \sum_{i=1}^{\#C} \alpha_{ik} n_i^j - \beta_k \right) \quad (3.10)$$

For determination the composition that minimizes φ , derivative of equation 3.10 with respect to n_i^s, n_i^l, n_i^g is taken. (Equation 3.11-3.13)

$$\left(\frac{\delta \varphi}{\delta n_i^s} \right) = 0 = \left(\frac{\mu_i^o}{RT} + \ln x_i^s \right) + \sum_{k=1}^m \alpha_{ik} \lambda_k \quad (3.11)$$

$$\left(\frac{\delta \varphi}{\delta n_i^l} \right) = 0 = \left(\frac{\mu_i^o}{RT} + \ln x_i^l \right) + \sum_{k=1}^m \alpha_{ik} \lambda_k \quad (3.12)$$

$$\left(\frac{\delta \varphi}{\delta n_i^g} \right) = 0 = \left(\frac{\mu_i^o}{RT} + \ln P + \ln y_i \right) + \sum_{k=1}^m \alpha_{ik} \lambda_k \quad (3.13)$$

In addition to these equations, elemental mole balance and solid, liquid and gas molar ratios are specified to system of equations as equations 3.14 to 17.

$$\sum_{j=1}^{\#P} \frac{\beta_k}{n_{tot}^j} - \sum_{j=1}^{\#P} \sum_{i=1}^{\#C} \alpha_{ik} \frac{n_i^j}{n_{tot}^j} = 0 \quad k = 1, 2 \dots m \quad (3.14)$$

$$\sum_{i=1}^{\#P} x_i^s = 1 \quad (3.15)$$

$$\sum_{i=1}^{\#P} x_i^l = 1 \quad (3.16)$$

$$\sum_{i=1}^{\#P} y_i = 1 \quad (3.17)$$

The procedure used for solution of equations 3.11 to 3.17 is given below:

1. Components expected in equilibrium are listed.
2. Partial Gibbs free energies are found from literature or calculated at system pressure and temperature.
3. Initial moles for components are determined.
4. Since solution is found by an iterative method, initial guesses for each expected components are introduced. These guesses are important for convergence. Therefore, they should be determined carefully.
5. Finally, equations are solved using a Matlab® code (Appendix B).

The Matlab® code was written for finding the composition that minimizes the Gibbs free energy of a specified system. Since coal oxidation process was the focus, coal was selected as carbon source. It was assumed that volatile matter and moisture was removed from the system. Therefore, only fixed carbon and sulfur components (existence ratio is 1mol C/0.05 mol S from stated data in Tables 13 and 14), were taken into consideration during calculations. Then, performance of the selected materials; lead oxide, cobalt oxide and iron oxide, were examined with respect to temperature and pressure.

3.2. Experimental Methods

3.2.1. Synthesis Methodology

Bulk lead oxide, bulk cobalt oxide, bulk mixed oxide of cobalt and lead, Pt-doped cobalt oxide; γ -Al₂O₃ supported cobalt oxide and Pt-doped γ -Al₂O₃ supported cobalt oxide were synthesized. In addition, technical grade cobalt oxide supplied from Ege-Ferro and technical grade lead rods were also used during experiments.

3.2.1.1. Bulk Lead Oxide Synthesis

Lead acetate salt was dissolved in deionized water. Solution was evaporated for excess water removal. Then, it was dried overnight at 120°C and calcined in static air at 500°C for 3h.

3.2.1.2. Bulk Cobalt Oxide Synthesis

Cobalt (II) nitrate salt was dissolved in deionized water. Solution was evaporated for excess water removal. Then, it was dried overnight at 120°C and calcined in static air at 500°C for 3h.

3.2.1.3. Bulk Cobalt Oxide and Lead Oxide Synthesis

Lead acetate salt was dissolved in deionized water. Predetermined amount of cobalt (II) nitrate salt was slowly added with constant stirring. Stirred solution was evaporated for excess water removal. Then, it was dried overnight at 120°C and calcined in static air at 500°C for 3h.

3.2.1.4. Pt doped Cobalt Oxide Synthesis

Appropriate amount of $Pt(NH_3)_4Cl_2 \cdot 2H_2O$ salt was dissolved in deionized water. Then, previously synthesized cobalt oxide was added to this solution. Slurry was mixed and stirred at 80°C until a paste was formed. Paste was dried overnight at 120°C and calcined in static air at 500°C for 3h.

3.2.1.5. γ -Al₂O₃ supported Cobalt Oxide Synthesis

Appropriate amount of cobalt (II) nitrate salt was dissolved in deionized water. γ -Al₂O₃ was slowly added to this solution with constant stirring. Slurry was mixed at 80°C until a paste was formed. Paste was dried overnight at 120°C and calcined in static air at 500°C for 3h.

3.2.1.6. Pt doped γ -Al₂O₃ supported Cobalt Oxide Synthesis

Appropriate amount of $Pt(NH_3)_4Cl_2 \cdot 2H_2O$ salt was dissolved in deionized water. Then, synthesized alumina supported cobalt oxide was added to this solution. Slurry was mixed at 80°C until a paste was formed. Paste was dried overnight at 120°C and calcined in static air at 500°C for 3h.

3.2.2. Synthesized Material Characterization

Rigaku X-ray diffractometer (30kV, 15mA) were used with Cu K α radiation ($\lambda=1.54\text{\AA}$). Spectra were taken in $5^{\circ}\leq 2\theta\leq 80^{\circ}$. Peaks in spectra were characterized by comparing with data cards [44].

3.2.3. Visual Observation Experiments

Predicting reacting environment is important for understanding reaction mechanism and situations faced by looping material. Thus, a simple oxidation and reduction experiment was prepared by using a quartz glassware, an aquarium type air pump and a high temperature oven as shown in Figure 15. 200mg lead rods were put into glassware. Air pump was started at maximum rate. Then, oven was heated at a rate of $10^{\circ}\text{C}/\text{min}$.

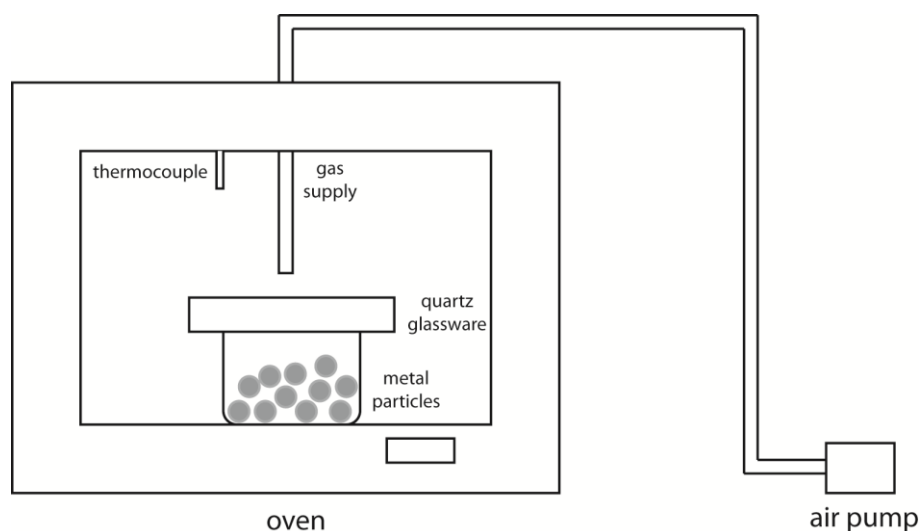


Figure 15: Visual observation experimental design

3.2.4. FT-IR Experiments

FT-IR technique provides qualitative information about vibrational spectra of certain sample. In the scope of this thesis, a gas cell apparatus was installed to Perkin Elmer Spectrum 100 FT-IR Spectrometer for detection of change in product gas of reactor output. Reactors used during the

experiments were designed and manufactured by following the criteria shown in Appendix D. Feed gas concentration was adjusted by dilution of CO₂ in an inert gas, using mass flow controllers (MFC). CO₂ flow rate was adjusted to 45ccpm. 495.9gr metallic lead was put into reactor. Then, heat was supplied to the system with a rate of 8°C/min. Product gas stream was sent to FT-IR's gas cell for continuous spectral measurement. Then, CO formation rate was observed from change in molecular vibrational energy of product gas. Finally, the output stream was sent to the hood as shown in Figure 17.

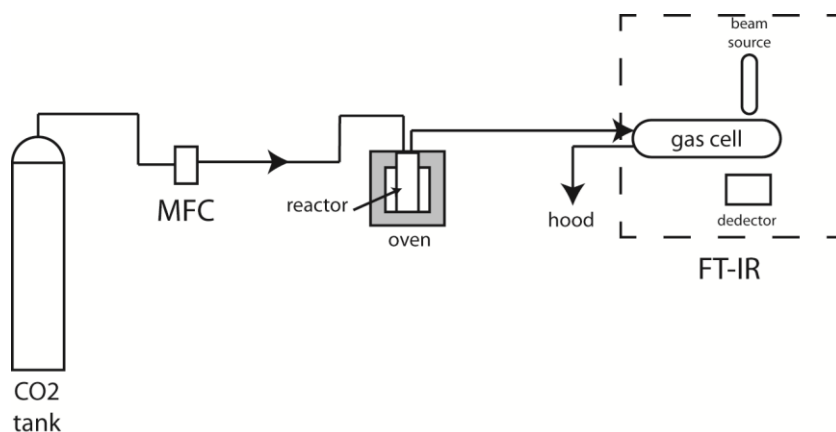


Figure 16: Experimental setup used for FT-IR measurement.

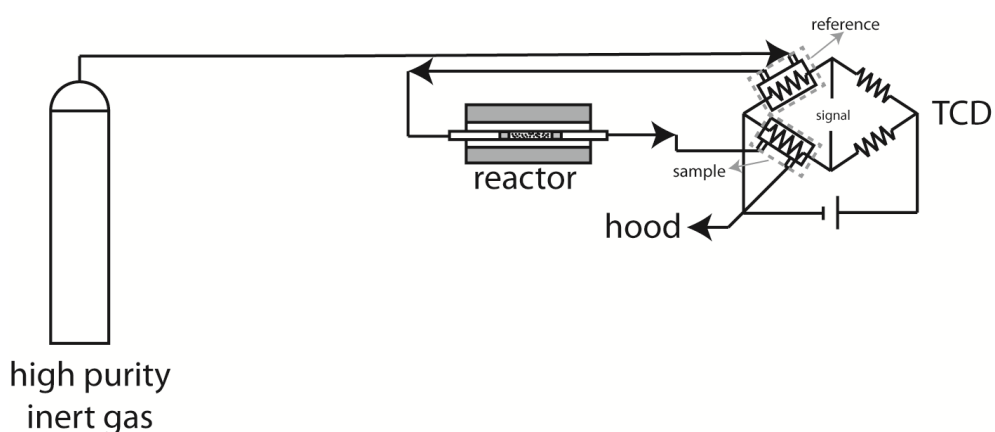


Figure 17: Thermal decomposition reactions experimental design

3.2.5. Temperature Programmed Desorption (TPD) Experiments

Experiments were performed for reduction performance of metal oxides. Column of HP4890A model gas chromatograph was removed. Chromatograph was configured as shown in Figure 17. Output of reference gas of TCD was directly connected to reactor inlet. Flow rate of reference gas were adjusted to 80ccpm. Then, product stream was sent to the sample gas part of TCD for measurement. After configuration, 150mg of selected materials were put in the reactor and heated with a rate of 10°C/min. Oxygen release amounts were determined by change in voltage output signal. Sweeping gas flowing rate was determined as 80ccpm.

3.2.5.1. Coal Oxidation Experiments

Coal oxidation experiments were carried out to show that oxygen released during thermal decomposition of metal oxide could be transferred to a carbon source such as coal. Therefore, reactor was prepared as two sections as shown in Figure 18: oxygen source part and coal part. Certain amounts of material were put in these sections such as 150mg metal oxide and 50mg coal. Flow rate of sweep gas adjusted to 50ccpm Ar. Reactor was heated with 10°C/min. Finally, product gas was analyzed by Mass Spectrometry.

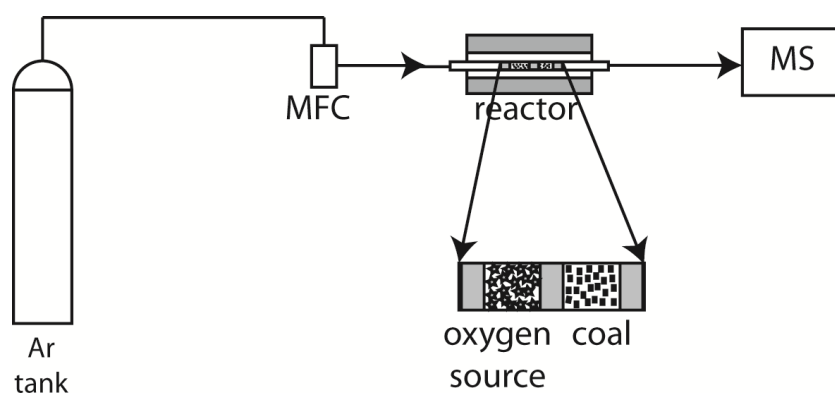


Figure 18: Coal oxidation experiment setup

CHAPTER 4

RESULTS

4.1. Thermodynamic Analysis

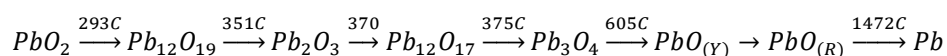
Selection of appropriate reducible oxides during syngas production requires thermodynamic background since relative strengths of oxidation and reduction processes are important for elimination of possible Me/MeOx pairs.

4.1.1. Ellingham Diagrams

Ellingham diagrams were prepared for comparing relative oxidative strengths of certain materials. In these diagrams molar Gibbs free energy of formation of the interested molecule (in this case, oxygen molecule) were plotted against temperature. Ellingham diagrams of some selected metal oxides were plotted in Figure 19. One can infer some conclusions about the stability of these compounds from Figure 19. Because, compounds become less stable as their free energy get close to $\Delta G_f^\circ(T) = 0$. For instance, metallic cerium can reduce any compound presented in Figure 19 while being oxidized itself. Zinc and iron also can reduce CO_2 to CO, C and H_2O to H_2 in order to oxidize themselves. Similar conclusion is true for carbon oxidation during coal or biomass oxidation. Lead and cobalt oxide can oxidize carbon and hydrogen. In other words, syngas production via metal oxides is possible only if selected metal oxide line is close to $\Delta G_f^\circ(T) = 0$.

Magnetite is less stable than ferrous oxide when their relative positions in Figures 19 and 20 were compared. This finding is also true for cobalt and lead oxides. Sufficient difference in chemical potentials between magnetite line and carbon oxidation line occurs at temperatures higher than 1200°C . Same difference was achieved at 130°C for Pb_3O_4 and at 630°C for Co_3O_4 .

Most commonly known lead and cobalt oxide pairs were plotted in Figure 21. It was observed that compounds become less stable as Me/O atomic ratio decreases. For instance, it is expected that PbO_2 will decompose first when lead oxide decomposition sequence is concerned. Then, decomposition of Pb_3O_4 and PbO will follow. This analysis also shows that cobalt oxide is more stable than lead oxide. When these two metal oxides exist in the same environment, cobalt will keep lead in reduced form in order to oxidize itself.



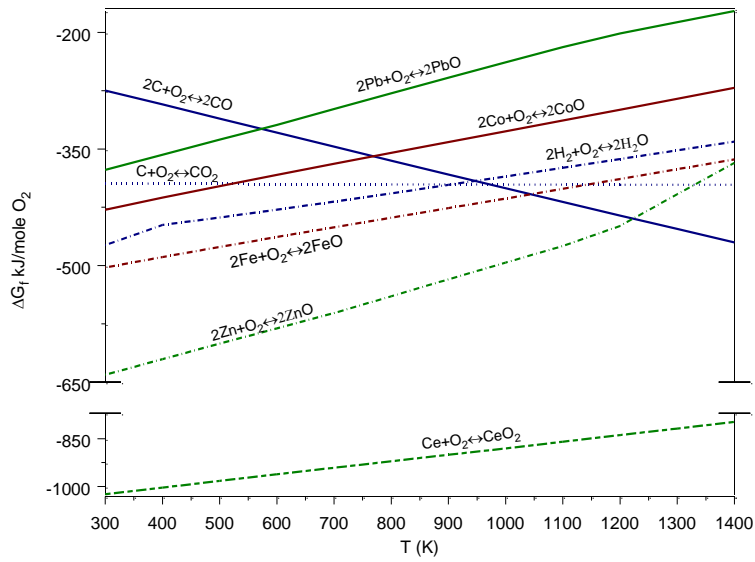
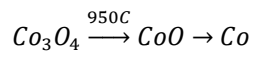


Figure 19: Relative oxidative strengths of some metal oxides at 1 bar.

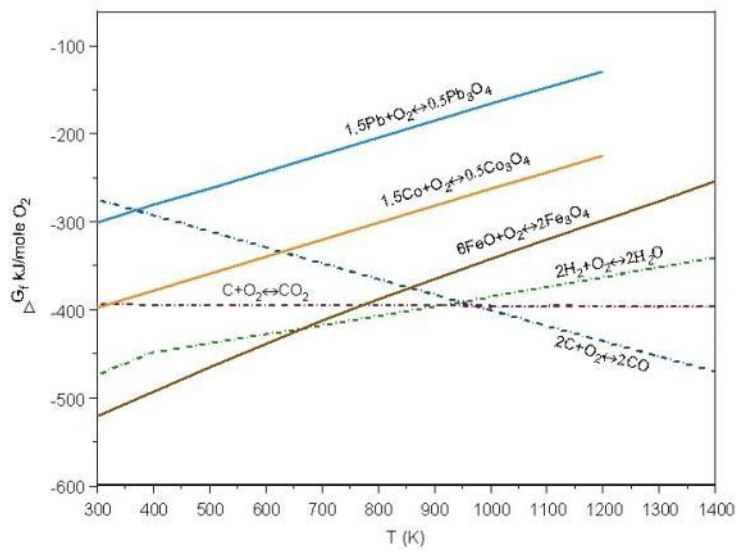


Figure 20: Oxidative strengths of metal oxides when Me/O=0.75 at 1 bar.

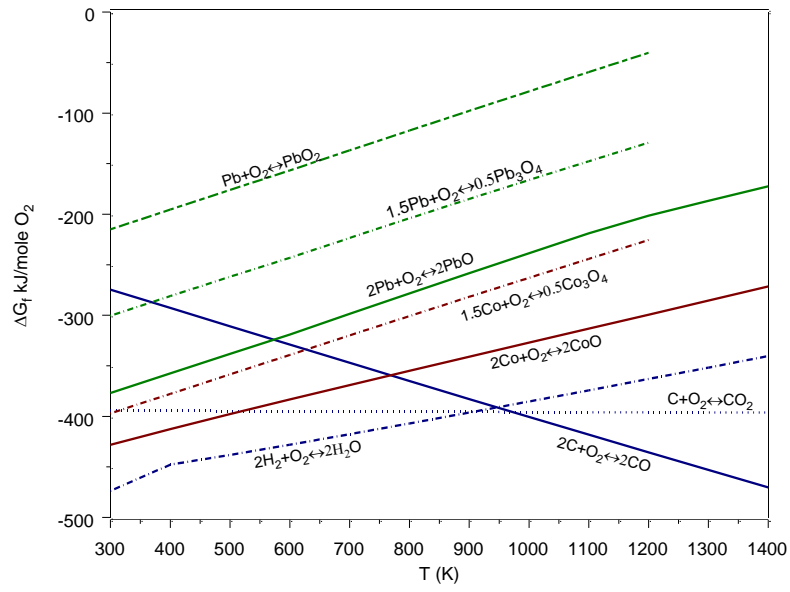


Figure 21: Oxidative strengths of generally available lead oxides and cobalt oxides at 1 bar.

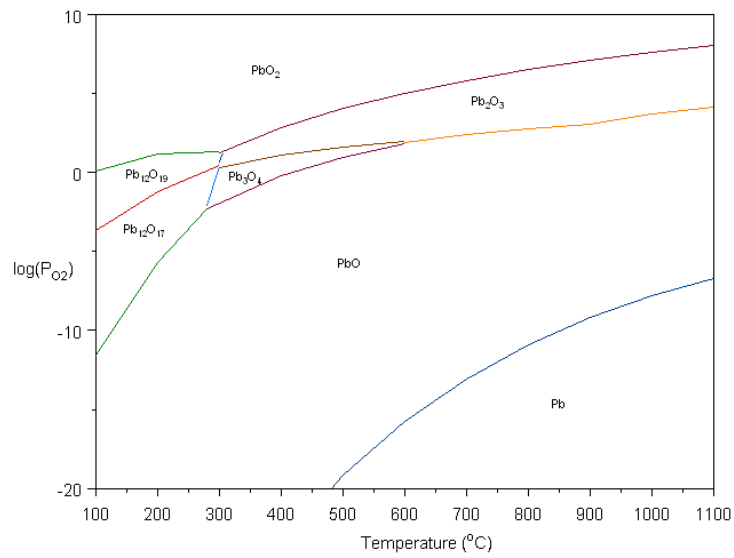
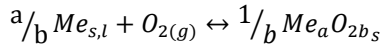


Figure 22: $P(O_2)$ vs. T diagram for Pb-O systems at 1 bar.

4.1.2. Predominance Diagrams

4.1.2.1. Metal Oxide Stability

Stability of metal oxide is determined by its formation equilibrium constant. For an arbitrary metal oxidation reaction, equilibrium constant was calculated by equation 4.1



$$K_{Me_{s,l} \leftrightarrow Me_a O_{2b_s}} = \frac{a_{Me_a O_{2b_s}}^{1/b}}{a_{Me}^{a/b} (P_{O_2}/P_0)} \quad (4.1)$$

By knowing the relationship between formation Gibbs free energy and equilibrium constant, metal oxide is stable only if equation 4.3 is satisfied.

$$\Delta G_{for}^o = -RT \ln K \quad (4.2)$$

$$P_{O_2} \geq \exp\left(\frac{\Delta G_{for}^o}{RT}\right) \quad (4.3)$$

Equation 4.3 constitutes the basis of predominance diagram of the metal oxide. A detailed account of the construction of Figure 22 was given in Appendix A. These diagrams were actually the rearrangement of the data available in Ellingham diagrams.

Predominant oxide forms of cobalt, lead and their oxides were plotted in Figure 22 and 23. It was seen that lead has more oxide forms than cobalt. Therefore, it can be concluded that oxygen can be stored in different forms of lead. Their oxide stability decreases as temperature increases. Therefore, they can decompose thermally to more stable forms.

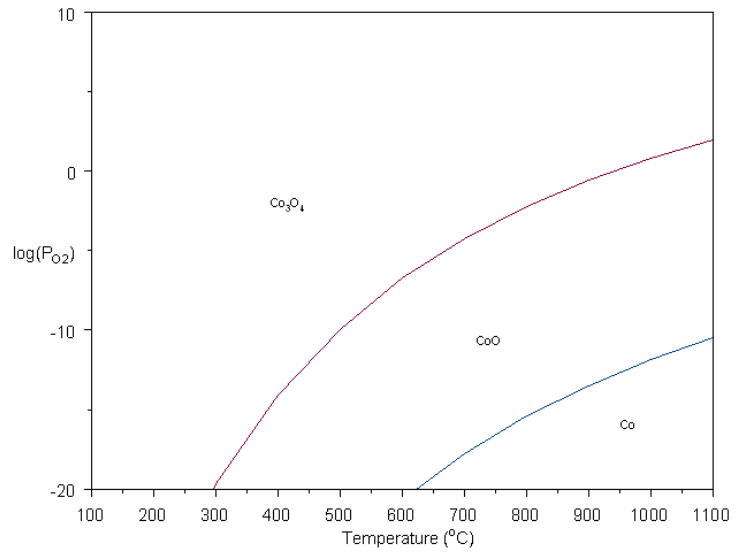


Figure 23: $P(O_2)$ vs. T diagrams for Co-O systems at 1 bar.

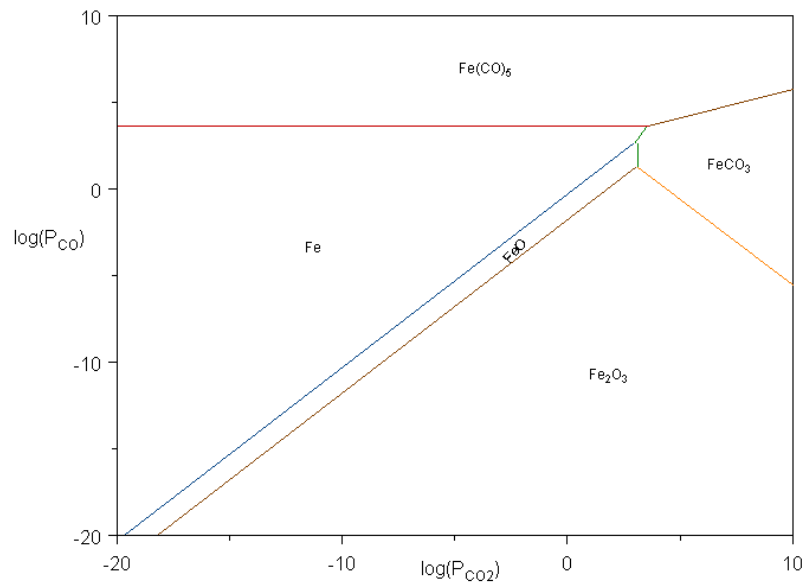


Figure 24: Fe/ CO_2 /CO system at 400°C and 1bar

4.1.2.2. Metal/Metal Oxide stability at CO₂/CO atmosphere

Stability of carbonate and oxide forms of iron was shown in Figures 24 and 25. It was found that iron can reduce CO₂ in order to oxidize itself. This tendency continues at high partial pressures of CO₂. In addition, when CO partial pressure increases, the system stabilizes itself by forming iron carbonates. Iron tends to form carbonates which show carbon capture capability at high CO₂ partial pressures and high carbon contents as shown in Figures 24 and 25.

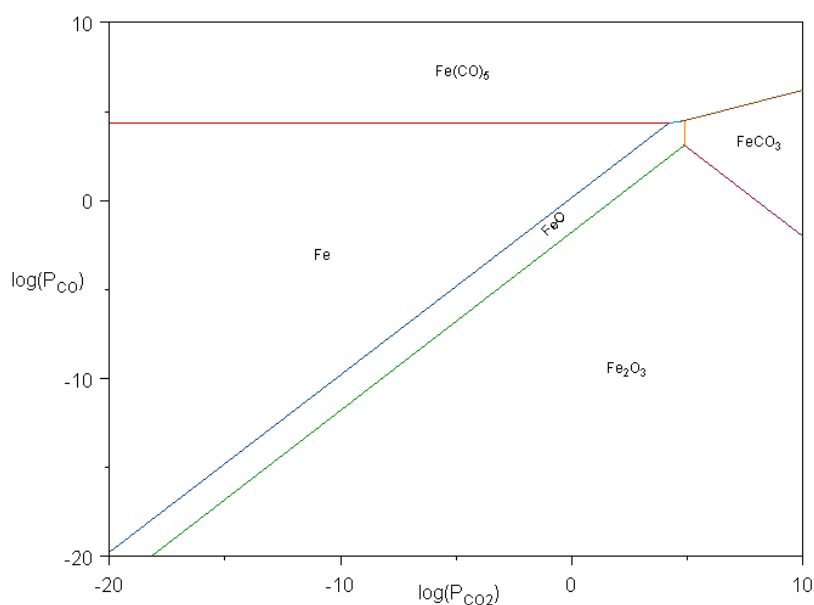


Figure 25: Fe/CO₂/CO system at 700°C and 1bar

Stability of lead with respect to temperature was shown in Figures 26 and 27. It was seen that lead oxidation by CO₂ reduction was possible at high CO₂ partial pressure and at very low CO partial pressures. As CO partial pressure increases, new crystal structures are formed as *PbO · PbCO₃* and *PbCO₃*. In addition, system tolerance to high CO environment increases as temperature increases.

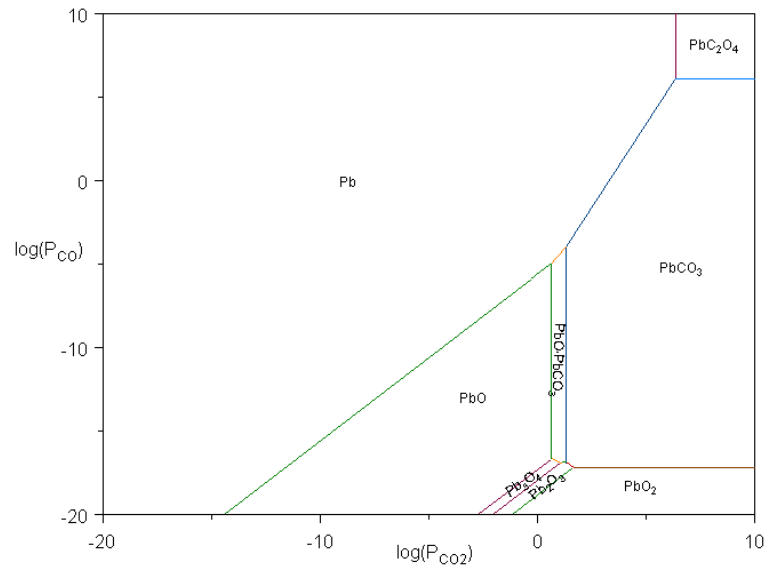


Figure 26: Pb/CO₂/CO system at 400°C and 1bar

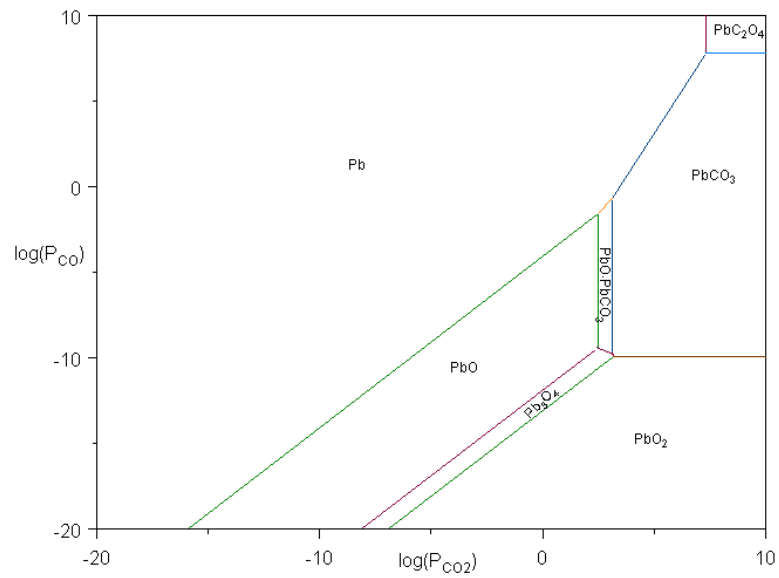


Figure 27: Pb/CO₂/CO system at 700°C and 1bar

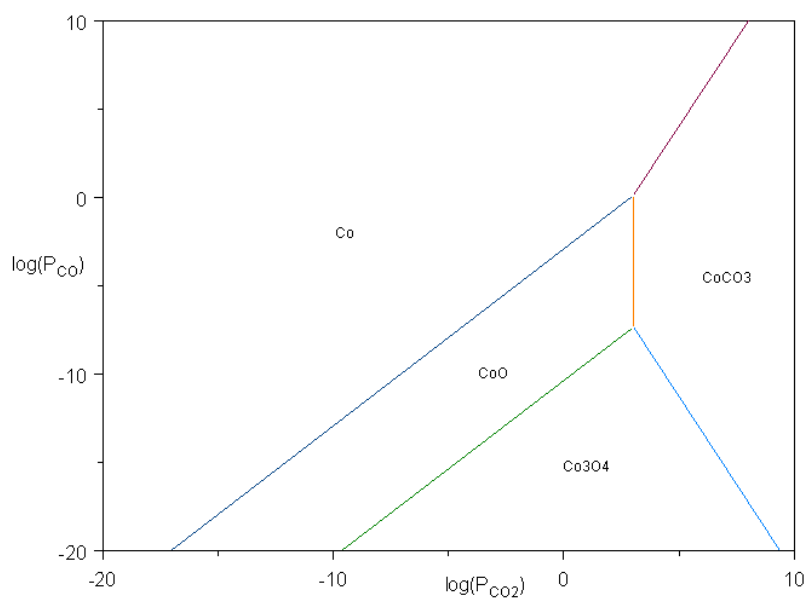


Figure 28: Co/CO₂/CO system at 400°C and 1bar

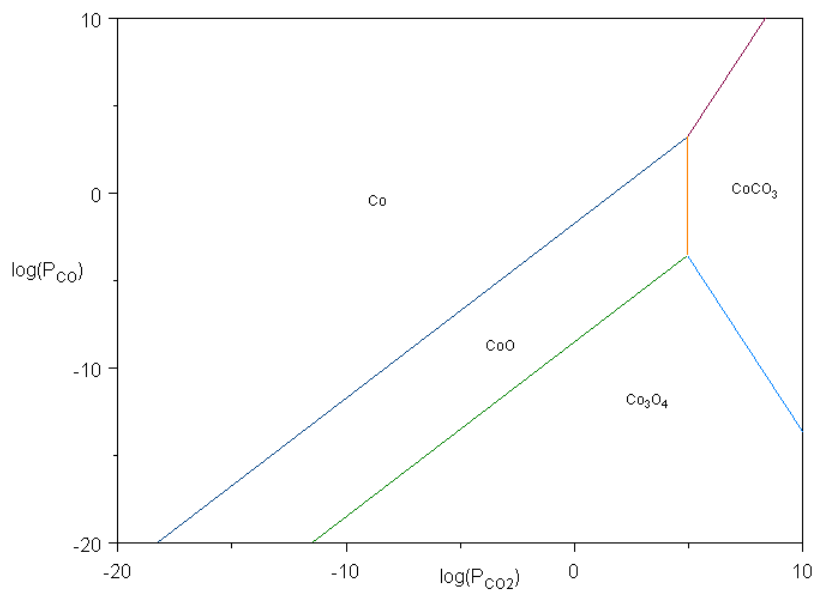


Figure 29: Co/CO₂/CO system at 700°C and 1bar

Predominance diagram of cobalt under CO/CO₂ atmosphere was shown in Figures 28 and 29. These diagrams can be used to identify the compounds predominantly present given the temperature and the atmosphere. For example, we can easily conclude that Co can be oxidized easier than lead when CO₂ is the oxidizing agent.

4.1.2.3. Stability of Sulfur containing Compounds

Since these materials are intended for coal processing, sulfur, one of the most critical compounds in coal structure, needs to be addressed as well. For this purpose, stability of sulfur compounds was determined.

Stability of iron oxides and iron sulfates were shown in Figures 30 and 31. Iron tends to absorb sulfur in its structure as $FeSO_4$ and $Fe_2(SO_4)_3$ at high O₂ and high SO₂ partial pressures. These compounds become unstable with increase in temperature so probability of sulfur capturing decreases at high temperatures. In addition, when $P_{O_2} = 0.21\text{bar}$, iron sulfate formation is restricted at low SO₂ concentrations as shown in Figure 32.

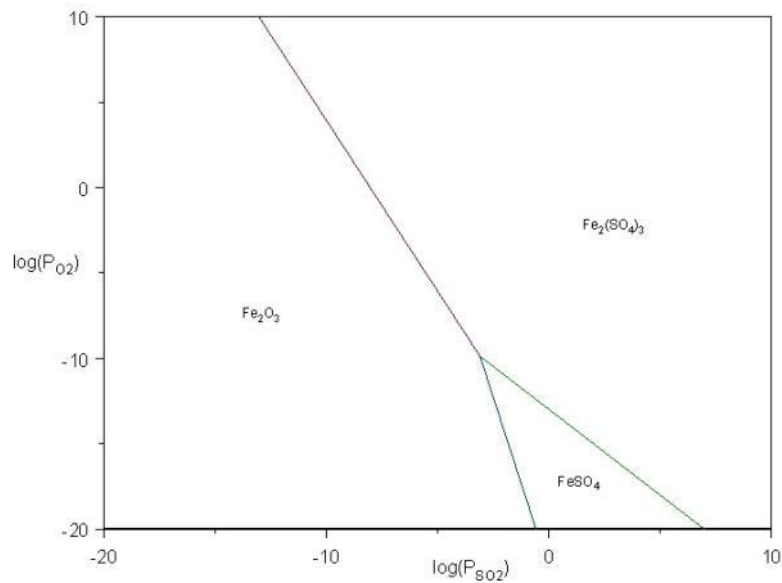


Figure 30: Predominance diagram for Fe-S-O system at 400°C and 1 bar

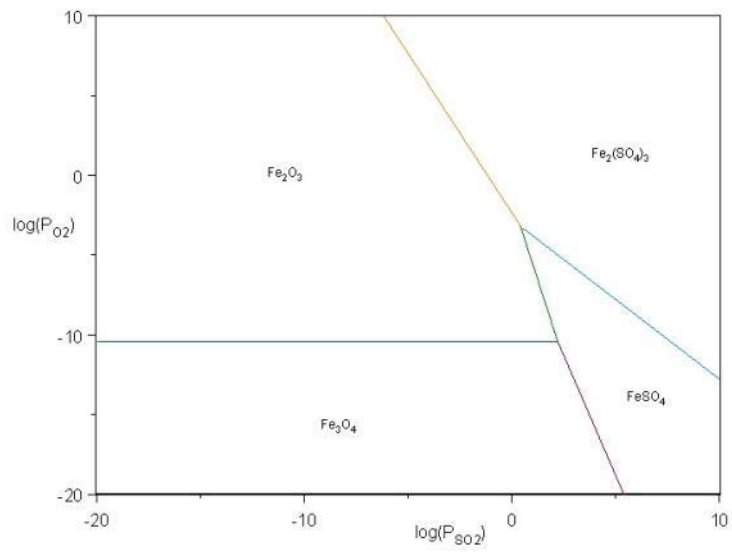


Figure 31: Predominance diagram for Fe-S-O system at 700°C and 1 bar

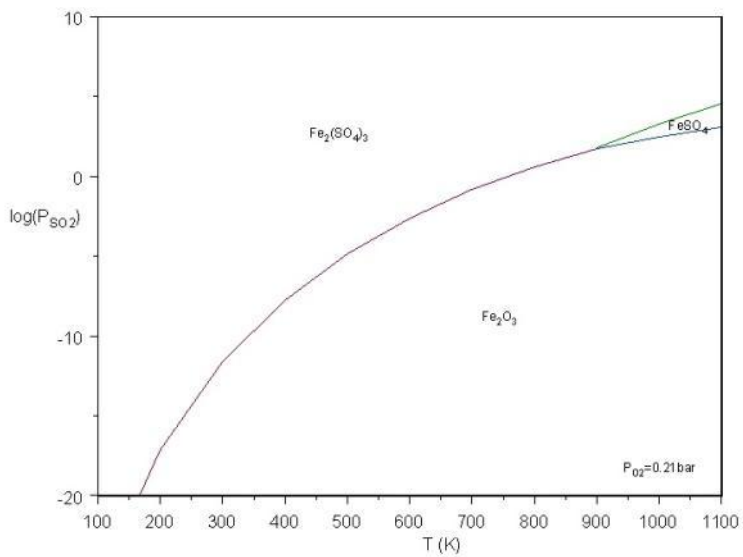


Figure 32: Predominance diagram for Fe-S-O system at $P_{O_2}=0.21$ bar

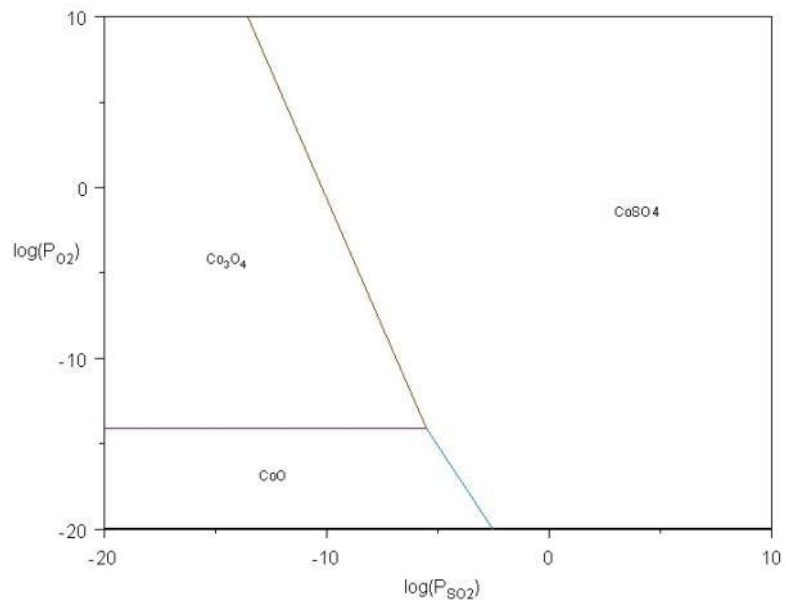


Figure 33: Predominance diagram for Co-S-O system at 400°C and 1 bar

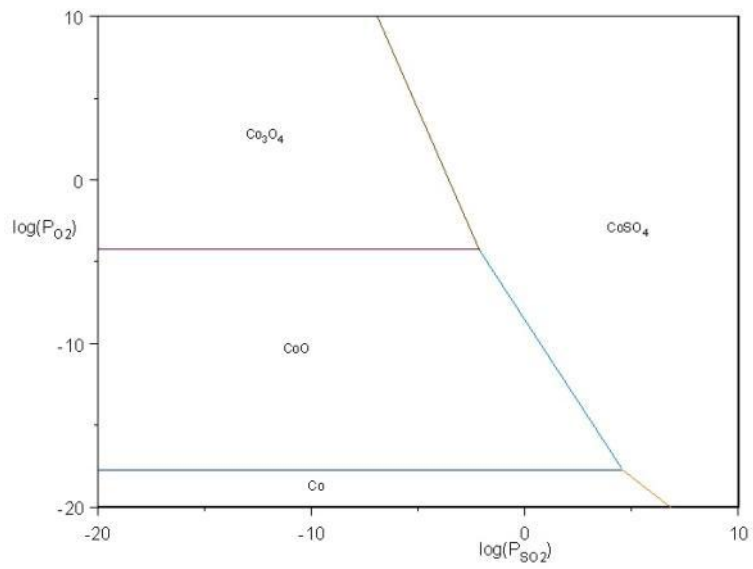


Figure 34: Predominance diagram for Co-S-O system at 700°C and 1 bar

Stability of cobalt oxides and sulfates were examined at 400°C and 700°C as shown in Figures 33 and 34. Similar findings were found as in Fe-S-O system. Nevertheless, cobalt has only one sulfate composition as CoSO_4 . Its stability is decreased with increasing temperature. In addition, sulfur capturing is limited at low SO_2 concentrations when $P_{\text{O}_2} = 0.21\text{bar}$ as shown in Figure 35.

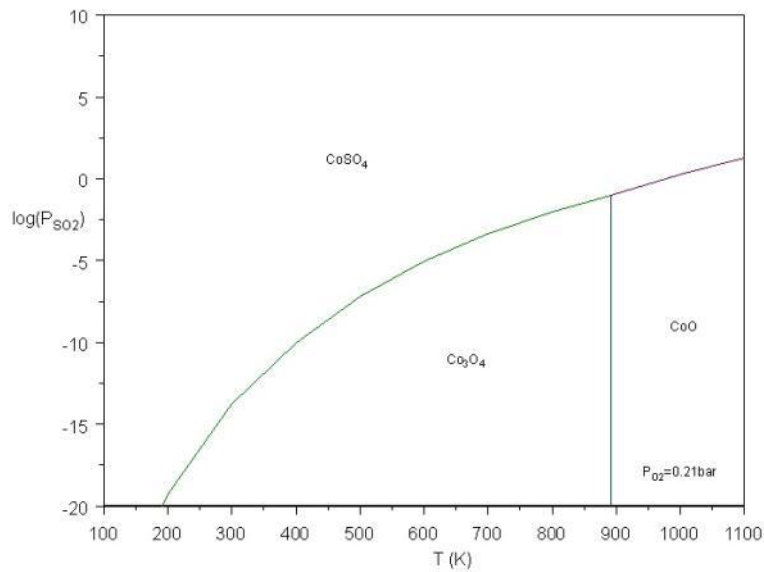


Figure 35: Predominance diagram for Co-S-O system at $P_{\text{O}_2} = 0.21\text{bar}$

Lead has more tendency to absorb sulfur compounds such as PbSO_4 , $\text{PbO} \cdot \text{PbSO}_4$, $2\text{PbO} \cdot \text{PbSO}_4$, $4\text{PbO} \cdot \text{PbSO}_4$ and PbS forms as stated in Figures 36 to 38. These compounds are stable in a very wide range in both temperatures. In addition, all sulfur involving lead compounds have a temperature resistance even at low SO_2 contents.

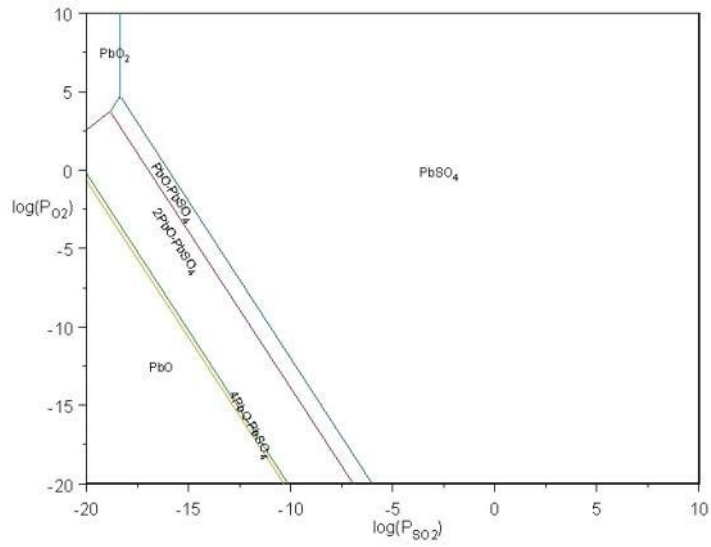


Figure 36: Predominance diagram for Pb-S-O system at 400°C and 1 bar

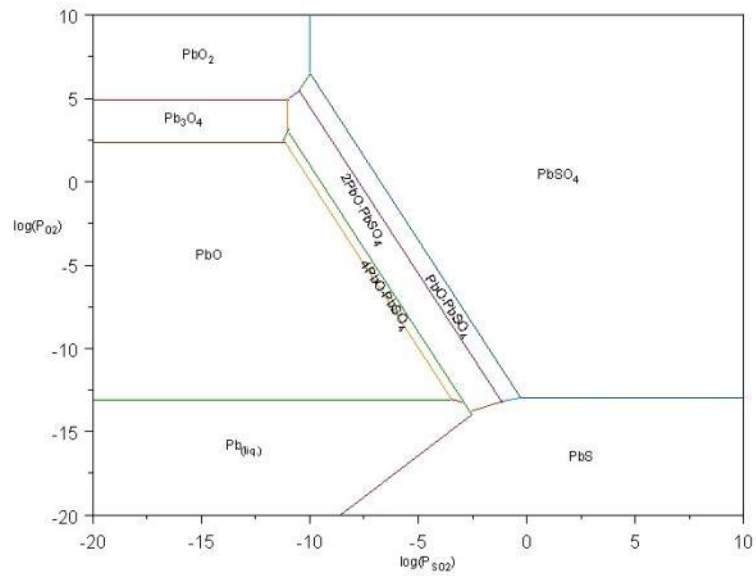


Figure 37: Predominance diagram for Pb-S-O system at 700°C and 1 bar

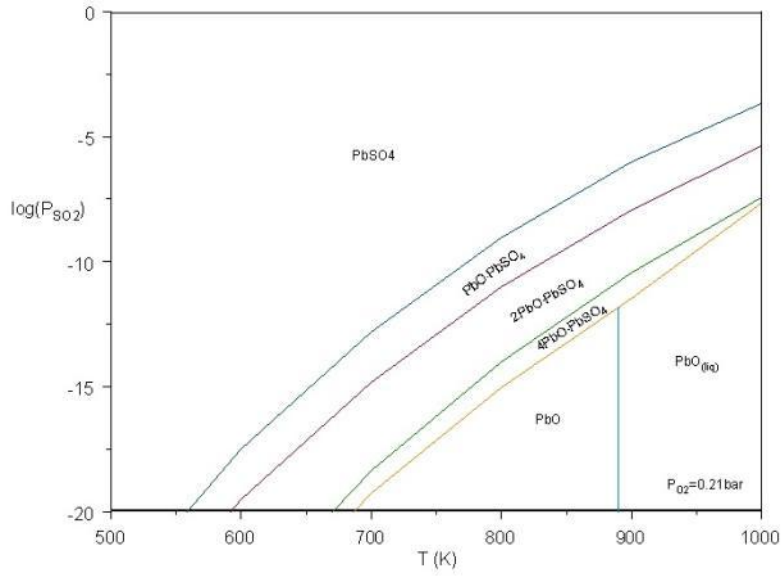


Figure 38: Predominance diagram for Pb-S-O system at $P_{O_2}=0.21\text{bar}$

Table 6: Enthalpies of lead oxide decomposition reactions

Decomposition Reactions	ΔH_{298K}°
$4.8PbO_2 \rightarrow 0.4Pb_{12}O_{19} + O_2$	181.4kJ/mole O_2
$2Pb_{12}O_{19} \rightarrow 12Pb_2O_3 + O_2$	325.1kJ/mole O_2
$12Pb_2O_3 \rightarrow 2Pb_{12}O_{17} + O_2$	-167.9kJ/mole O_2
$2Pb_{12}O_{17} \rightarrow 8Pb_3O_4 + O_2$	318.0kJ/mole O_2
$2Pb_3O_4 \rightarrow 6PbO_{(Y)} + O_2$	128.8kJ/mole O_2
$PbO_{(Y)} \rightarrow PbO_{(R)}$	-0.5kJ/mole O_2
$2PbO_{(R)} \rightarrow 2Pb + O_2$	437.4kJ/mole O_2

4.1.3. Energy Analysis

Required energy for breaking existing bonds or forming new bonds determines the energy input or output to the system. Lead has various oxide forms. By taking metallic lead as a starting point, lead monoxide formation had the greatest energy output as shown in Table 6. Depending on the new formed crystal structure, some transformations become exothermic whereas some becomes

endothermic. Few forms were observed for cobalt in terms of oxide transformation. Nevertheless, it was observed that energy released during the oxidation of cobalt supplies more energy as shown in Table 7 than lead when same reactions are concerned.

Table 7: Enthalpies of cobalt oxide decomposition reactions

Decomposition Reactions	ΔH_{298K}°
$2Co_3O_4 \rightarrow 6CoO + O_2$	392.1kJ/mole O_2
$2CoO \rightarrow 2Co + O_2$	476.2kJ/mole O_2

Table 8: Equilibrium analysis of C-S-O system

Feedstock in atomic basis	Inputs (moles)	Material expected to be in equilibrium
C	1	C
S	0.05	S
O	0.5; 1;3	CO
Temperature	400K-1300K	CO ₂
Pressure	0.1-1-10 bar	SO ₂
		O ₂

4.1.4. Equilibrium Analysis

4.1.4.1. C-S-O system

C-S-O system was selected as a basis for further calculations. In this manner, system limitations were determined as in Table 8. Compositions that minimize system Gibbs free energy at various temperature and pressures were plotted as Figures 39 to 41. Breakeven point of CO dominant region was affected by pressure directly with a shift from 850K to 1050K for the case when oxygen carbon ratio was 0.5. In addition, this shift was same as for other calculations done in different feedstocks. Therefore, only results at 1 bar were shown in following parts of this section while other calculations were demonstrated in Appendix C.

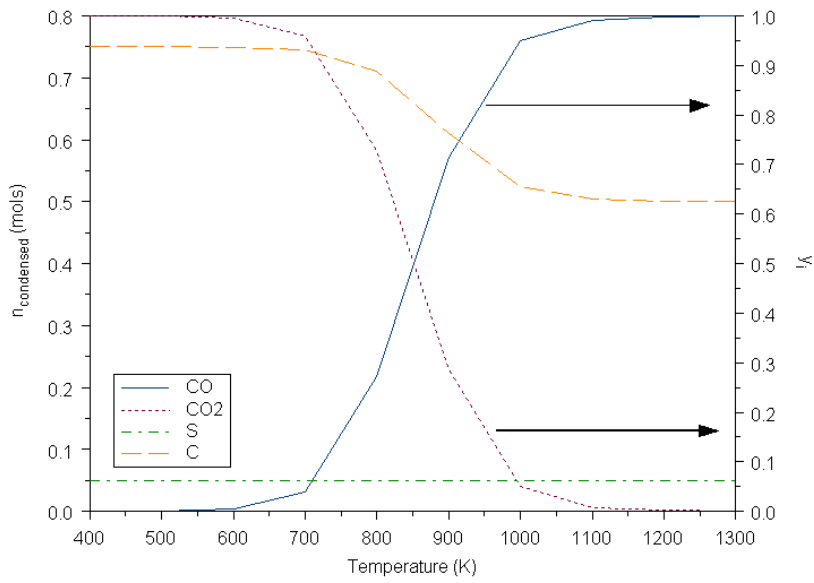


Figure 39: Equilibrium composition of a system of 1 mol C, 0.05 mol S and 0.5 mol O at 0.1 bars.

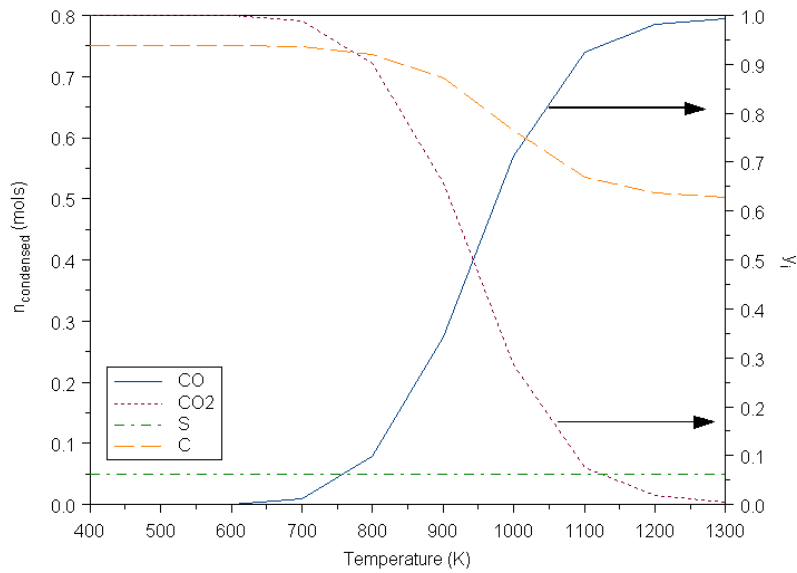


Figure 40: Equilibrium composition of a system of 1 mol C, 0.05 mol S and 0.5 mol O at 1 bar

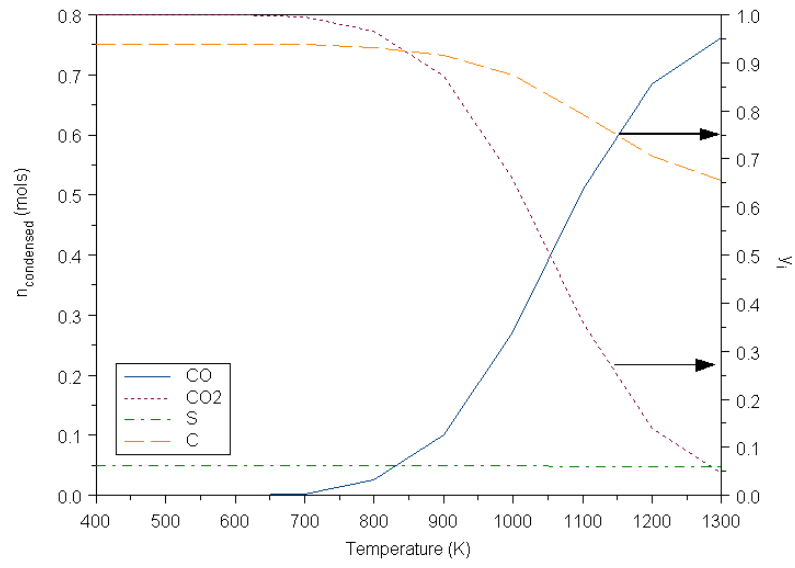


Figure 41: Equilibrium composition of a system of 1 mol C, 0.05 mol S and 0.5 mol O at 10 bars

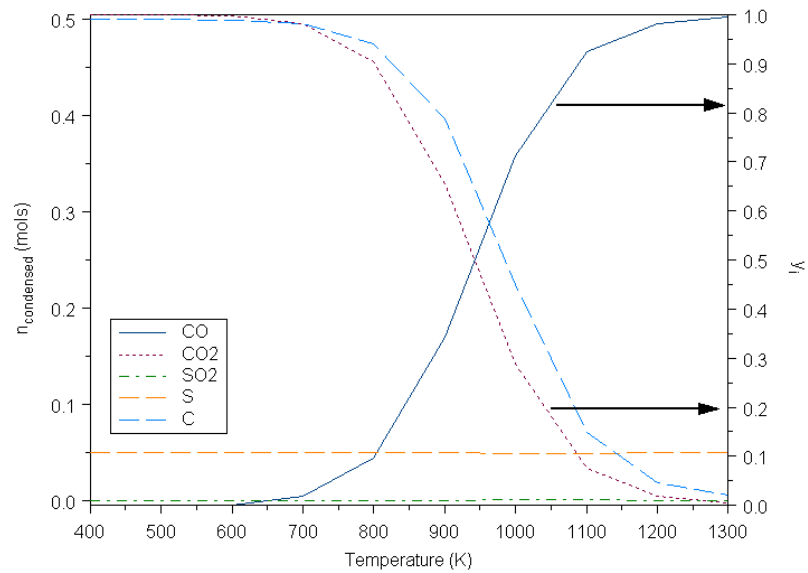


Figure 42: Equilibrium composition of a system of 1 mol C, 0.05 mol S and 1 mol O at 1 bar

Minimization results at different carbon oxygen ratios at 1 bar were shown in Figure 40, 42 and 43. As oxygen concentration increases unconverted carbon started to react with more oxygen. In addition, it was seen that oxygen reacts first with carbon. Then, sulfur dioxide formation was observed. This may lead the conclusion that low SO_x emissions can be achieved at controlled oxidizing atmospheres when equilibrium was considered. One final conclusion is that no change in product composition with temperature was observed when excess oxygen was present as shown in Figure 43.

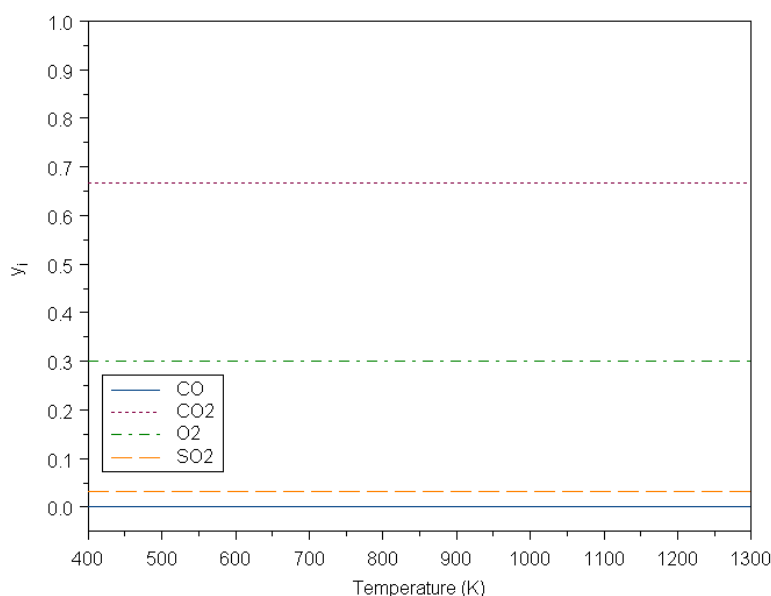


Figure 43: Equilibrium composition of a system of 1 mol C, 0.05 mol S and 3 mol O at 1 bar

4.1.4.2. C-S-O-Pb system

Reactants and products were expected to be in equilibrium were stated in Table 9. It was found that carbon can reduce lead oxide to oxidize itself as shown in Figure 44 to 46. In addition, carbon conversion was affected as temperature increases due to $CO_2 + C \leftrightarrow 2CO$ reaction. Results of C-S-O-Pb system were very similar with C-S-O system since lead oxide decomposed directly to metallic lead and oxygen molecule at studied range. Formed metallic lead reacts with elemental sulfur to produce PbS. During the calculations, PbSO₄ formation was also tested. Nevertheless, calculations showed that at studied environments, most stable compound is appeared to be PbS. SO₂ production becomes favorable at high temperatures by reduction of lead oxide followed by reaction with PbS as it was concluded from Figure 46. In addition, tests of possibility of various lead oxide formations were also investigated. Nevertheless, it was seen that PbO was only stable compound in condensed phase.

Table 9: Compounds expected to be in equilibrium for C-S-O-Pb

Feedstock in atomic basis	Inputs (moles)	Compounds expected to be in equilibrium
C	1	C
S	0.05	S
O	0.5; 1;3	CO
Pb	0.5; 1;3	CO ₂
Temperature	400K-1300K	SO ₂
Pressure	0.1-1-10 bar	O ₂
		Pb
		PbO
		PbS
		PbSO ₄

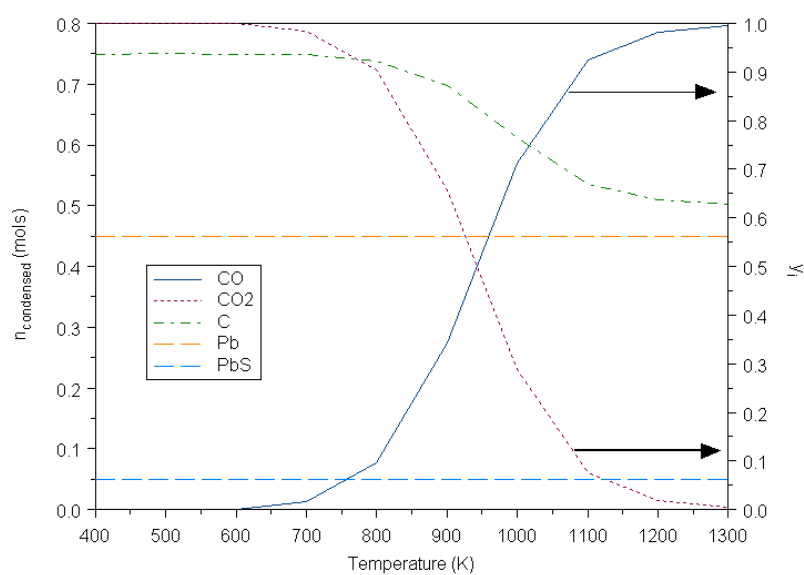


Figure 44: Equilibrium composition of a system of 1 mol C, 0.05 mol S, 0.5 mol Pb and 0.5 mol O at 1 bar

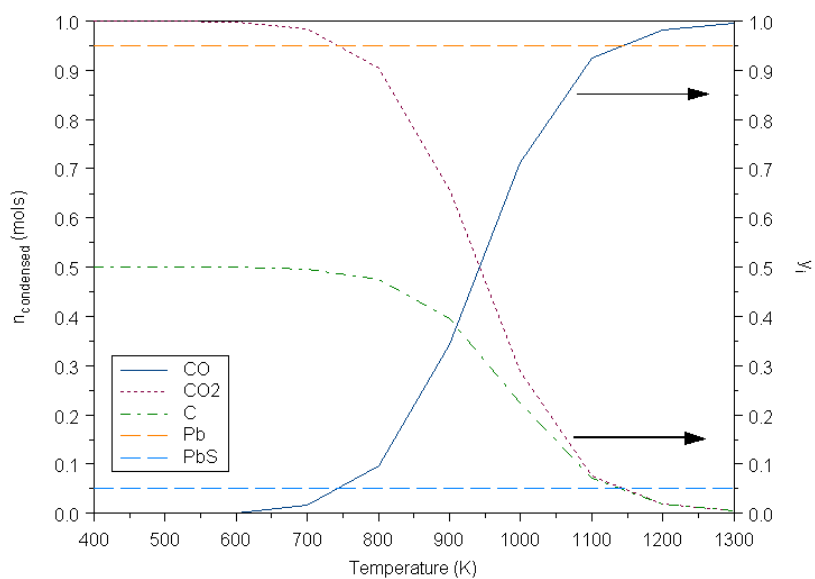


Figure 45: Equilibrium composition of a system of 1 mol C, 0.05 mol S, 1 mol Pb and 1 mol O at 1 bar

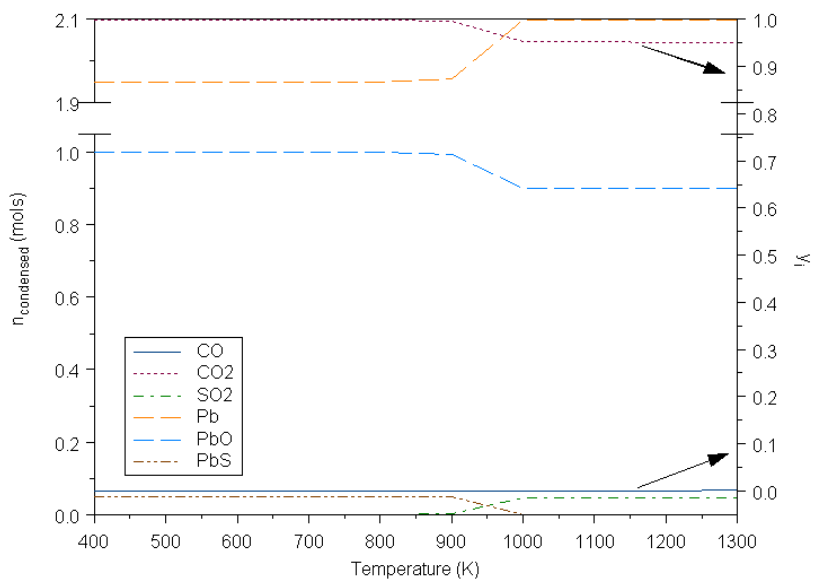


Figure 46: Equilibrium composition of a system of 1 mol C, 0.05 mol S, 3 mol Pb and 3 mol O at 1 bar

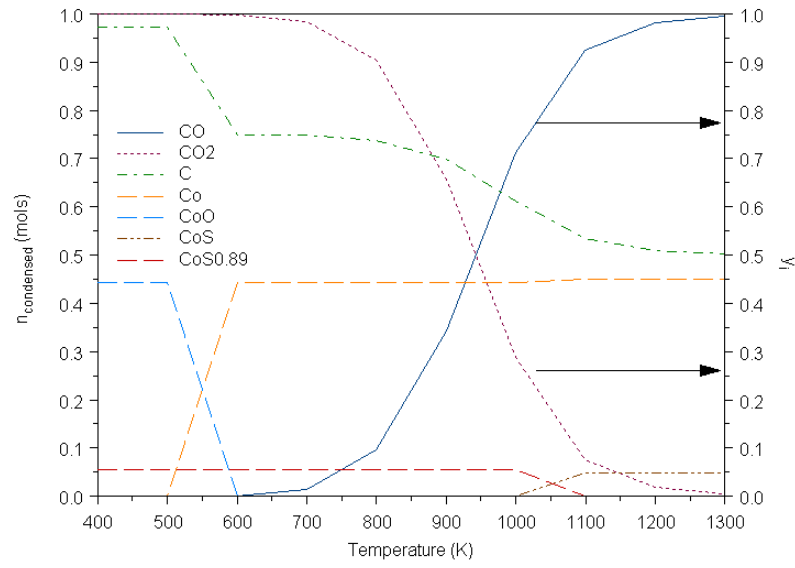


Figure 47: Equilibrium composition of a system of 1 mol C, 0.05 mol S, 0.5mol Co and 0.5mol O at 1 bar

Table 10: Compounds expected to be in equilibrium for C-S-O-Co

Feedstock in atomic basis	Inputs (moles)	Compounds expected to be in equilibrium
C	1	C
S	0.05	S
O	0.5; 1;3	CO
Co	0.5; 1;3	CO ₂
Temperature	400K-1300K	SO ₂
Pressure	0.1-1-10 bar	O ₂
		Co
		CoO
		CoS
		CoSO ₄
		CoS _{0.89}

4.1.4.3. C-S-O-Co system

Reactants and products were expected to be in equilibrium were stated in Table 10. It was found that cobalt has higher affinity to sulfur since below 600K formed CO_2 was only due to the reaction of sulfur with CoO . In other words, CoO reduction is only due to the presence of elemental sulfur not carbon as in the case of lead. As temperature increases, CoO reduction becomes favorable. CO_2 and CO formation starts and consumes all available carbon in the system as shown in Figures 47 and 48. Nevertheless, this finding becomes invisible when excess oxygen was present as shown in Figure 49. Another important conclusion with sulfur metal interaction was that CoS transforms to $\text{CoS}_{0.89}$ as available cobalt site and temperature increases.

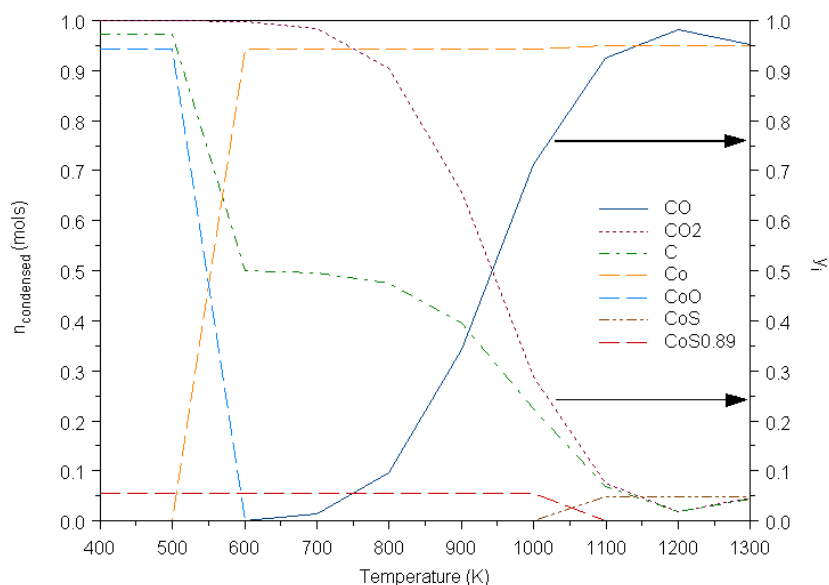


Figure 48: Equilibrium composition of a system of 1mol C, 0.05 mol S, 1mol Co and 1mol O at 1 bar

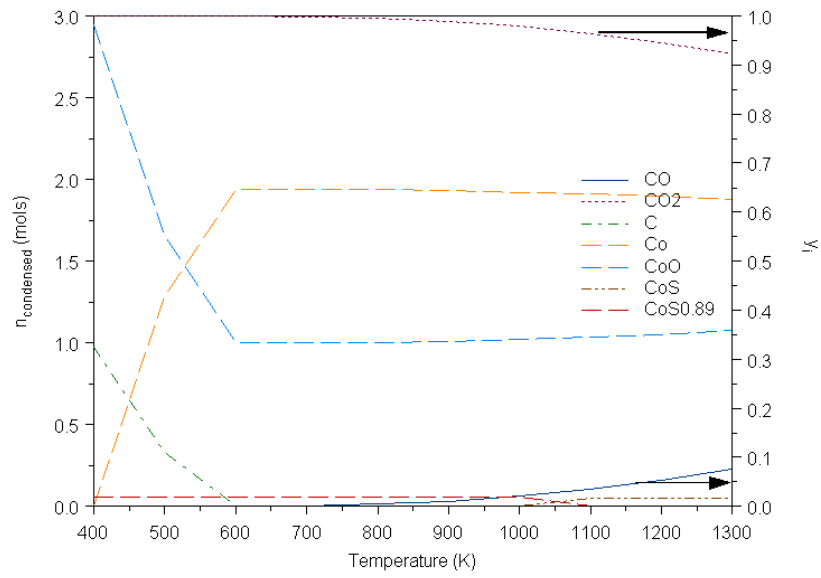


Figure 49: Equilibrium composition of a system of 1 mol C, 0.05 mol S, 3 mol Co and 3 mol O at 1 bar

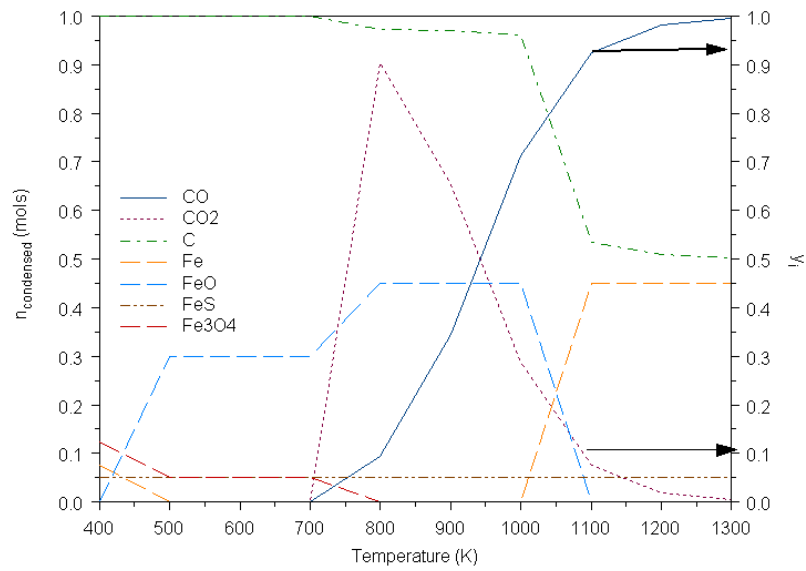


Figure 50: Equilibrium composition of a system of 1 mol C, 0.05 mol S, 0.5 mol Fe and 0.5 mol O at 1 bar

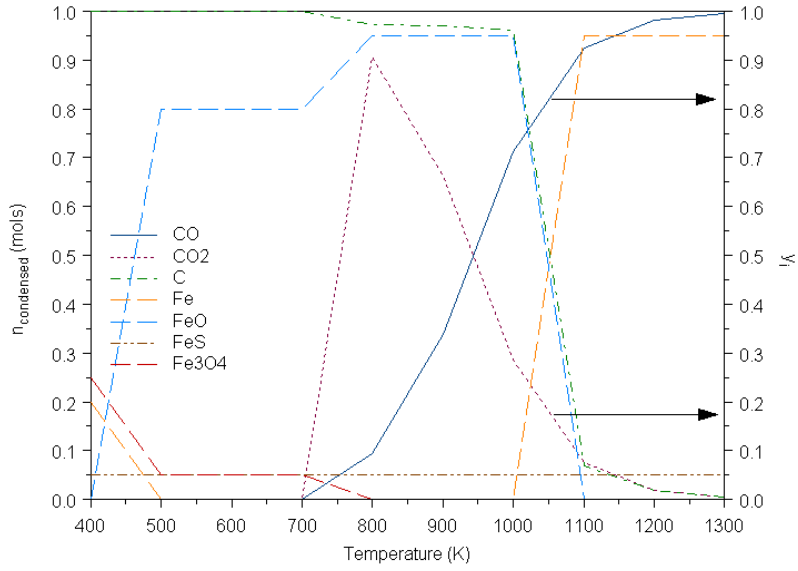


Figure 51: System of 1mol C, 0.05 mol S, 1mol Fe and 1mol O at 1 bar

Table 11: Compounds expected to be in equilibrium for C-S-O-Pb

Feedstock in atomic basis	Inputs (moles)	Compounds expected to be in equilibrium
C	1	C
S	0.05	S
O	0.5; 1;3	CO
Fe	0.5; 1;3	CO ₂
Temperature	400K-1300K	SO ₂
Pressure	0.1-1-10 bar	O ₂
		Fe
		FeO
		FeS
		FeSO ₄
		Fe ₂ O ₃
		Fe ₃ O ₄

4.1.4.4. C-S-O-Fe system

Reactants and products were expected to be in equilibrium were stated in Table 11. Iron oxides were not reactive with carbon as shown in Figure 50 to 52. It was found that most stable compound in equilibrium is Fe_3O_4 at low temperatures. Nevertheless, Fe_3O_4 starts to decompose and form FeO as temperature increases. Formed iron reacts with elemental sulfur to produce FeS . Carbon oxidation starts after 700K. Formation of CO_2 and CO starts at same time. Nevertheless, these formations were limited with low carbon conversion up to 1000K. Then, required oxygen was supplied by reduction of FeO so that it oxidizes elemental carbon.

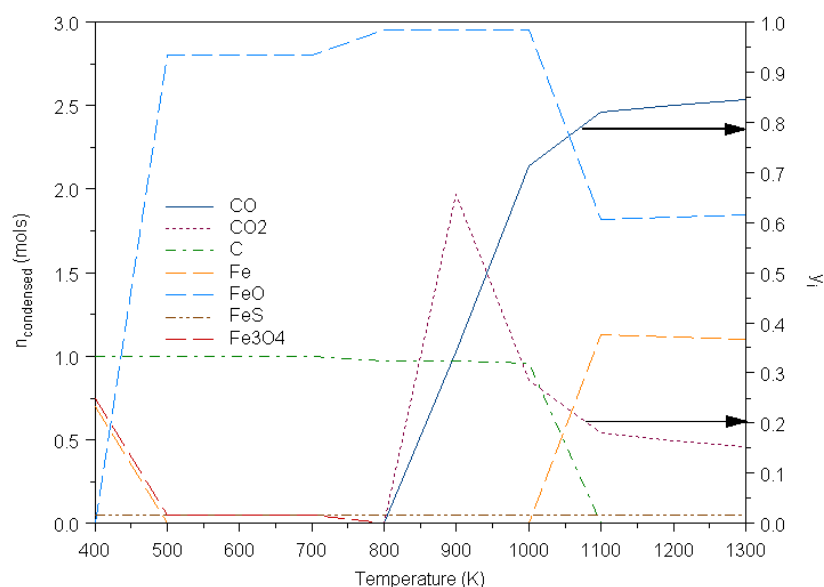


Figure 52: Equilibrium composition of a system of 1 mol C, 0.05 mol S, 3 mol Fe and 3 mol O at 1 bar

4.2. Experimental Results

It was concluded from thermodynamic analysis that lead and cobalt oxides can be used for carbon oxidation at various temperature and pressures. It was found that as temperature increases CO formation becomes favorable. Another conclusion was that metal oxide stability affects the oxygen concentration in the system which can control the formed CO_2 at equilibrium. Experimental verification of these findings was presented in this section.



Figure 53: Metallic lead oxidation in air atmosphere from 20°C to 800°C.

4.2.1. Visual Observation Experiments

Visual observations were done by taking pictures at predetermined oxidation temperatures. Color variations at the surface during oxidation of lead are shown in Figure 53. Up to melting point of lead, no oxide layer was observed. Further increase in temperature resulted in a thin oxide layer which thickened up to 600°C. After a point, oxidation proceeded with oxygen transfer from surface by solid state diffusion. Then, oxidized lead started to change its oxidation state by reacting more oxygen so higher O/Pb ratios were obtained. This can be understood from color change by temperature increase by knowing that metallic lead has a gray color whereas PbO has yellow and/or red depending on crystal structure, Pb₃O₄ has light red and PbO₂ has brown and/or dark red color. After reaching final set temperature 800°C, lead oxide started to melt. Nevertheless, an interesting thing was observed as it cooled down. During phase transformation, surface relaxation results with thermal decomposition. Thus, lower oxidation states are observed as metallic lead and PbO from higher ones; Pb₃O₄, PbO₂. These unstable oxide forms restrict the maximum oxidation temperature since oxidation becomes unfavorable and thermal decomposition becomes easier at higher temperatures. In other words, higher energy levels can easily deform crystal lattice to more stable ones.

Second part of visual observation experiments were done in reactor A for observing real situation. Experimental procedure was shown in Appendix E. It was known from first part that oxidation was favorable up to 700°C. Stable metal oxides can be obtained around this temperature. Second part mainly examined this conclusion at air atmosphere and H₂O atmosphere in a real reactor environment. Shooting photos were shown in Figure 54. It is found that metallic lead can be oxidized in both air and steam atmospheres and stable forms of lead oxides could be obtained at around 700°C. Oxidation in air atmosphere results with oxides with higher oxidation states whereas in steam atmosphere this seems to be restricted. In other words, oxidation in air atmosphere seemed more favorable. This conclusion was simply based on color difference. Formation of Pb₃O₄ and PbO₂ was observed as red colors at the surface in air atmosphere while almost uniform PbO was seen in steam atmosphere. This confirmed that capturing oxygen from air is easier than H₂O so that higher oxidation degrees are more achievable at air atmosphere.



Figure 54: Metallic lead oxidation in air (left) and steam (right) atmosphere at 700°C.

4.2.2. CO₂ Reduction Experiments

Overall experimental results were shown in Figure 55. It was observed that CO formation was not favorable up to 400°C. CO₂ reduction by lead began after 400°C. Lead oxidation by CO₂ reduction fastened after 600°C. Intensity of CO absorbance band increased almost double when reactor temperature reached to 700°C. CO formation seemed more favorable around 800°C.

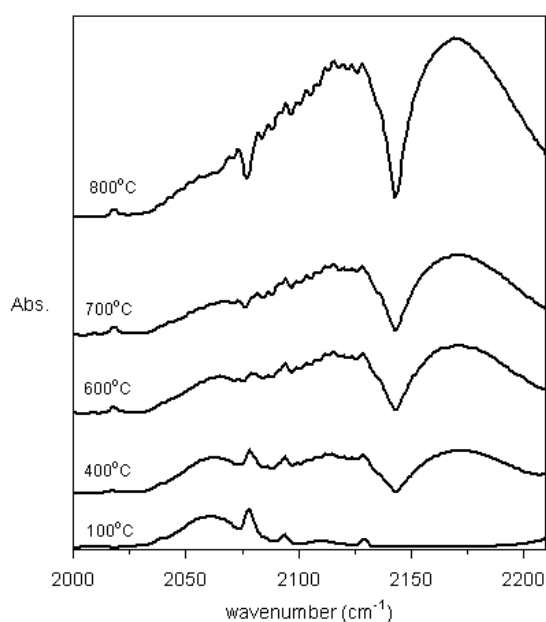


Figure 55: CO formation band at different temperatures.

4.2.3. Coal Oxidation via Reducible Metal Oxides

Thermodynamic analysis showed that reducible metal oxides can be used for carbon oxidation depending on their oxidation and reduction ability. Therefore, carbon source oxidation experiments were conducted by considering Turkish lignite as carbon source. Highest oxygen release per gr available oxygen in the materials was determined by TPD analysis. These materials were further used for coal oxidation experiments to observe CO and CO₂ evaluation.

4.2.3.1. Characterization

4.2.3.1.1. Coal Characterizations

Synthesized materials were further tested as oxygen carriers for coal gasification process. Turkey's coal reserves are generally classified as low quality coal due to their high ash content and low calorific value. In our laboratory, we had lignite coal samples from Tuncbilek region. This coal has a content of ~30wt% fixed carbon which is expected to form reactive char after moisture release and pyrolysis as stated in Table 12. Then, ultimate analysis was done for determining its sulfur content. The sulfur content this coal was around ~5.5wt% which is actually pretty high as stated in Table 13. Carbon to sulfur ratio of this coal is calculated as 20 (mol/mol).

Table 12: Proximate analysis

	wt%
Volatile matter	27.9 ± 0.1
Fixed carbon	29.5 ± 0.1
Ash	37.9 ± 0.2
Moisture	4.7 ± 0.9
Calorific value (cal/g)	3680 ± 60

Table 13: Ultimate Analysis

	wt%
C (%)	37.7 ± 0.7
H₂ (%)	3.6 ± 0.1
N₂ (%)	1.6 ± 0.1
S (%)	5.4 ± 0.6

4.2.3.1.2. Metal Oxide Characterization

Characterizations of PbOx, CoOx, Pb/Co=3 (wt./wt.) and 1wt.Pt% CoOx(5.5wt%)-Al₂O₃ were shown in Figure 56. CoOx was in the form of Co₃O₄ structure. Only alumina structures were observed during the characterization of 1wt.Pt% CoOx(5.5wt%)-Al₂O₃. Cobalt oxides peaks seems not easily differentiable from alumina due to weight ratio. PbOx has various crystal structures. Nevertheless, only two of these structures were characterized precisely as α -PbO and Pb₂O₃. Additional peaks were observed during the characterization of Pb/Co=3 (wt./wt.). These peaks may indicate mixed metal oxide pair since no matchup was hit in the databank. [44]

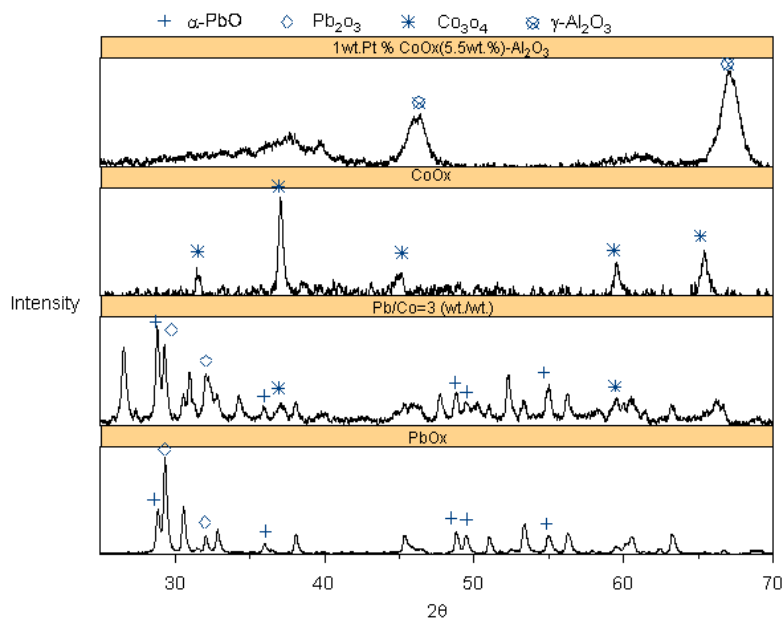


Figure 56: XRD characterization of PbOx, CoOx, Pb/Co=3 (wt./wt.) and 1wt.Pt% CoOx(5.5wt%)-Al₂O₃

4.2.4. Coal Oxidation Experiments

Oxygen release abilities of synthesized materials during thermal treatment were tested by conducting TPD analysis. Results were shown in Figure 57a. It was observed that lead oxide decomposition started after 600°C. Nevertheless, low decomposition rates were observed. Cobalt oxide decomposition started after 700°C. Oxygen evolution increased as temperature increases. A peak

temperature around 820°C was observed for CoOx decomposition. Mixed lead and cobalt oxide (Pb/Co=3 (wt./wt.)) shows two decomposition region: 350°C-450°C and after 670°C. Decomposition signal of this mixed metal oxide seems a mixed form of thermal decomposition plots of cobalt oxide and lead oxide materials. Different behavior was observed during thermal decomposition of 1wt.Pt% CoOx(5.5wt%)-Al₂O₃ material. When pure alumina was subjected to heat treatment, no oxygen evolution was observed above the detection limits of the instrument. Nevertheless, cobalt addition to pure alumina with Pt doping shows a broader absorbance increase between 400°C and 700°C. Obtained signals were further analyzed by using Simpsons' 1/3 rule. Area under each plot was estimated. Then, these values were divided by the oxygen available in the material. Calculated values were shown in Table 14.

Table 14: Thermal decomposition analysis of selected materials by TPD

Looping Material	Peak Temperature (°C)	Amount of Oxygen available, mg(A)	O ₂ peak area (a.u) (PA)	(PA)/(A)
PbOx	NA	5.19	5139	990
Pb/Co=3 (wt./wt.)	820	6.01	11163	1857
CoOx	820	13.28	4976	375
1wtPt% CoOx(5.5wt%)-Al ₂ O ₃	575	22.51	8544	657

Table 15: Gasification reaction results for performed looping material

Looping Material	Oxygen amount predicted, mg (a)	CO ₂ ,ml (b)	CO, ml (c)	c/a ($\times 10^{-3}$)
PbOx	20.76	0	0.001	0.05
Pb/Co=3 (wt/wt)	18.03	0	0.022	1.22
CoOx	39.84	0.04	0.070	1.75
1wtPt% CoOx(5.5wt%)-Al ₂ O ₃	67.53	0.08	0.155	2.29

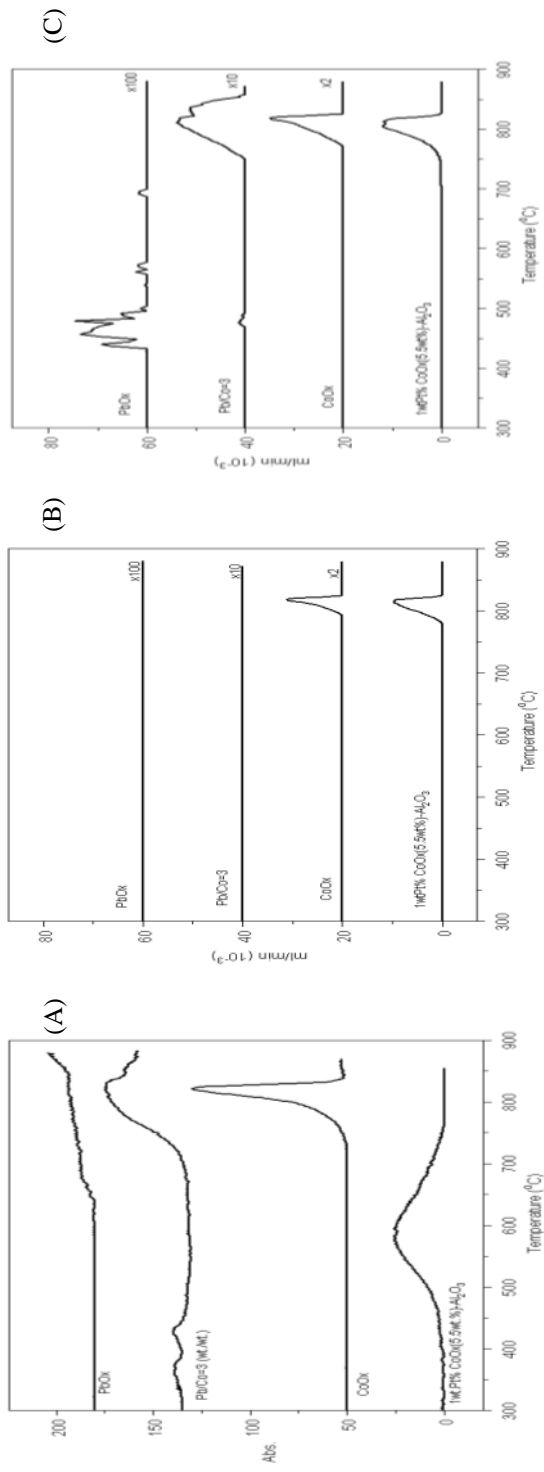


Figure 57: Results of thermal decomposition experiments (A); CO₂ formation during coal oxidation experiments (B); CO formation during coal oxidation experiments (C)

Extracted data in Table 14 were used for preliminary experiment of coal oxidation. Main objective was to show coal oxidation by thermally decomposing the specified metal oxides. Results were plotted in Figures 57b and 57c. It was found that only CO formed when PbOx and Pb/Co=3 (wt./wt.) were used. Nevertheless, formation rates were limited in both cases. Two CO favorable temperature zones were obtained for Pb/Co=3 (wt./wt.). First zone was observed due to Pb_2O_3 decomposition while second one seemed a mixture of Co_3O_4 and PbO. Both CO_2 and CO formation were observed for CoOx and 1wtPt% CoOx(5.5wt%)- Al_2O_3 materials. CO formation was found more favorable than CO_2 .

CHAPTER 5

DISCUSSIONS

As a result of the expected increase in world energy consumption by around 35% between 2010 and 2035, there is a need on alternative energy technologies. EIA 2010 statistics shows that US spent 22% of its total energy to transportation sector. Supplying such amount of oil is very difficult for net oil importer countries. In 2010, 49% of USA energy consumption was supplied from imports [45]. Therefore, interest on alternative energy technologies such as synthetic fuel production increases day by day. Solar and coal based alternative technologies are encouraged by government agencies throughout the world as well as in Turkey.

Coal based processes suffer from high ash and sulfur content feeds leading to slagging and SO_x emissions related problems in commercial gasification and combustion processes. Furthermore, coal based plants are under scrutiny for CO₂ emissions which are also solved by sequestration technologies. For easy sequestration, N₂ free stack gases are needed for which, oxy-fuel combustion technologies are used. On the other hand, solar energy is the most abundant energy source all over the world. Nevertheless, technology is in its infancy for the storage and transport of solar energy. Solar thermochemical processes offer an alternative, but their viability should be tested.

For both N₂ free coal combustion or gasification and solar thermochemical processes, reducible oxides used as chemical looping agents offer a very promising alternative [51, 52]. For example, pilot scale studies were compiled in Table 3 earlier in this thesis for chemical looping combustion technologies. Solar fuel field is still in its infancy, thus only proof of principle studies are available in the literature [51]. Both of these fields would benefit immensely from a systematic methodology for the selection of materials based on the design principles, in contrast to an empirical approach. In the scope of this thesis, a thermodynamic analysis was conducted to select metal oxides as chemical looping agents.

For this purpose, Ellingham diagrams for cobalt, lead, iron, cerium and zinc were constructed. Their relative positions were compared with carbon and hydrogen related reactions. It was found that formation Gibbs free energies of ceria, ferrous oxide and zinc monoxide are less than formation Gibbs free energies of CO₂, CO and H₂O. Therefore, syngas can be produced via cerium, iron and zinc since their oxide forms are more stable. Nevertheless, regeneration of these materials needs high temperature due to high metal oxide stability. Cerium, iron and zinc are mostly studied for solar syngas production. Schnuk *et al.* shows that dissociation temperature for ZnO is around 1700°C [46] whereas same temperature is 1500°C for SnO₂ [47]; 2000°C for CeO₂ [48, 49] and 1200°C for Fe₃O₄ [50]. It was also found that cobalt and lead can reduce CO₂ and H₂O and produce syngas at lower temperatures when compared to ceria, zinc oxide and magnetite. Nevertheless, less reduction strength is expected when compared to cerium, zinc, and iron.

Syngas can be produced from fossil fuels such as coal and biomass. Commercial molten iron bath gasifiers generally use magnetite as bath materials since reduction of magnetite is more favorable than ferrous oxide. Therefore, magnetite reduction to ferrous oxide is the desired reaction for supplying oxygen. Since Pb and its oxides have much lower melting points than magnetite, they offer a very

promising alternative for this type of gasifiers. As result, a similar analysis was conducted for Pb_3O_4 and Co_3O_4 materials. It was found that carbon oxidation is more favorable at low temperatures when lead and cobalt oxides are available. Metal oxide stability under various conditions was also studied. Lead oxide has more oxide forms than cobalt oxide and iron oxide. Transformation between these forms occurs at low temperatures which makes it suitable for carbon oxidation at low temperatures hence improving energy efficiency of these processes.

Bath material in a commercial molten metal bath gasifier should be selected such a way that it should absorb excess carbon in order not to lose unconverted carbon in slag. Therefore, stability analysis was conducted at CO/CO_2 atmosphere. When gasification processes are the main interest, lead can offer more place for carbon storage by forming carbonates while cobalt oxide can supply more oxygen to the system. Therefore, use of Co-Pb in same reaction environment can affect system performance by both supplying oxygen and carbon storage places.

Turkish lignite has considerable sulfur content. This sulfur content reacts with available hydrogen and oxygen and forms H_2S and SO_x . These gases lower the product gas quality and influence the downstream process by poisoning the valuable catalysts. Nevertheless, sulfur has also a positive effect on the reactivity as indicated in Chapter 2.4. Therefore, absorption of sulfur in the reaction environment is important to increase the reactivity. Thermodynamic analysis of sulfur removal from product gas was performed for iron, cobalt and lead materials. It was found that lead and lead oxides are more suitable for low temperature sulfur removal processes when their thermodynamic characteristics are compared with cobalt and iron.

Thermodynamic limitations directly affect the boundaries of system efficiency. Nevertheless, if oxygen source is changed from molecular oxygen to metal oxide, product distribution could be changed at same temperature and pressure. Therefore, effect of cobalt oxide, lead oxide and iron oxides to equilibrium was investigated during carbon oxidation. Most commercial process uses iron and its oxides for carbon oxidation. Results show that carbon oxidation is only possible when temperatures are high enough. Nevertheless, it was found that carbon oxidation via lead oxide seems more desirable. Product distribution seems similar with the findings of C-S-O system. Cobalt oxide reacts with carbon after 500K to form CO_2 . Then, CO formation becomes favorable as temperature increases. When reaction with sulfur is concerned, it was found that elemental sulfur is very reactive with studied metals at low temperatures. Metal sulfides are formed at low oxygen atmospheres and low temperature. SO_x forms as the oxygen content in reaction environment increases. Therefore, oxygen and temperature control is crucial for desired product distribution at equilibrium.

Verification of theoretical findings was performed by setting up several experimental methods. First experiments were conducted by performing visual observation. Lead was oxidized up to $700^\circ C$. Different oxide forms were observed. After $800^\circ C$, formed lead oxide became so unstable that it directly decomposed to more stable forms. Therefore, it was found that lead oxidation via air was favorable up to $700^\circ C$ whereas thermal decomposition was achieved after $800^\circ C$. H_2 was also produced from H_2O by using lead rods in a home built setup. CO_2 reduction experiment was also performed. CO evolution was observed by FT-IR as temperature increases. This formation was also verified by Mass Spectrometry (Appendix F). A thermal decomposition experiment was performed after the experiment. Oxygen evaluation peaks were observed at certain temperatures. Obtained temperatures were very close to the know decomposition temperatures of PbO_2 , Pb_2O_3 and PbO . To sum up, CO_2 and H_2O reduction by lead was also verified experimentally. Then, lead oxide was decomposed thermally. This two main findings shows that lead can be used as a chemical looping agent for carbon and oxygen neutral cycles. Released oxygen during thermal decomposition can be taken as oxygen or it can be used for oxidation of carbon sources.

Lead oxide and cobalt oxide were decomposed thermally as temperature increases. Oxygen evaluation rates of each material were determined by TPD analysis. Detailed analysis was shown in Appendix G. It was found that amount of oxygen released per gr oxygen available in the material becomes higher when cobalt and lead oxide were mixed with certain proportions. Highest value was obtained when $Pb/Co=3(wt./wt.)$. A broader oxygen evaluation was observed for $1wt.Pt\% CoO_x(5.5wt.\%)-Al_2O_3$.

These two materials with lead oxide and cobalt oxide were further tested for coal oxidation. Proof of principle experiments were conducted for coal oxidation via thermal decomposition of these metal oxides. Similar findings with thermal decomposition were found except 1wt.Pt% CoOx(5.5wt.%)-Al₂O₃. CO and CO₂ formation rates of 1wt.Pt% CoOx(5.5wt.%)-Al₂O₃ were close to cobalt oxide's rates. Nevertheless, total amount of formed CO₂ and CO were doubled. This statement is verified by Table 14. It was concluded that coal can oxidize to CO and CO₂ depending on the oxygen evaluation rates. Almost no CO formation was observed when lead oxide and Pb/Co=3(wt./wt.) material were used due to low decomposition rates. CO₂ and CO evolution was observed when cobalt oxide and 1wt.Pt% CoOx(5.5wt.%)-Al₂O₃ were used.

Under the findings of thermodynamic and experimental analysis, a process scheme was suggested for syngas production via reducible metal oxides as shown in Figure 58. Looping material oxidation by air, CO₂ and H₂O was shown in Part 1. After oxidation, user can operate this process in two different ways. Pure oxygen can be obtained by thermal decomposition of looping material under vacuum as seen in Part 2a. In addition, carbon source such as methane can also be oxidized by looping material for syngas production (Part 2b). Combination of Part 1 and Part 2a was also studied by Steinfeld *et al.* [51]. Nevertheless, their operating temperatures are very high due to high decomposition temperature of ceria. Findings of this thesis offer that cobalt oxide and lead oxide can be used as a chemical looping agent instead of ceria or magnetite due to its CO₂, H₂O reduction ability and its oxide stability.

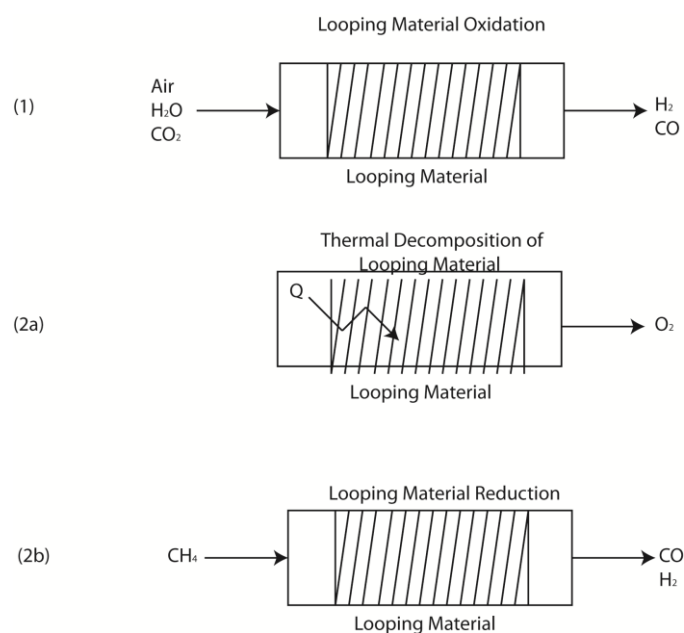


Figure 58: Suggested scheme for syngas production via cobalt and lead oxide.

CHAPTER 6

SUMMARY AND CONCLUSIONS

In the scope of this thesis, syngas production over reducible oxides was studied both theoretically and experimentally. Theoretical calculations were done on equilibrium basis by constructing Ellingham diagrams, predominance diagrams and by performing Gibbs free energy minimization analysis. Equilibrium compositions of certain systems were calculated at 400K to 1300K and at 0.1 to 10bars. It was concluded that cobalt oxide, lead oxide and their mixed forms could be used for carbon oxidation. It was also seen that sulfur reacts with metal to form metal sulfides during oxidation of high sulfur containing carbon sources. After theoretical calculations, experimental verification was investigated in various experimental setups and methods.

Experimental results showed that a synergetic effect between cobalt and lead oxide can be achieved with a mixing ratio Pb/Co=3 (wt./wt.). XRD characterization verifies this statement since new peaks were observed. Synthesized material performances were examined for thermal decomposition and coal oxidation experiments. It was observed that Pb/Co=3 (wt./wt.) material oxidizes the carbon of coal with almost no CO₂ formation due to slow decomposition kinetics. CO produced per mg oxygen content available is quite comparable with pure cobalt oxide and 1wtPt% CoO_x(5.5wt.%)-Al₂O₃. Nevertheless, high CO₂ production was observed. This fact supports the idea of that these materials can be used as oxygen carriers for fossil based fuels oxidation. Re-oxidation of reduced metals was also performed by using CO₂ and H₂O as oxidizing agents. To sum up, a thermodynamic route was presented for syngas production via reducible metal oxides. Cobalt and lead oxides were mainly studied. It was found that cobalt-lead mixed metal oxide material with mixing ratio Pb/Co=3 (wt./wt.) is suitable for chemical looping material for syngas production.

REFERENCES

- [1] Japan International Cooperation Agency (JICA), *The Final Report for the Feasibility Study on Effective Utilization of Banko Coal in Republic of Indonesia, Volume I (1989)*
- [2] Bergius, F. (1913) U.S. Patent No. 1,059,818. Washington, DC: U.S.
- [3] *Fischer-Tropsch archive*. (01, 2013 16). Retrieved from <http://www.fischer-tropsch.org/>
- [4] Fan, L., Zeng, L., Wang, W., & Luo, S. (2012). Energy & environmental science. *Chemical looping processes for CO₂ capture and carbonaceous fuel conversion- prospect and opportunity*, 5, 7254.
- [5] Linderholm, C., Cuadrat, A., & Lyngfelt, A. (2011). Chemical-looping combustion of solid fuels in a 10 kwth pilot – batch tests with five fuels. *Energy Procedia*, 4, 385-392.
- [6] Uner, D., Demirkol, M., & Dernaika, B. (2005). A novel catalyst for diesel soot oxidation. *Applied Catalysis B: Environmental*, 61, 334-345.
- [7] Juntgen, H. (1983). Application of catalysts to coal gasification processes: incentives and perspectives. *Fuel*, 62(2), 234-238.
- [8] Otto, K., Bartosiewicz, L., & Shelef, M. (1979). Catalysis of carbon-steam gasification by ash components from two lignites. *Fuel*, 58(2), 85-91.
- [9] Douchanov, D., & Angelova, G. (1983). Effect of catalysis and inlet gas on coal gasification. *Fuel*, 62(2), 231-233.
- [10] McKee, D., Spiro, C., Kosky, P., & Lamby, E. (1983). Catalysis of coal char gasification by alkali metal salts. *Fuel*, 62(2), 217-220.
- [11] Darwent, B. D. U.S. Department of Commerce, National Bureau of Standards. (1970). *Bond dissociation energies in simple molecules (NSRDS-NBS 31)*. Washington D.C.: U.S. Government Printing Office
- [12] Mazzocco, N. J.; Klunder, E.B.; Krastman, D. Pittsburg Eng. Tech. Center, Pittsburg, PA, Report No. DOE/PETC/TR-81/1, March 1981
- [13] Moroni, E. C. Paper 6a presented at Spring AIChE Meeting, Houston, TX, 1981
- [14] Anderson, R. R. and Bockrath, B.C. *Fuel* 1984, **63**, 329
- [15] Lambert, J. M. *Fuel* 1982, **61**, 777
- [16] Bommannavar, A. S. and Montano, P. A. *Fuel* 1982, **61**, 523
- [17] Montano, P. A., Bommannavar, A. S. and Shah, V. *Fuel* 1981. **60**, 703.
- [18] Anderson, R. R., Bockrath, B.C. *Fuel* 1984, 63, 329.
- [19] Iron Sulfide Catalysis in Coal Liquefaction P. A. Montano, Y. C. Lee, A. Yeye-Odu, and C. H. Chien *Mineral Matter and Ash in Coal*. **April 2, 1986**, 416-429
- [20] Gozmen, B., Arkok, L., Erbatur, G., Erbatur, O. *Energy&Fuels* 2002, **16**, 1040.
- [21] Juntgen, H., Application of catalysts to coal gasification processes, incentives and perspectives, *Fuel*, 62: 234-238, 1983
- [22] Nishiyama, Y., *Fuel Process. Technol.*, 29: 31-42, 1991
- [23] McKee, D., & Chatterji, D. (1975). The catalytic behavior of alkali metal carbonates and oxides in graphite oxidation reactions. *Carbon*, 13(5), 1975.
- [24] Catalytic coal gasification reports. In (1976-1982). Exxon Research and Engineering Co.
- [25] Hahn, R., Heering, J., & Huttinger, K. (1977). Iron catalyzed steam gasification of coke. *ChemieIngenieurTechnik*, 49(12), 973-973.
- [26] Messerschmitt, A. (1910) U.S. Patent No. 971,206. Washington, DC: U.S.
- [27] Lane, H. (1913) U.S. Patent No. 1,078,686. Washington, DC: U.S.
- [28] Gilliard, ER and Lewis WK. (1950) U.S. Patent No. 2,498,088. Washington, DC: U.S.
- [29] Biljetina, R. and Tarman, PB. Alternative energy sources II; Proceedings of the Second Miami International Conference, Miami Beach, Fla., December 10-13, 1979. Volume 8. (A81-25137 09-44) Washington, D.C., Hemisphere Publishing Corp., 1981, p. 3335-3347

- [30] Dobbyn, R.C. et al. 1978 "Evaluation of the Performance of Materials and Components Used in the CO₂ Acceptor Process Gasification Pilot Plant," Technical Report, U.S. Department of Energy, DOE-ET-10253-T1, Washington, D.C.
- [31] Miyamoto, A. et al. (1984) *Ind. Eng. Chem. Prod. Res. Dev.*, 23, 467-470.
- [32] Kodama, T. et al. (2000) *Energy*, 25, 411-425
- [33] Ryden, M., Lynggelt, A. (2006) *Int. J. Hydrogen Energy*, 31, 1271-1283
- [34] T.B. Massalski, (Ed.), *Binary Alloy Phase Diagrams*, 2nd edition, ASM International, Metals Park, Ohio (1990)
- [35] JU.V. LEWINSKY, "The Phase Diagrams of Metals with Gas" (in Russian), *Izd. Metallurgija*, Moscow (1975)
- [36] FactSage. (01, 2013 11). *Database documentation*. Retrieved from <http://www.crct.polymtl.ca/fact/documentation/>
- [37] Blanks, R.F., and Willis, G.M., 1961, Equilibria between lead, lead sulfide and cuprous sulfide and the deooperizing of lead with sulfur, in *Metallurgical Society Conferences*, v. 8, Physical chemistry of process metallurgy, pt. 2: New York, Intersci. Publishers, p.91-1028.
- [38] Garner WE (1955) *Chemistry of the solid state*. Butterworths, London
- [39] Galwey AK, Dollimore D, Brown ME (1980) *Reactions in the solid state*. Elsevier, Amsterdam
- [40] L'vov BV, Ugolkov VL, Grekov FF (2004) *ThermochimActa* 411:187–193
- [41] L'vov, B. (2007). *Thermal Decomposition of Solids and Melts*. Chp 2. (p. 13). Springer. Retrieved from <http://www.springer.com/materials/book/978-1-4020-5671-0> (2/11/13)
- [42] Barin, I. (1995). *Thermochemical data of pure substances*.
- [43] Sons, J., Powell, Russell, Powell, James, Company, R.R., Army, Rose. (1985). *Phase equilibria in chemical engineering*. Oryx Pr.
- [44] "Selected Powder Diffraction Data for Education and Training, Search Manual and Data Cards", International Center for Diffraction Data, Pennsylvania, 1988.
- [45] US Department of Energy, US Energy Information Administration. (2012). *Annual energy outlook*. Retrieved from website: [http://www.eia.gov/forecasts/aeo/pdf/0383\(2012\).pdf](http://www.eia.gov/forecasts/aeo/pdf/0383(2012).pdf)
- [46] Schunk, LO., et al. (2008) *J. Solar Energy Eng*, 130, 021009-1.
- [47] Abanades, S. et al. (2008) *Int. J. Hydrogen Energy*, 33, 6021.
- [48] Charvin, P. et al. (2009) *Solid State Ionics*, 180, 1003
- [49] Chueh, WC. (2009) Haile, SM. *ChemSusChem*, 2, 735
- [50] Roeb, M. et al. (2009) *Int. J. Hydrogen Energy*, 34, 4537
- [51] Chueh, W., Falter, C., Abbott, M., Scipio, D., Furler, P., Haile, S., & Steinfeld, A. (2010). High-flux solar-driven thermochemical dissociation of co₂ and h₂o using nonstoichiometric ceria. *Science*, 330(6012), 1797-1801.
- [52] Ryden, M., Johansson, M., Lyngfelt, A., & Mattisson, T. (2009). NiO supported on mg-zro₂ as oxygen carrier for chemical-looping combustion and chemical-looping reforming. *Energy & Environmental Science*, 970-981.

APPENDIX A

CONSTRUCTION OF PHASE STABILITY DIAGRAMS

Construction of phase stability will be described by an example. First step in construction of lead oxide stability diagrams is to determine possible chemical compounds; Pb, PbO, Pb₃O₄, Pb₁₂O₁₇, Pb₂O₃, Pb₁₂O₁₉, and PbO₂. Thereafter, all possible reactions describes the transformations between these metal oxides are determined.





Reaction constants are calculated for specified temperature and pressure. Then, equilibrium pressures for oxygen are found as a function of temperature. Now, enough data is collected so construction part can be started.

First step is to construct the lines of first 6 reactions as Figure A.1. These 6 reactions are related with metallic lead oxidation. It should be noted that only one reaction is possible which satisfies the lowest Gibbs free energy. Therefore, Reactions 2 to 6 should be eliminated as shown in Figure A.2.

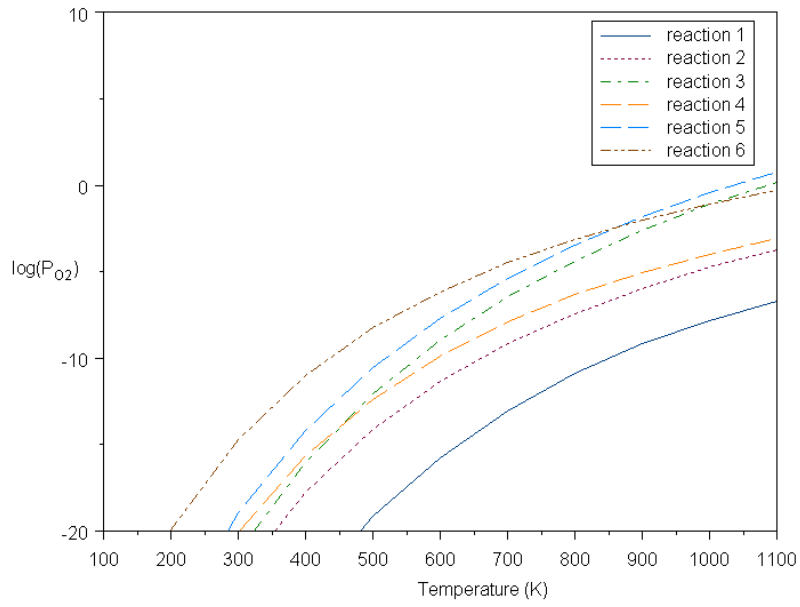


Figure A 1: Equilibrium partial pressures of oxygen for Reactions 1 to 6.

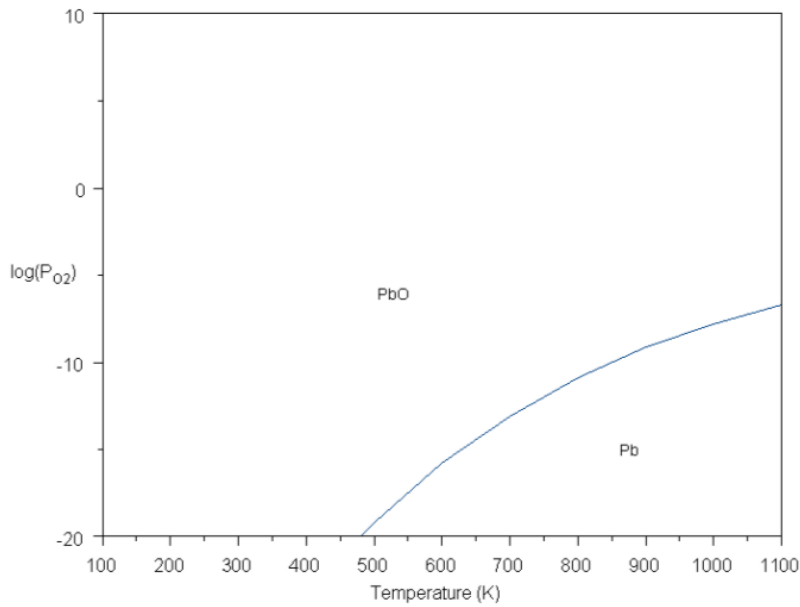


Figure A 2: Pb/PbO stability diagram.

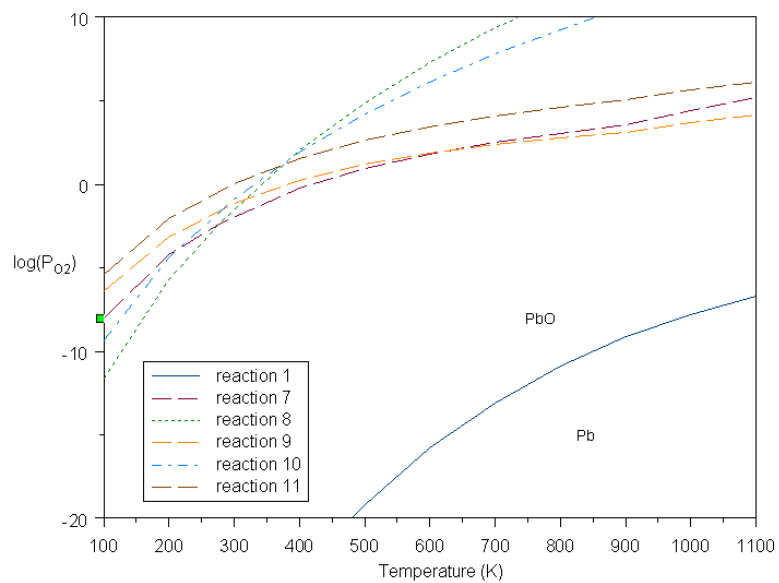


Figure A 3: Equilibrium partial pressures of oxygen for Reactions 1 and 7 to 11.

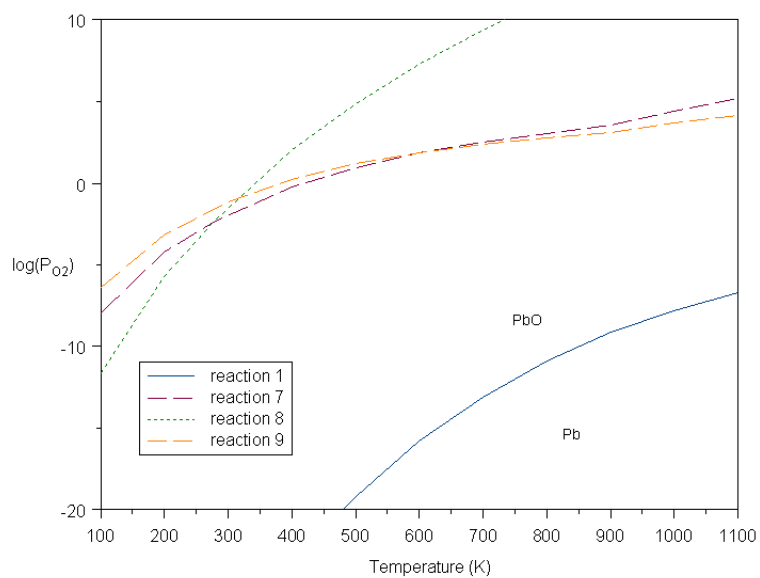


Figure A 4: Stability patterns of Reactions 1, 7 to 9.

Second step is related with lead monoxide oxidation. Reactions 7 to 11 are studied. Then, these lines are inserted to Figure A.2 and Figure A.3 is formed. Out of these 5 reactions only three of them possible in studied temperature range. Therefore, Reaction 10 and 11 are eliminated since equilibrium oxygen partial pressure lines of Reaction 7 to 9 are lower than these ones as shown in Figure A.4. Then, these lines are cut from their intersections and Figure A.5 is formed.

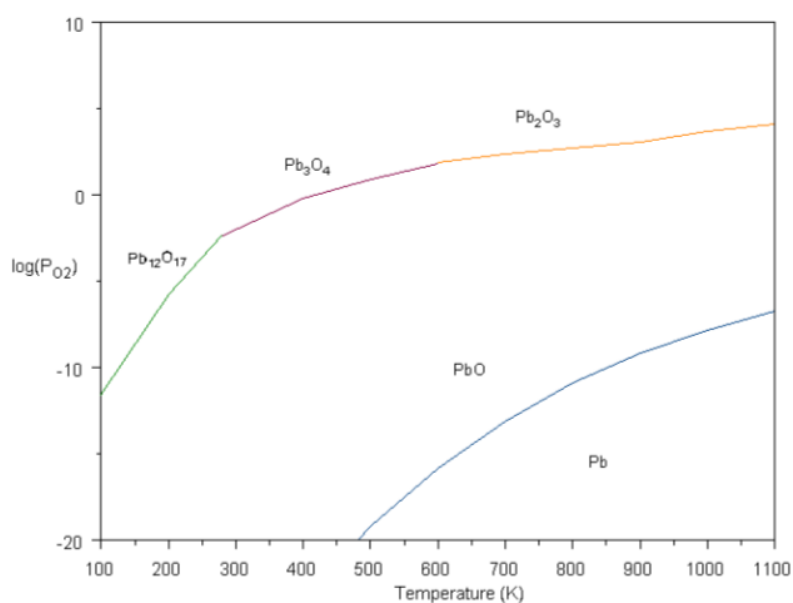


Figure A 5: Pb/PbO/Pb₃O₄/Pb₁₂O₁₇/Pb₂O₃ stability diagram.

Third step is the integration of Reactions 12 to 15 into Figure A.5. Reactions 14 and 15 are eliminated since nearest lines to Pb₃O₄ are found as Reactions 12 and 13 as in Figure A.6. Remaining possible reaction lines are shown in Figure A.7. Final form is shown in Figure A.8 after cutting extra parts of the Reaction 12 and 13.

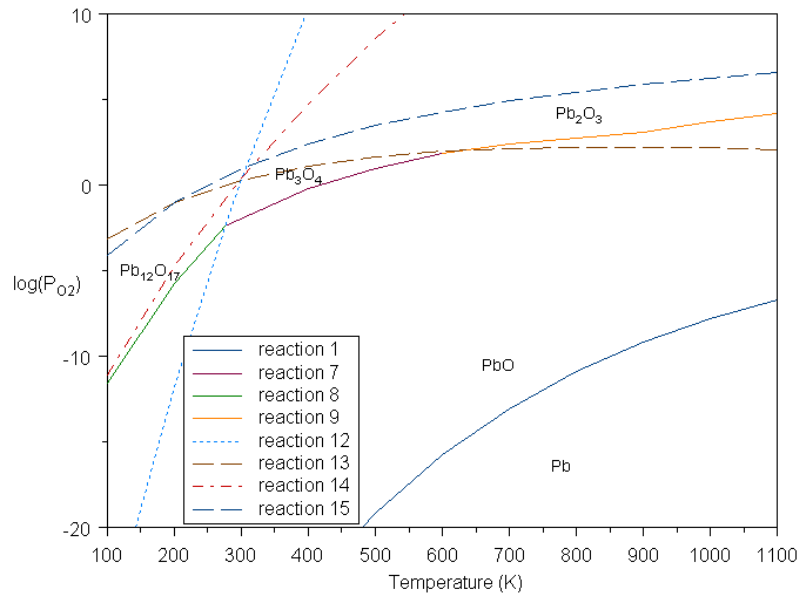


Figure A 6: Stability patterns of Reactions 1, 7 to 9 and 12 to 15.

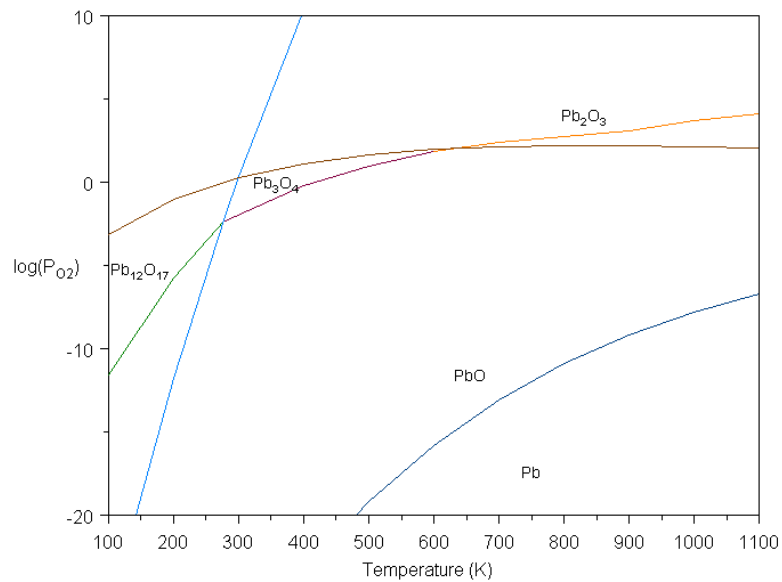


Figure A 7: Pb/PbO/ Pb_3O_4 stable region (raw figure)

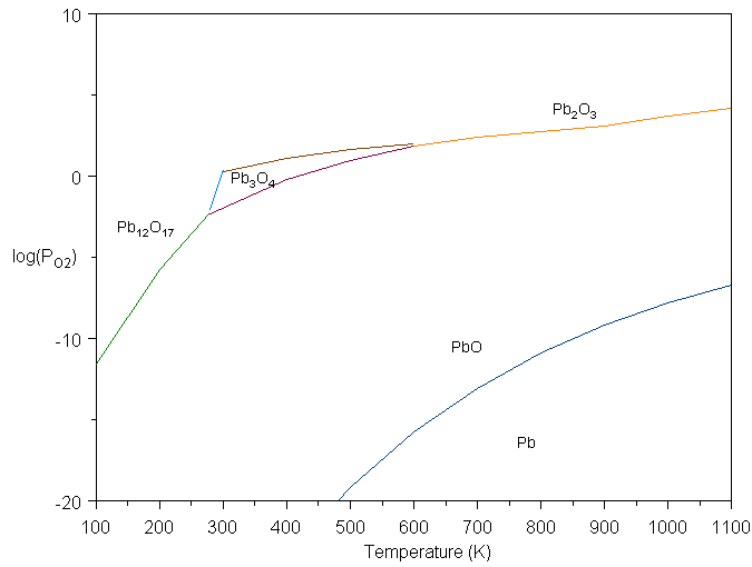


Figure A 8: Pb/PbO/Pb₃O₄ stable region after trimming extra lines

Next step is about Reactions 16 to 18. Reactions 16 and 18 are not possible to occur as shown in Figure A.9. Figure A.10 is constructed after trimming necessary part of the Reaction 17.

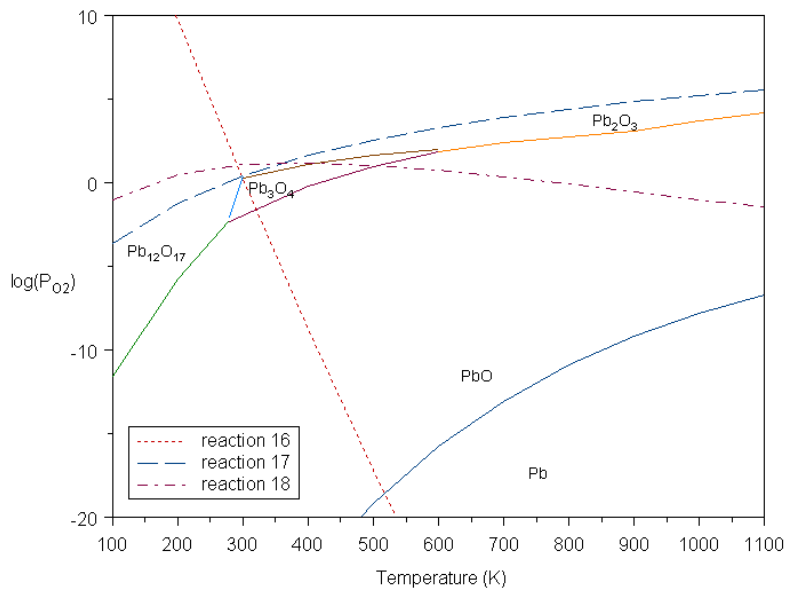


Figure A 9: Stability patterns of Reactions 16 to 18

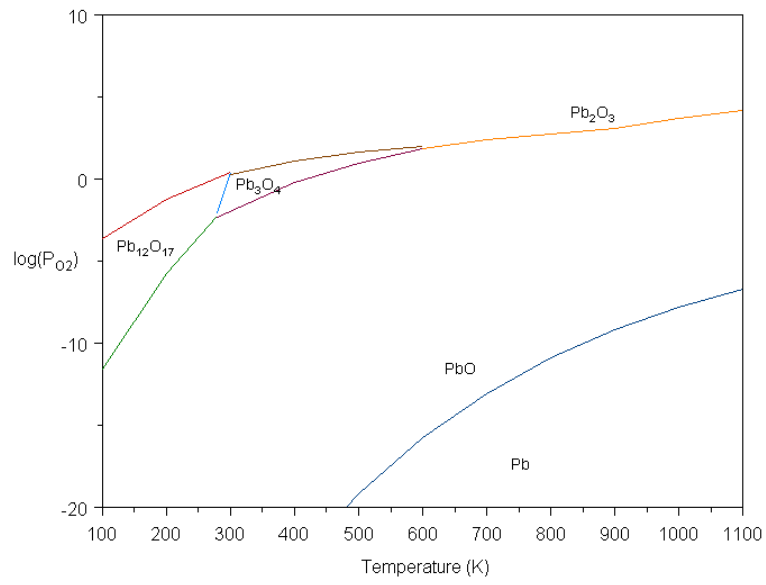


Figure A 10: Pb/PbO/ Pb_3O_4 / $Pb_{12}O_{17}$ / Pb_2O_3 stability diagram

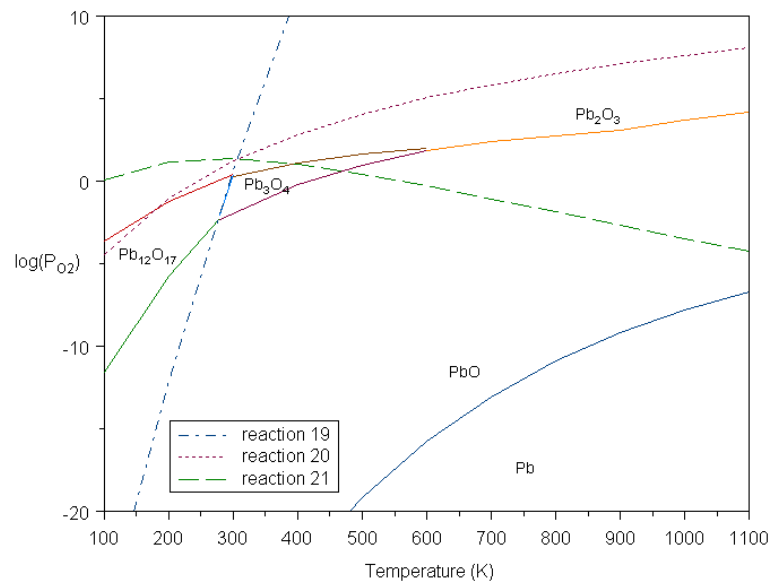


Figure A 11: Stability patterns of Reactions 19 to 21.

Analysis of Reactions 19 to 21 is studied in Figure A.11. It is shown that these three reactions are possible reactions. Then, they are trimmed from intersection points. Finally, the oxygen stability diagram of lead is formed as in Figure A.12.

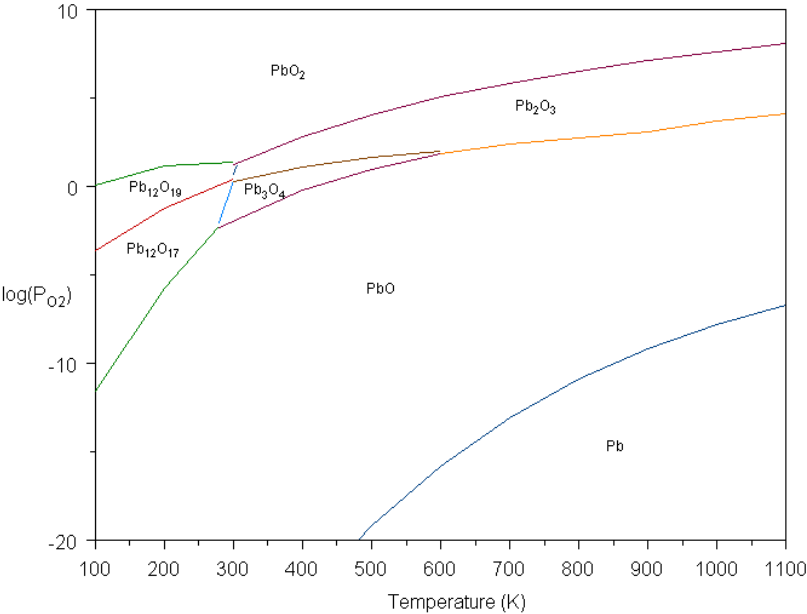


Figure A 12: Stability diagram of lead/lead oxide compounds

APPENDIX B

MATLAB CODE FOR GIBBS FREEE ENERGY MINIMIZATION

A sample code is given used for C-S-O-Pb system at 1300K at 0.1 bars

```
%% MAIN PROGRAM %%
clc;
clear all;

Aeq = [ 0  0  0  0  0  0  1  1  1  1  % Pb balance
        1  1  0  0  0  1  0  0  0  0  % C balance
        1  2  2  2  0  0  0  1  0  4  % O balance
        0  0  0  1  1  0  0  0  1  1]; % S balance

% equimolar feed of 1 mol H2O and 1 mol CO
beq = [0  % mol Pb fed
       1  % mol C fed
       0.5  % mol O fed
       0.05]; % mol S fed

LB = [0 0 0 0 0 0 0 0 0 0]; %lower limit has to be zero

x0 = [0.5 0.5 0.5 0.5 0.5 0.5 0.5 0.5 0.5 0.5]; % initial guesses

species = {'CO','CO2','O2','SO2','S','C','Pb','PbO','PbS','PbSO4'};
a=species';

options = optimset('Algorithm','sqp','TolX',1e-4);
x = fmincon(@func,x0,[],[],Aeq,beq,LB,[],[],options)

for i=1:numel(x)
fprintf('%5d%10s%15.4f mole\n',i, species{i}, x(i))
end
```

```

%% SUB PROGRAM %%

function G = func(nj)
load('gibbs.mat');
T = 1300; %K
i= 10; % 10 points gibbs free energy of species j at T=1300 (T=400
at i=1)

R = 8.314; % kJ/mol/K

P = 0.1; % atm, this is the total pressure in the reactor
Po = 1; % atm, this is the standard state pressure
species = {'CO' 'CO2' 'O2' 'SO2' 'S' 'C' 'Pb' 'PbO' 'PbS' 'PbSO4'};

% Gibbs energy

Enj = sum(nj(1,1)+nj(1,2)+nj(1,3)+nj(1,4));
G = nj(1,1)*(Gj(i,1)/R/T + log(nj(1,1)/Enj*P/Po))...
+nj(1,2)*(Gj(i,2)/R/T + log(nj(1,2)/Enj*P/Po))...
+nj(1,3)*(Gj(i,3)/R/T + log(nj(1,3)/Enj*P/Po))...
+nj(1,4)*(Gj(i,4)/R/T + log(nj(1,4)/Enj*P/Po))...
+nj(1,5)*Gj(i,5)/R/T...
+nj(1,6)*Gj(i,6)/R/T...
+nj(1,7)*Gj(i,7)/R/T...
+nj(1,8)*Gj(i,8)/R/T...
+nj(1,9)*Gj(i,9)/R/T...
+nj(1,10)*Gj(i,10)/R/T;

end

%% gibbs.mat file %%
%% this file demonstrates the Gibbs free energies of compounds %%
%% rows show temperatures from 400 to 1300 with 100K increments %%
%% columns show compounds in the order of species given in the code
%%
-190064 -479618 -82523 -396743 -13277 -2449 -26340 -246275 -135951 -984181
-211030 -502638 -104262 -423297 -18181 -3473 -33944 -255101 -147141 -1003423
-232596 -526554 -126626 -450787 -23867 -4789 -42122 -264941 -159365 -1025031
-254671 -551260 -149528 -479099 -30124 -6386 -51588 -275653 -172466 -1048785
-277193 -576676 -172901 -508140 -36856 -8248 -61494 -287133 -186332 -1074546
-300114 -602735 -196697 -537838 0 -10358 -71776 -299301 -200879 -1102212
-323398 -629384 -220875 -568131 0 -12700 -82389 -312098 -216040 -1131708
-347014 -656577 -245402 -598970 0 -15257 -93297 -325473 -231764 -1162979
-370937 -684274 -270251 -630309 0 -18016 -104469 -340292 -248008 -1196881
-395145 -712441 -295397 -662114 0 -20965 -115882 -356944 -264736 -1232982

```

APPENDIX C

GIBBS FREE ENERGY MINIMIZATION RESULTS

1. C-O-S SYSTEM

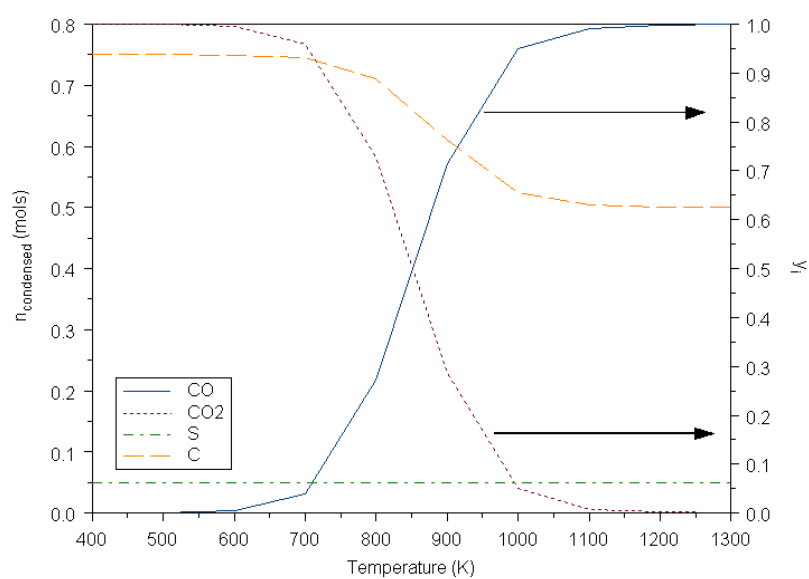


Figure C 1: Equilibrium composition of a system of C=1mol; S=0.05mol; O=0.5mol at 0.1bar

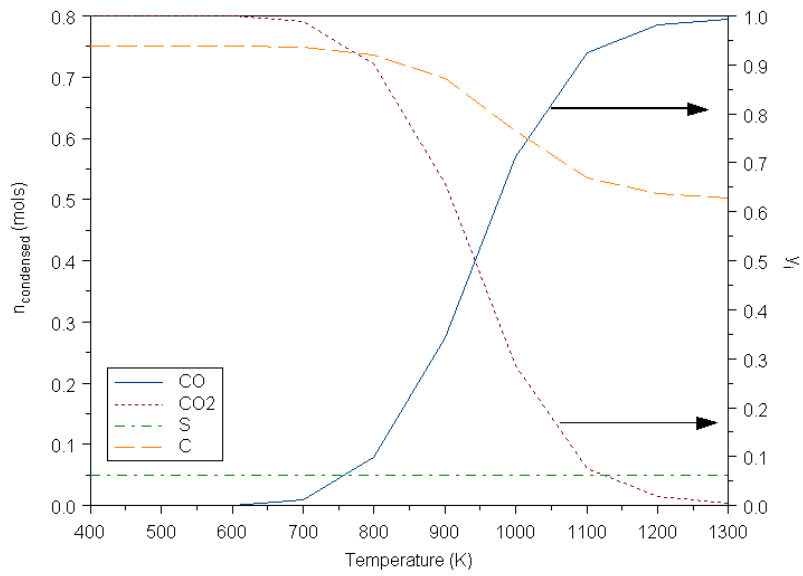


Figure C 2: Equilibrium composition of a system of C=1mol; S=0.05mol; O=0.5mol at 1bar

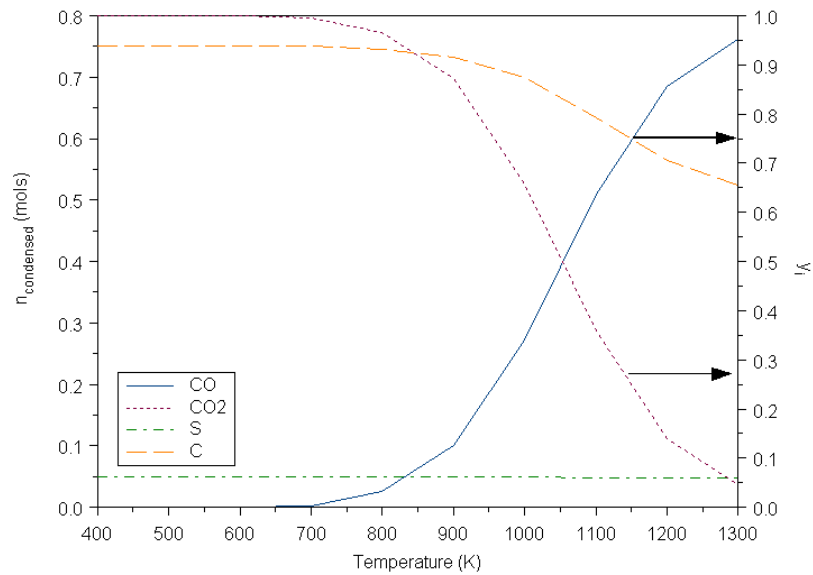


Figure C 3: Equilibrium composition of a system of C=1mol; S=0.05mol; O=0.5mol at 10bar

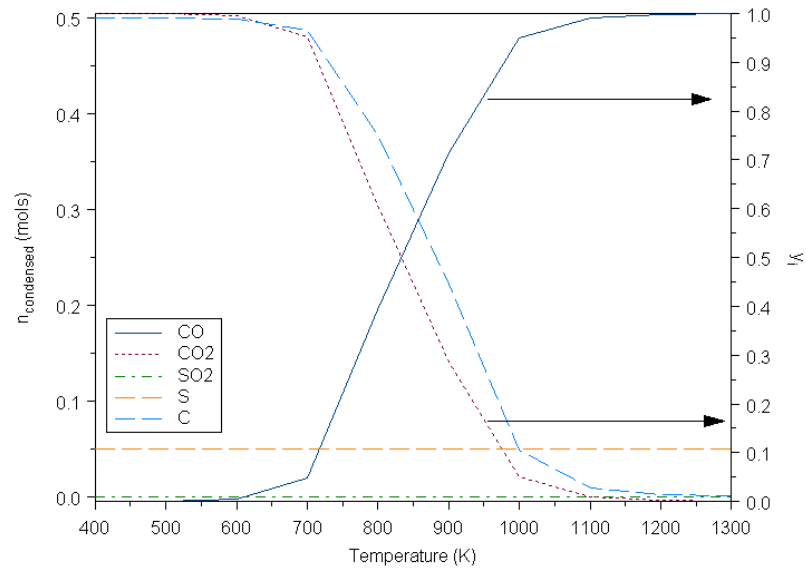


Figure C 4: Equilibrium composition of a system of C=1mol; S=0.05mol; O=1mol at 0.1bar

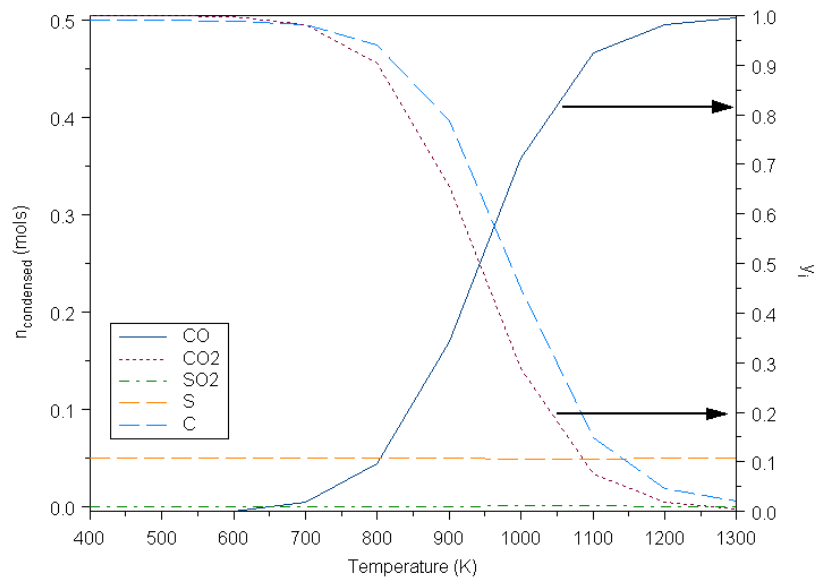


Figure C 5: Equilibrium composition of a system of C=1mol; S=0.05mol; O=1mol at 1bar

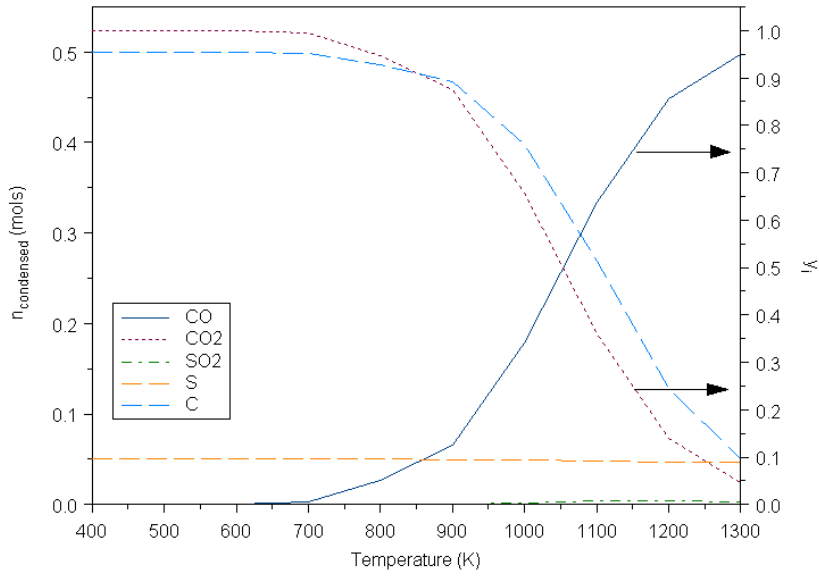


Figure C 6: Equilibrium composition of a system of C=1mol; S=0.05mol; O=1 mol at 10bar

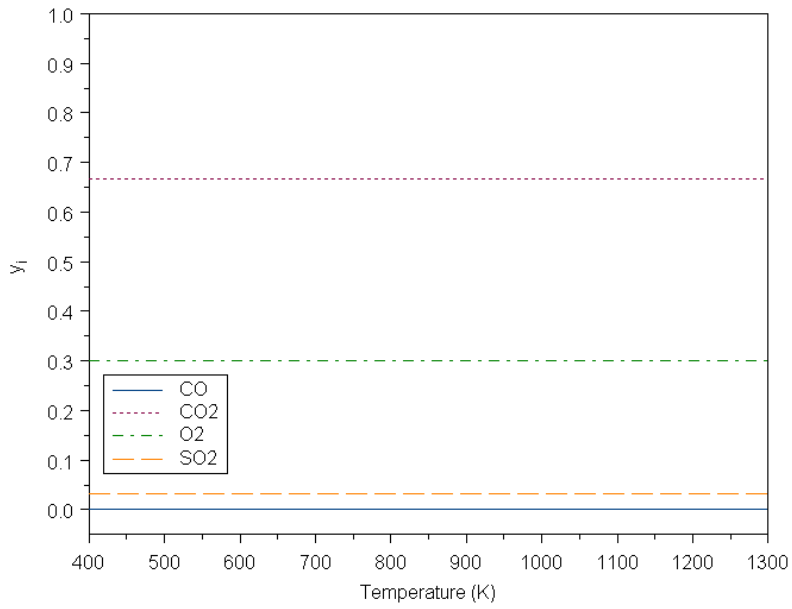


Figure C 7: Equilibrium composition of a system of C=1mol; S=0.05mol; O=3mol at 0.1bar, 1 bar and 10bar

2. C-S-O-Pb SYSTEM

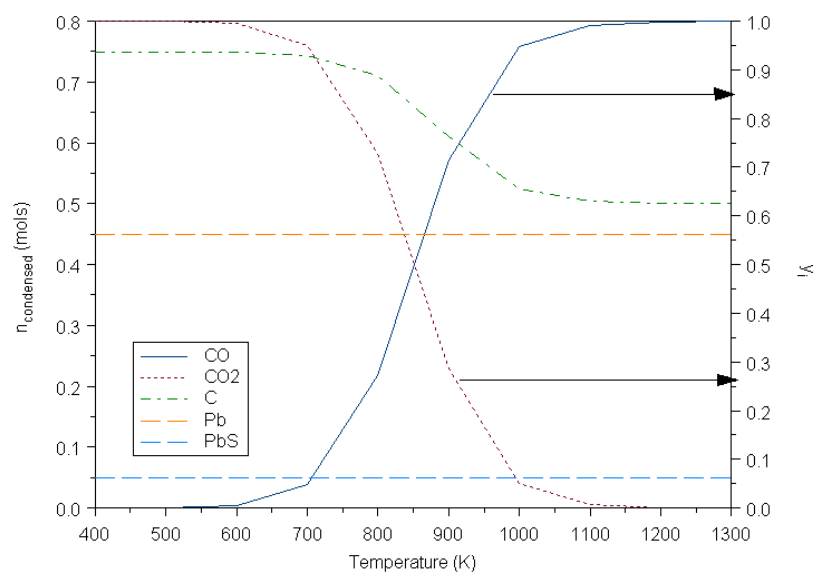


Figure C 8: Equilibrium composition of a system of C=1mol; S=0.05mol; O=0.5mol; Pb=0.5mol at 0.1bar

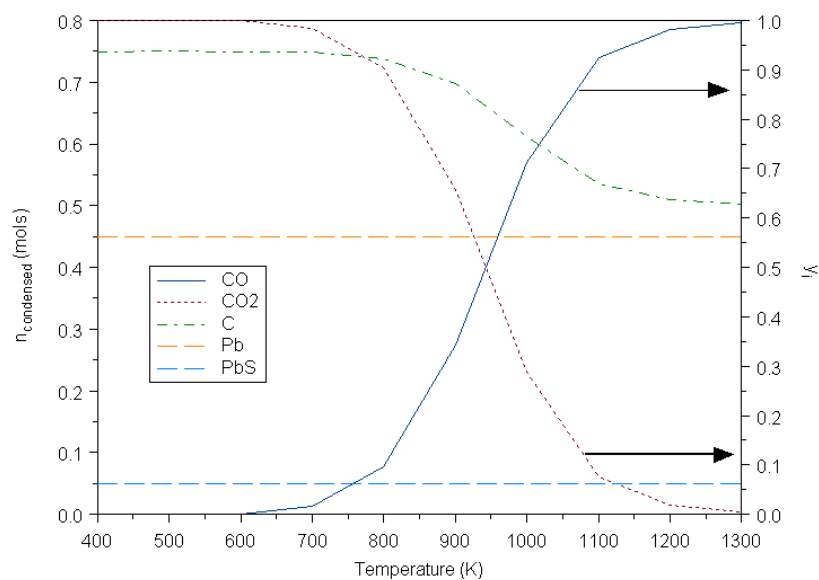


Figure C 9: Equilibrium composition of a system of C=1mol; S=0.05mol; O=0.5mol; Pb=0.5mol at 1bar

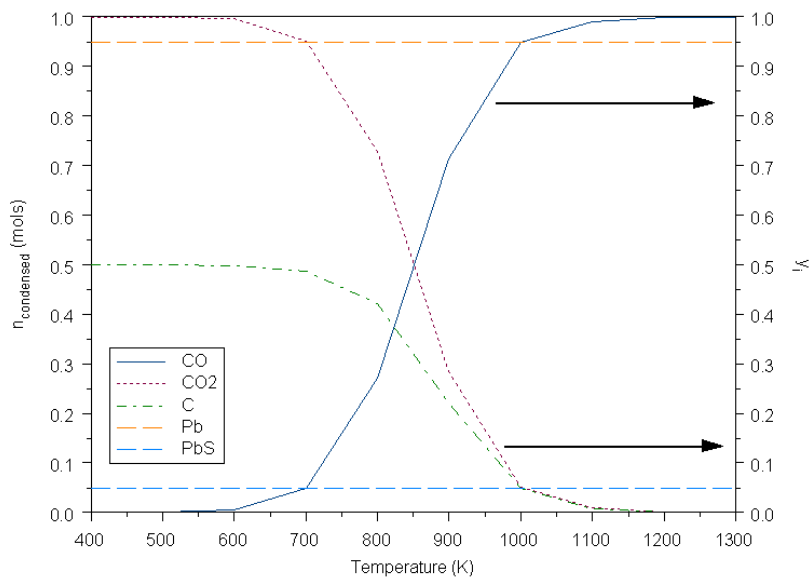


Figure C 10: Equilibrium composition of a system of C=1mol; S=0.05mol; O=1mol; Pb=1mol at 0.1bar

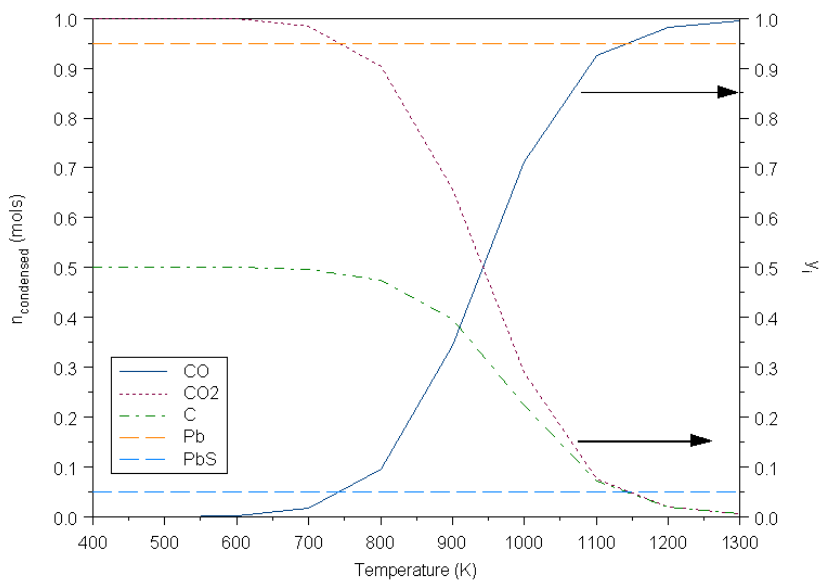


Figure C 11: Equilibrium composition of a system of C=1mol; S=0.05mol; O=1mol; Pb=1mol at 1bar

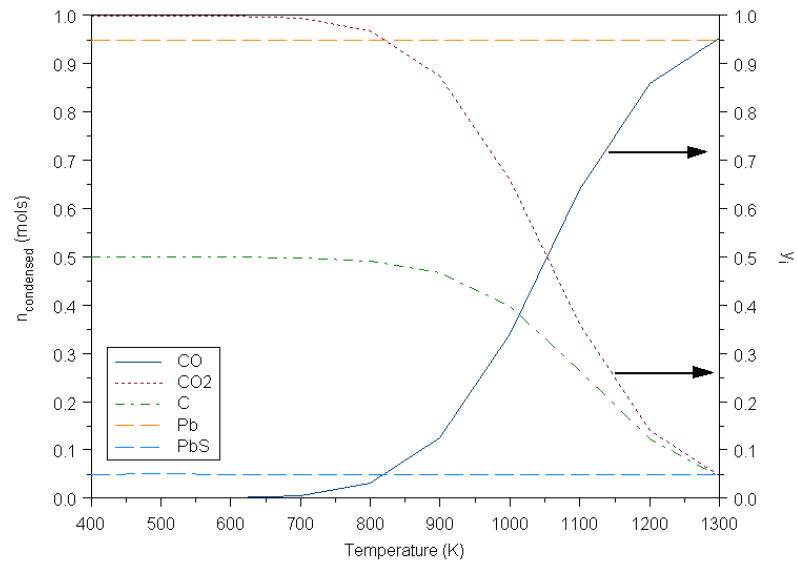


Figure C 12: Equilibrium composition of a system of C=1mol; S=0.05mol; O=1mol; Pb=1mol at 10bar

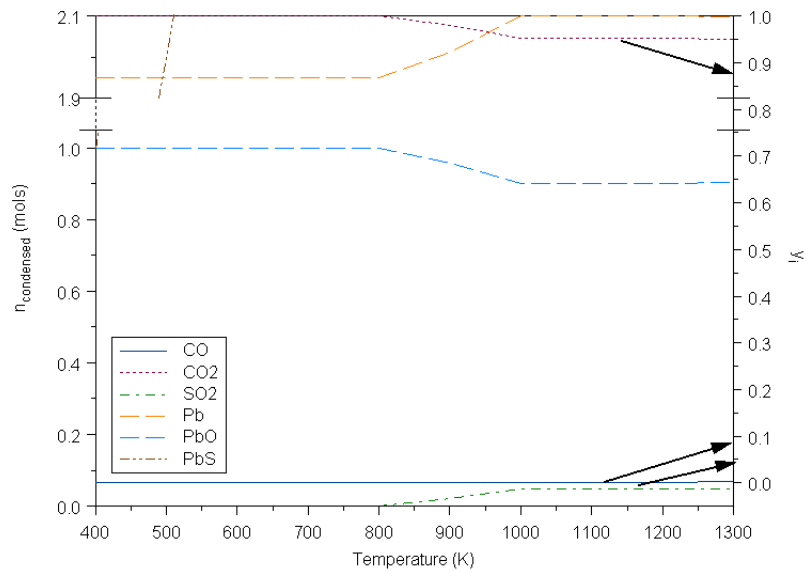


Figure C 13: Equilibrium composition of a system of C=1mol; S=0.05mol; O=3mol; Pb=3mol at 0.1bar

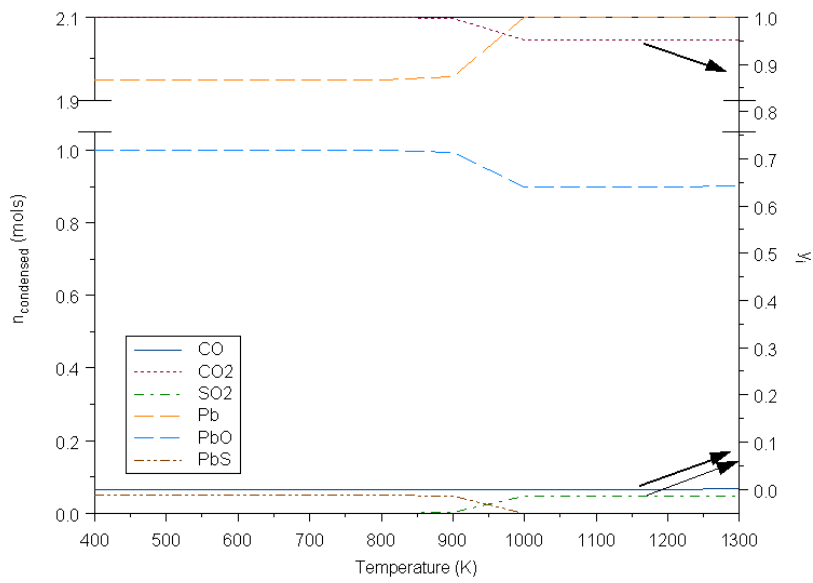


Figure C 14: Equilibrium composition of a system of C=1mol; S=0.05mol; O=3mol; Pb=3mol at 1bar

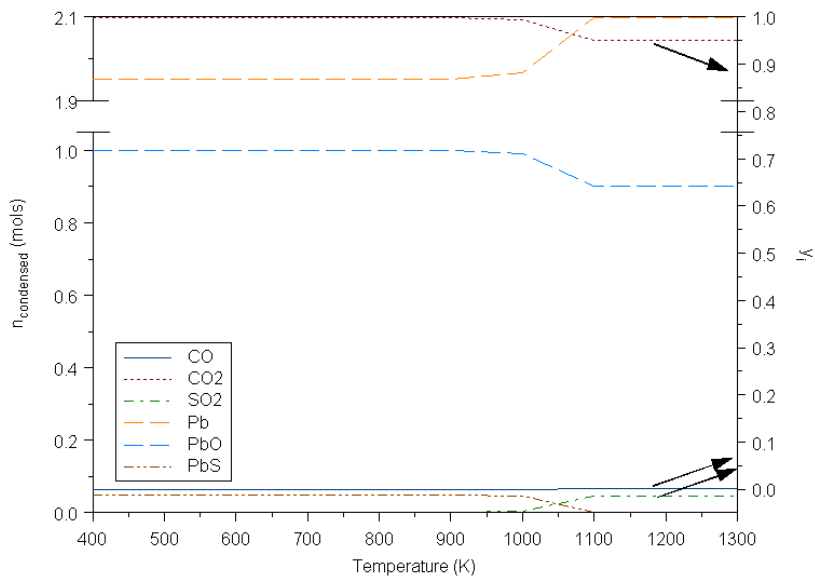


Figure C 15: Equilibrium composition of a system of C=1mol; S=0.05mol; O=3mol; Pb=3mol at 10bar

3. C-S-O-Co SYSTEM

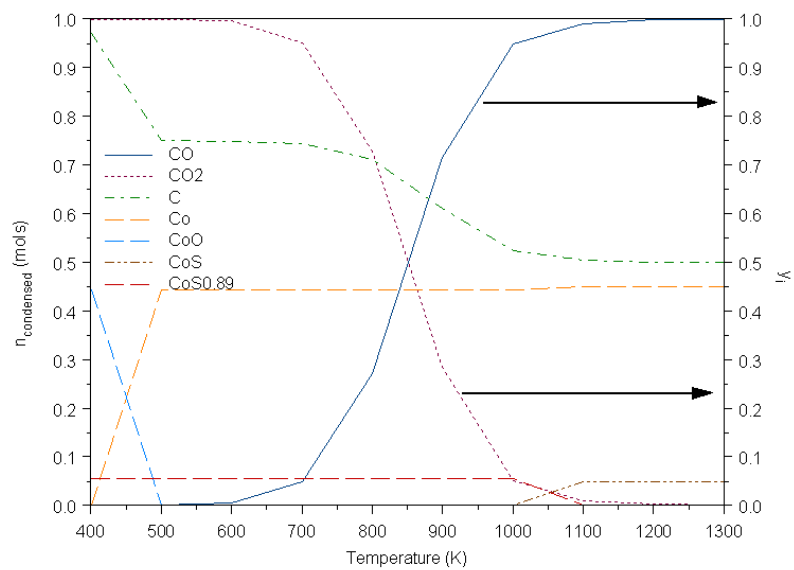


Figure C 16: Equilibrium composition of a system of C=1mol; S=0.05mol; O=0.5mol; Co=0.5mol at 0.1bar

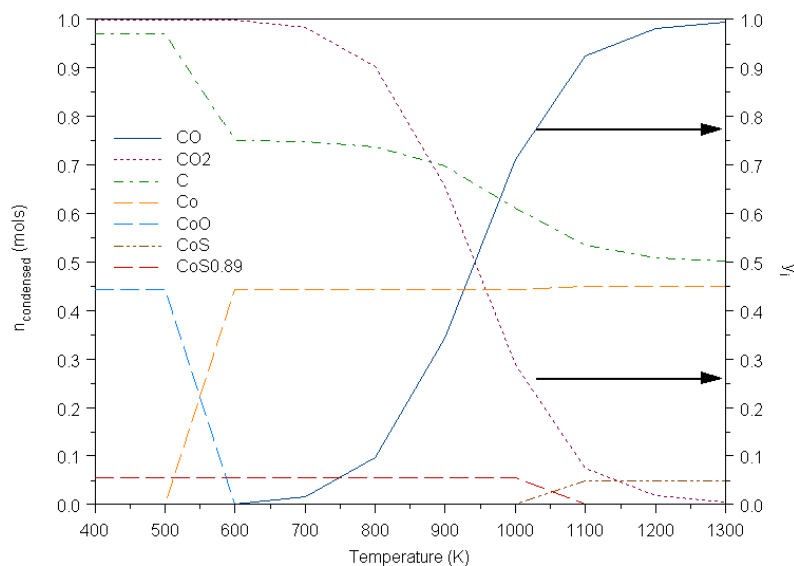


Figure C 17: Equilibrium composition of a system of C=1mol; S=0.05mol; O=0.5mol; Co=0.5mol at 1bar

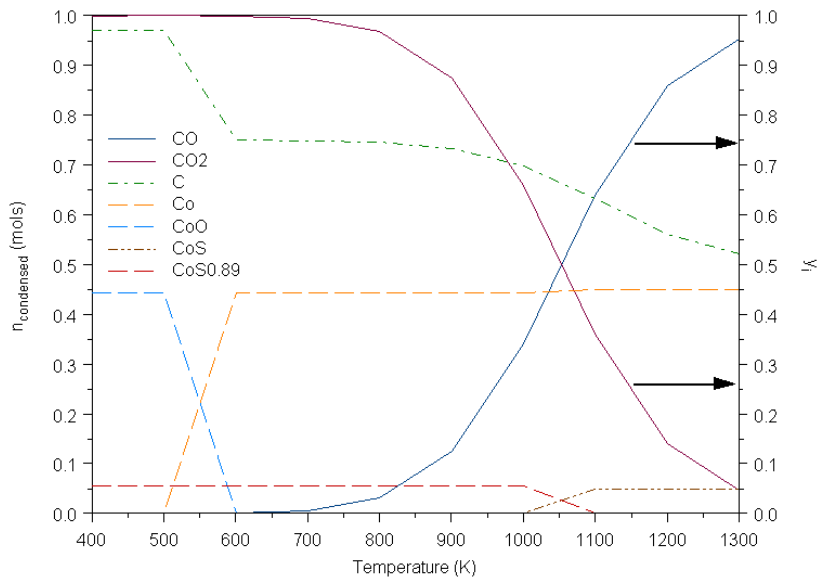


Figure C 18: Equilibrium composition of a system of C=1mol; S=0.05mol; O=0.5mol; Co=0.5mol at 10bar

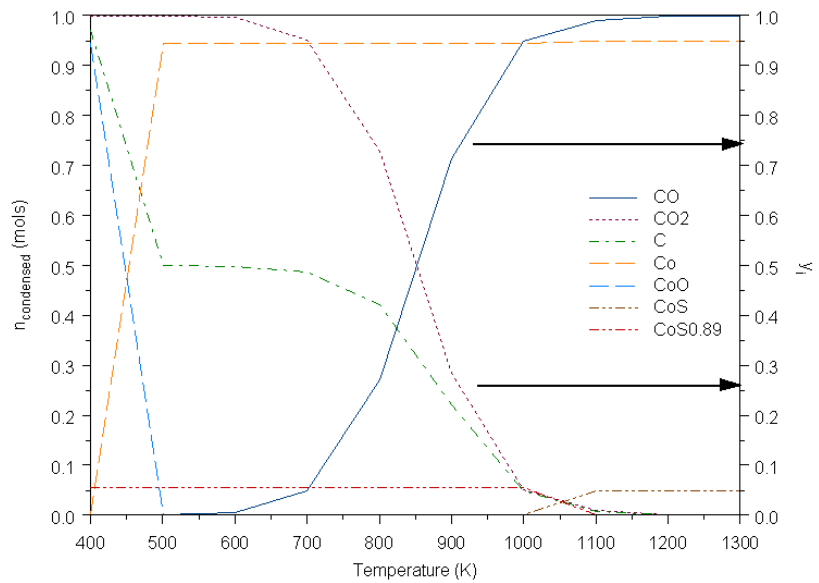


Figure C 19: Equilibrium composition of a system of C=1mol; S=0.05mol; O=1mol; Co=1mol at 0.1bar

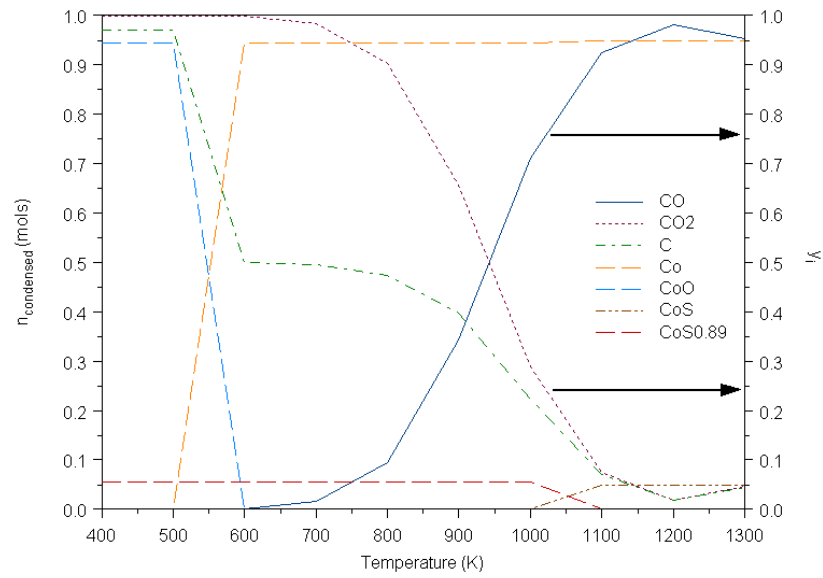


Figure C 20: Equilibrium composition of a system of C=1mol; S=0.05mol; O=1mol; Co=1mol at 1bar

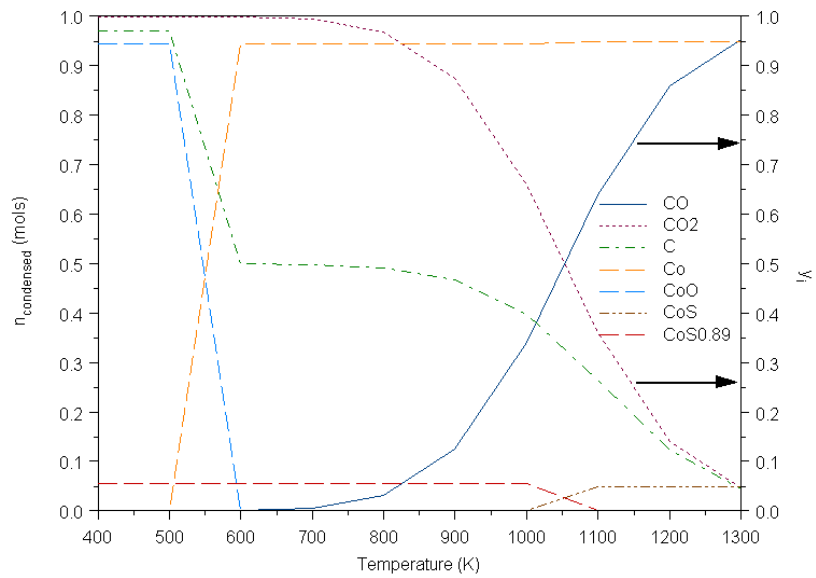


Figure C 21: Equilibrium composition of a system of C=1mol; S=0.05mol; O=1mol; Co=1mol at 10bar

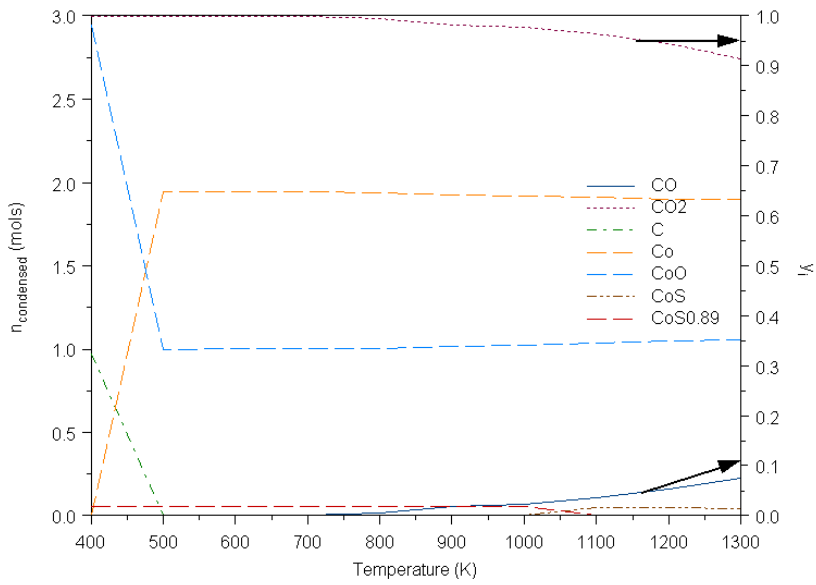


Figure C 22: Equilibrium composition of a system of C=1mol; S=0.05mol; O=3mol; Co=3mol at 0.1bar

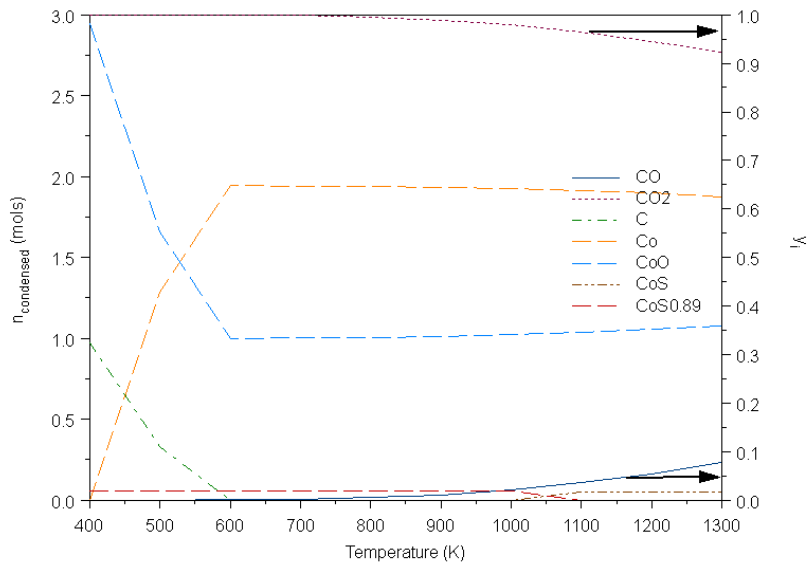


Figure C 23: Equilibrium composition of a system of C=1mol; S=0.05mol; O=3mol; Co=3mol at 1bar

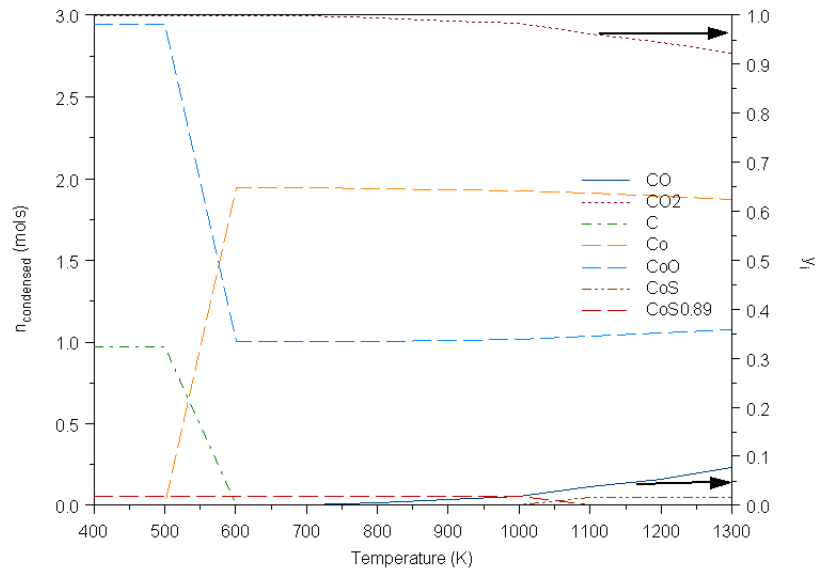


Figure C 24: Equilibrium composition of a system of C=1mol; S=0.05mol; O=3mol; Co=3mol at 10bar

4. C-S-O-Fe SYSTEM

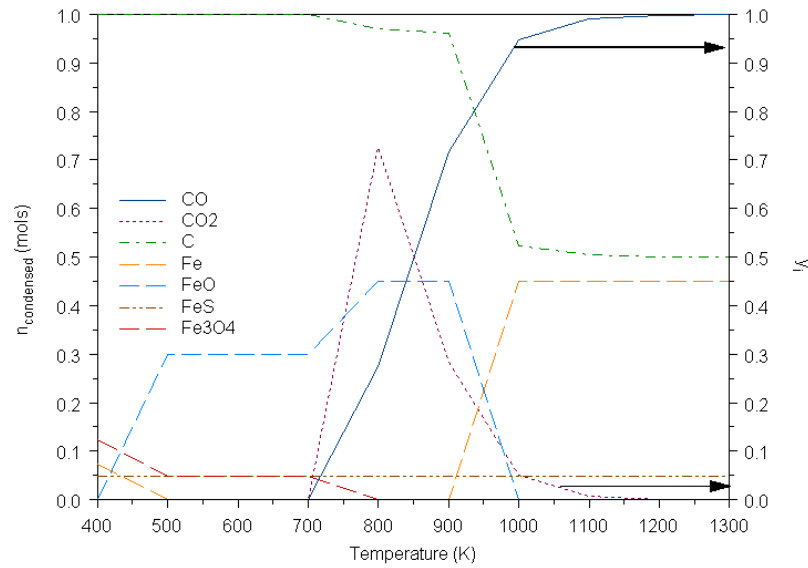


Figure C 25: Equilibrium composition of a system of C=1mol; S=0.05mol; O=0.5mol; Fe=0.5mol at 0.1bar

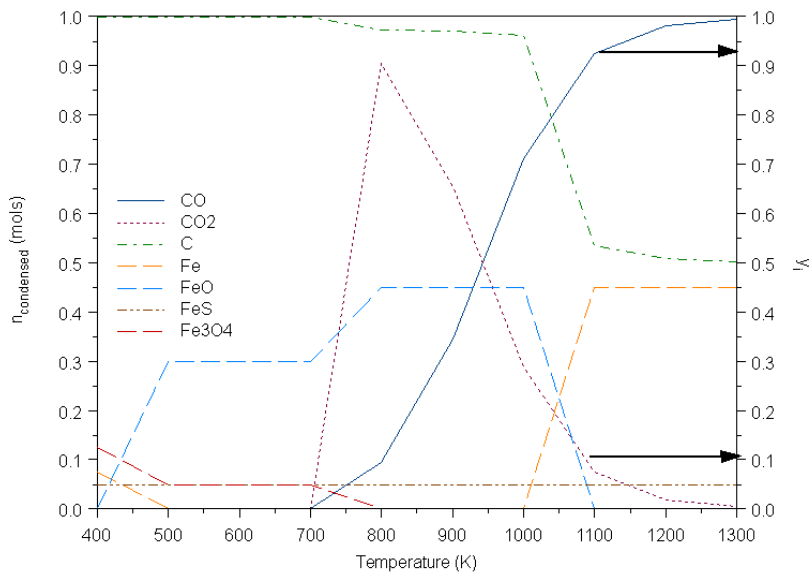


Figure C 26: Equilibrium composition of a system of C=1mol; S=0.05mol; O=0.5mol; Fe=0.5mol at 1bar

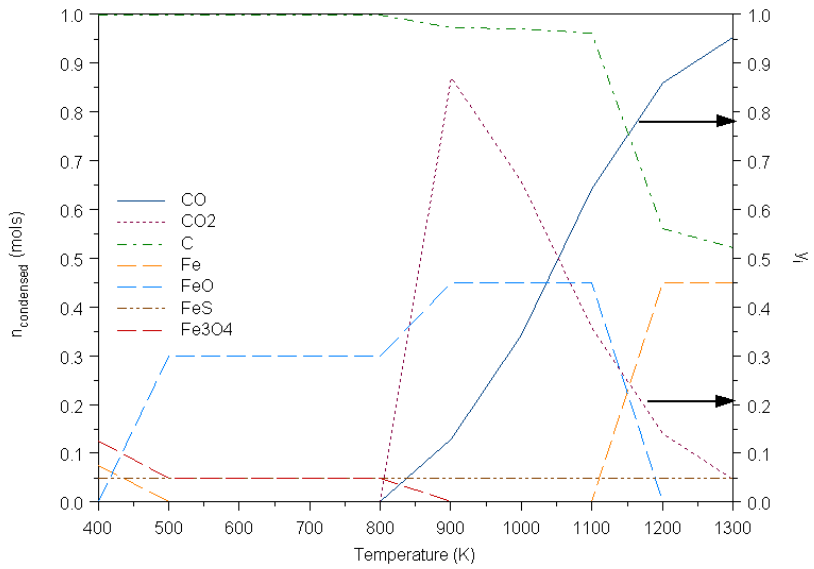


Figure C 27: Equilibrium composition of a system of C=1mol; S=0.05mol; O=0.5mol; Fe=0.5mol at 10bar

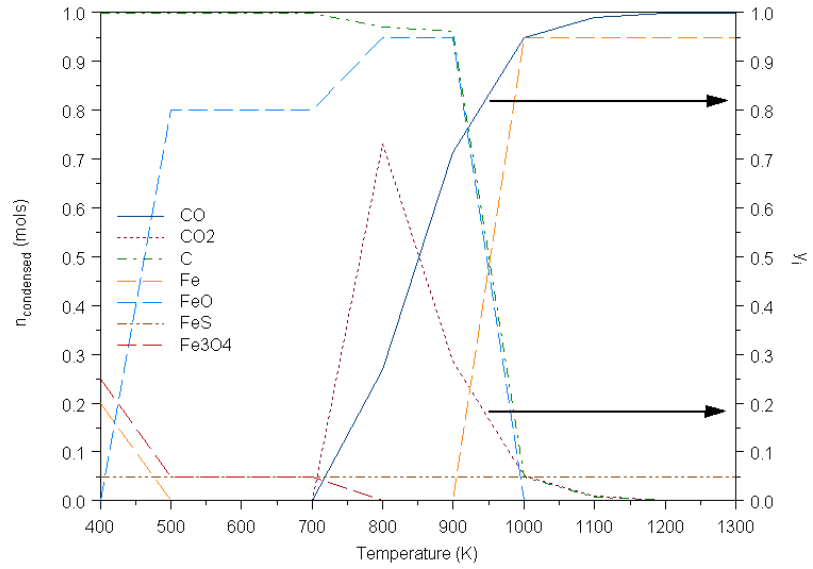


Figure C 28: Equilibrium composition of a system of C=1mol; S=0.05mol; O=1mol; Fe=1mol at 0.1bar

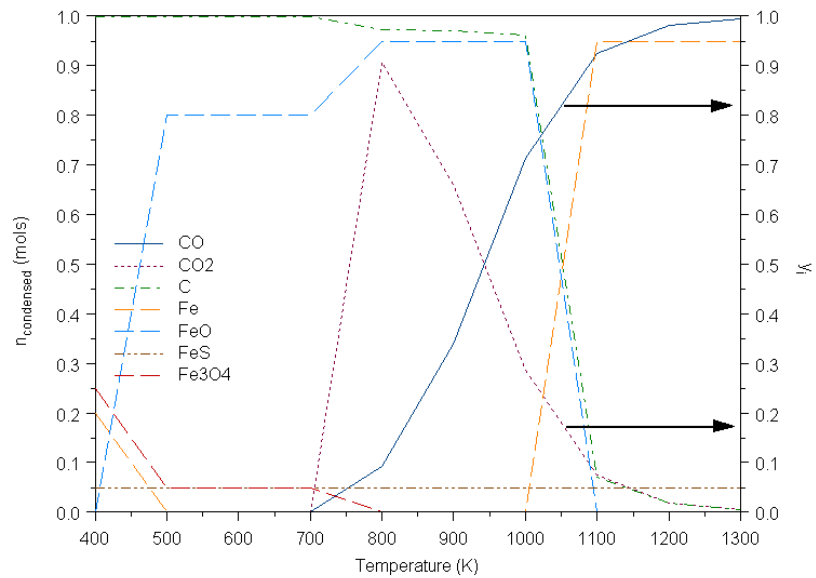


Figure C 29: Equilibrium composition of a system of C=1mol; S=0.05mol; O=1mol; Fe=1mol at 1bar

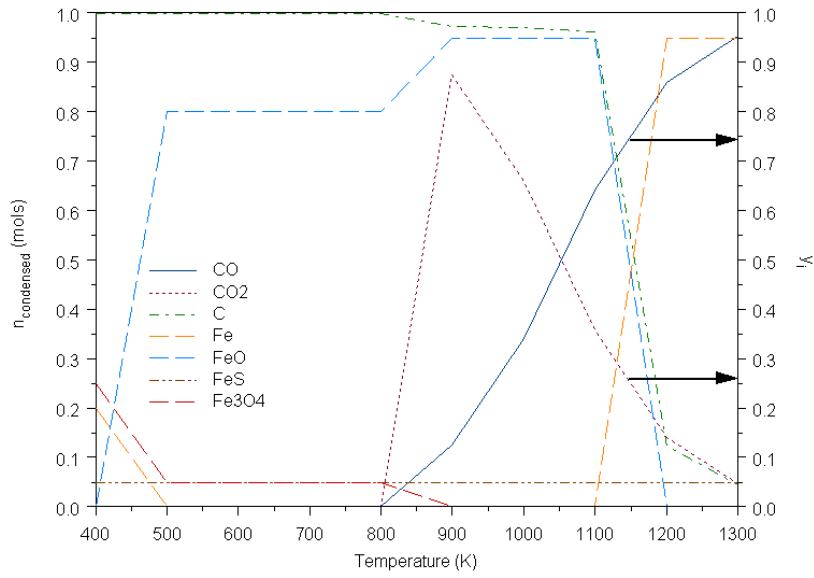


Figure C 30: Equilibrium composition of a system of C=1mol; S=0.05mol; O=1mol; Fe=1mol at 10bar

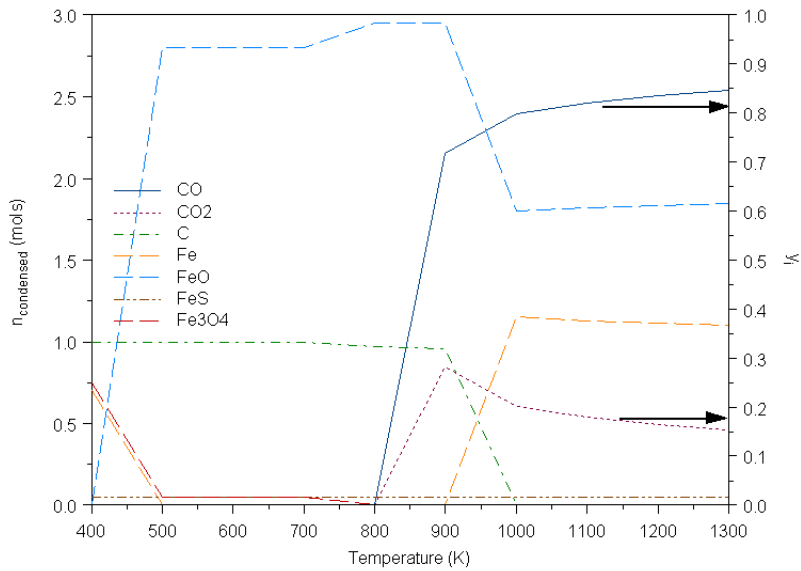


Figure C 31: Equilibrium composition of a system of C=1mol; S=0.05mol; O=3mol; Fe=3mol at 0.1bar

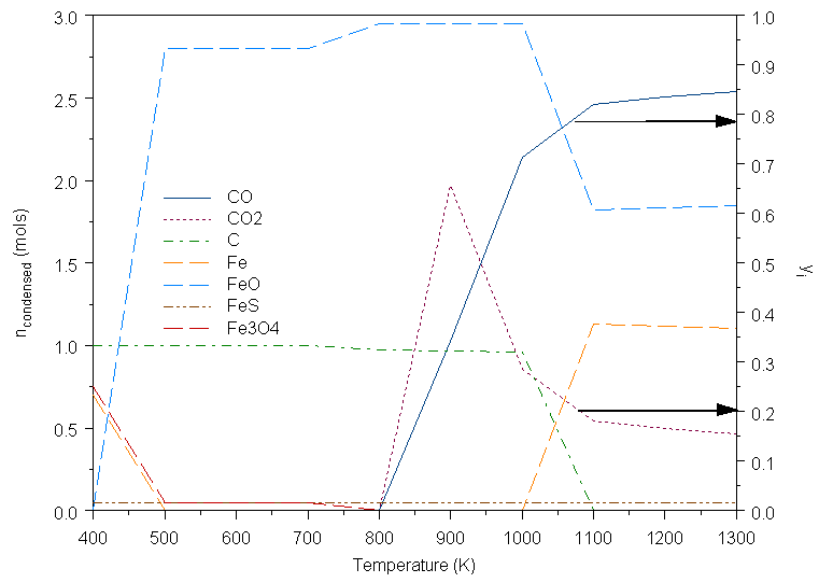


Figure C 32: Equilibrium composition of a system of C=1mol; S=0.05mol; O=3mol; Fe=3mol at 1bar

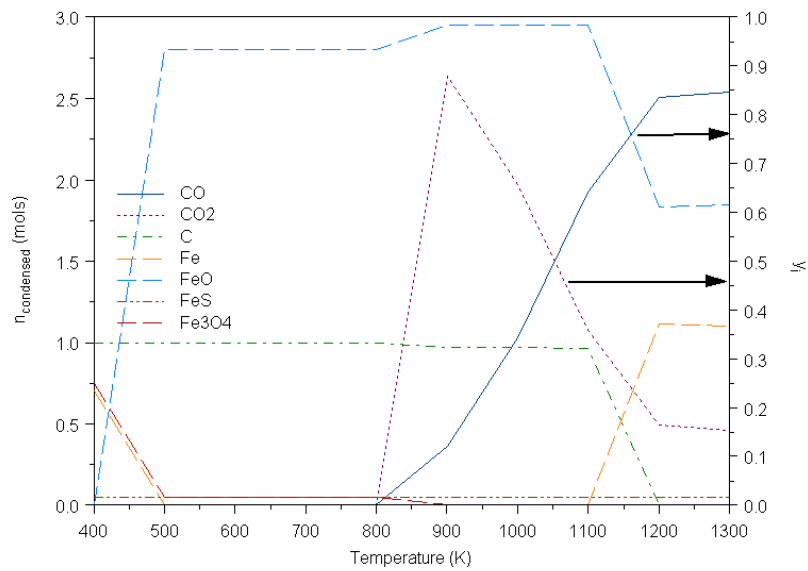


Figure C 33: Equilibrium composition of a system of C=1mol; S=0.05mol; O=3mol; Fe=3mol at 10bar

APPENDIX D

REACTOR DESIGN

Observing performance on relatively big lab scale reactors is important for predicting the problems during scaling up. Therefore, two prototype reactors were manufactured and operated. First reactor, Reactor A, was designed and manufactured as shown in Figure D1. During its design, discharging bath material after operation was mainly concerned. Thus, bottom part was manufactured with 7° slope. Reactor A has one inlet and one outlet lines. Inlet line has a longer length than outlet one since the idea is to supply oxidizing medium as much as closer to the surface of the molten metal bath. This reactor was mainly used for primary experiments. Thereafter, a new reactor, Reactor B, was designed and manufactured due to problems related with sealing and internal lack of temperature measurement in Reactor A. Reactor B is the second generation reactor as shown in Figure D2. During the design period, experience coming from reactor A was mainly used. Flanged cover was designed. An additional hole was drilled for thermocouple insertion. Then, a heat resistance gasket (<1300°C) was used for sealing purposes. Evacuation was mainly done by turning the bottom part upside down and heating it in order to melt the solidified metal.

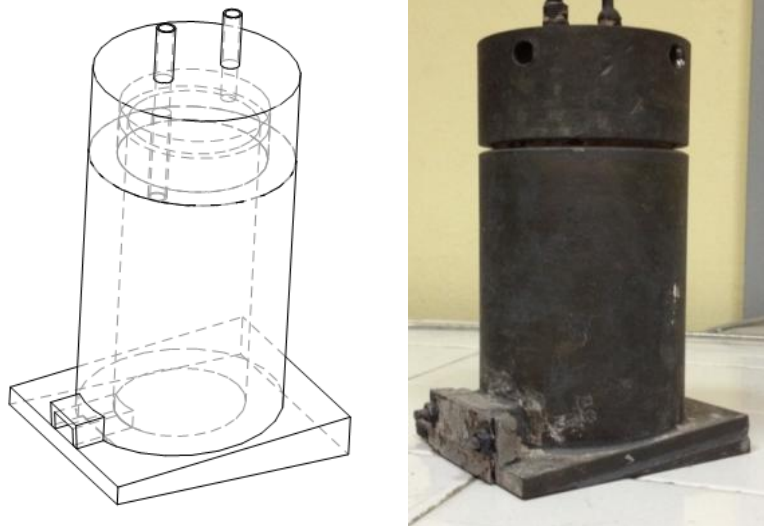


Figure D 1: Technical drawing and manufactured picture of Reactor A

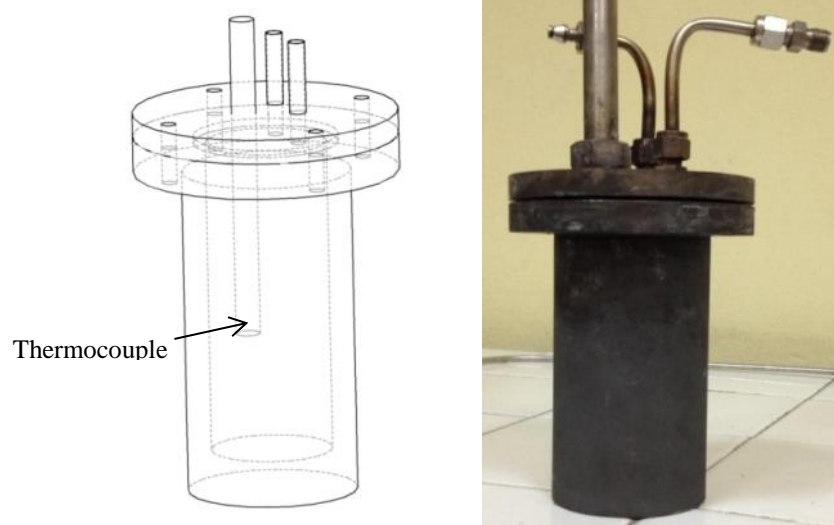


Figure D 2: Technical drawing and manufactured picture of Reactor B.

APPENDIX E

VISUAL ANALYSIS OF LEAD OXIDATION

New system shown in Figure E1 was prepared for testing metallic lead oxidation performance at air and steam atmosphere by the help of gained information from the system shown in Figure 15. This system could be operated for oxidation by air and vapor. Line 1 is used for air oxidation by air pump whereas line 2 is operated for steam oxidation. 230gr technical grade lead rods were put into the reactor for each experiment. Oxidation by air experiments air pump was started at maximum rate. Then, reactor was heated with 8°C/min. Nevertheless, sweeping gas (N₂) flow rate was adjusted to 100ccpm for oxidation by steam experiments. Water vapor generator temperature was set to 80°C. Reactor was heated at a rate of 8°C/min.

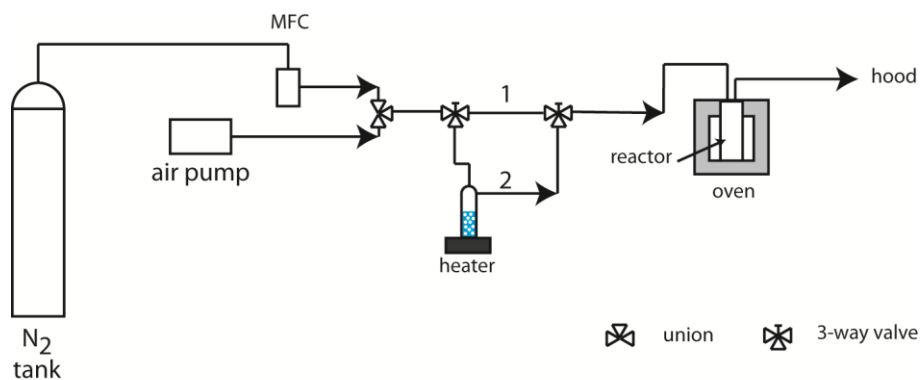


Figure E 1: Water oxidation experiment with Reactor A.

APPENDIX F

MASS SPECTROMETRY EXPERIMENTS

1. Experimental Setup

1.1. CO₂ Reduction Experiments

CO₂ reduction experiments were done by designing a discontinuous measurement methodology for mass spectrometry. A sampling system shown in Figure 22 was designed for this purpose. Experiments were done by following evacuation of sampling loop, product stream sampling, and carrying sampling gas for measurement steps for each measurement. Evacuation of sampling loop was done by isolating lines between valves 2, 3, 6, and 9. Then, vacuum pump was started by opening valve 9. Outflow is mixed with reactor outlet and is sent off to hood. Total evacuation time was determined as 1 minute. Thereafter, valve 9 was closed and vacuum pump was stopped for sampling step. An appropriate amount from reactor outlet was taken to the sampling loop at vacuum by opening valve 2. Sampling step lasted around 1 minute. Finally, valve 2 was closed and valve 6 was opened respectively for sweeping sampling gas to the MS. Carrier gas was selected as Ar. Time required for sweeping period was determined as 8 min. It was seen that this time was enough for signal to come baseline again.

Reactor was filled with lead weighed as 290g technical grade. In addition, flow rates were determined as 30ccpm for Ar and 10ccpm for CO₂. Heating period was determined as 20mins for 100°C, 20mins for 250°C, 20mins for 400°C, 20mins for 500°C, 20mins for 600°C, 20mins for 700°C, 30 min for 800°C and stay there for 1h.

1.2. Lead Oxide Decomposition Experiments

Decomposition experiment of formed lead oxide produced in section 3.2.7.1 was done at Ar atmosphere. Procedure was started with cooling the formed oxides at CO₂ atmosphere in order to prevent unwanted decomposition. After reaching room temperature, next heating period was started at Ar atmosphere with same procedure in Figure 22. Nevertheless, at this time CO₂ tube connection was replaced with an additional connection coming from Ar tube. Sweep gas flow rate was adjusted as 30ccpm Ar whereas reactor fed gas was adjusted as 15ccpm Ar. Similar heating period with CO₂ reduction was applied as 20mins for 100°C, 20mins for 250°C, 20mins for 400°C, 20mins for 500°C, 20mins for 600°C, 20mins for 700°C, 30 min for 800°C and 1 hour to 920°C.

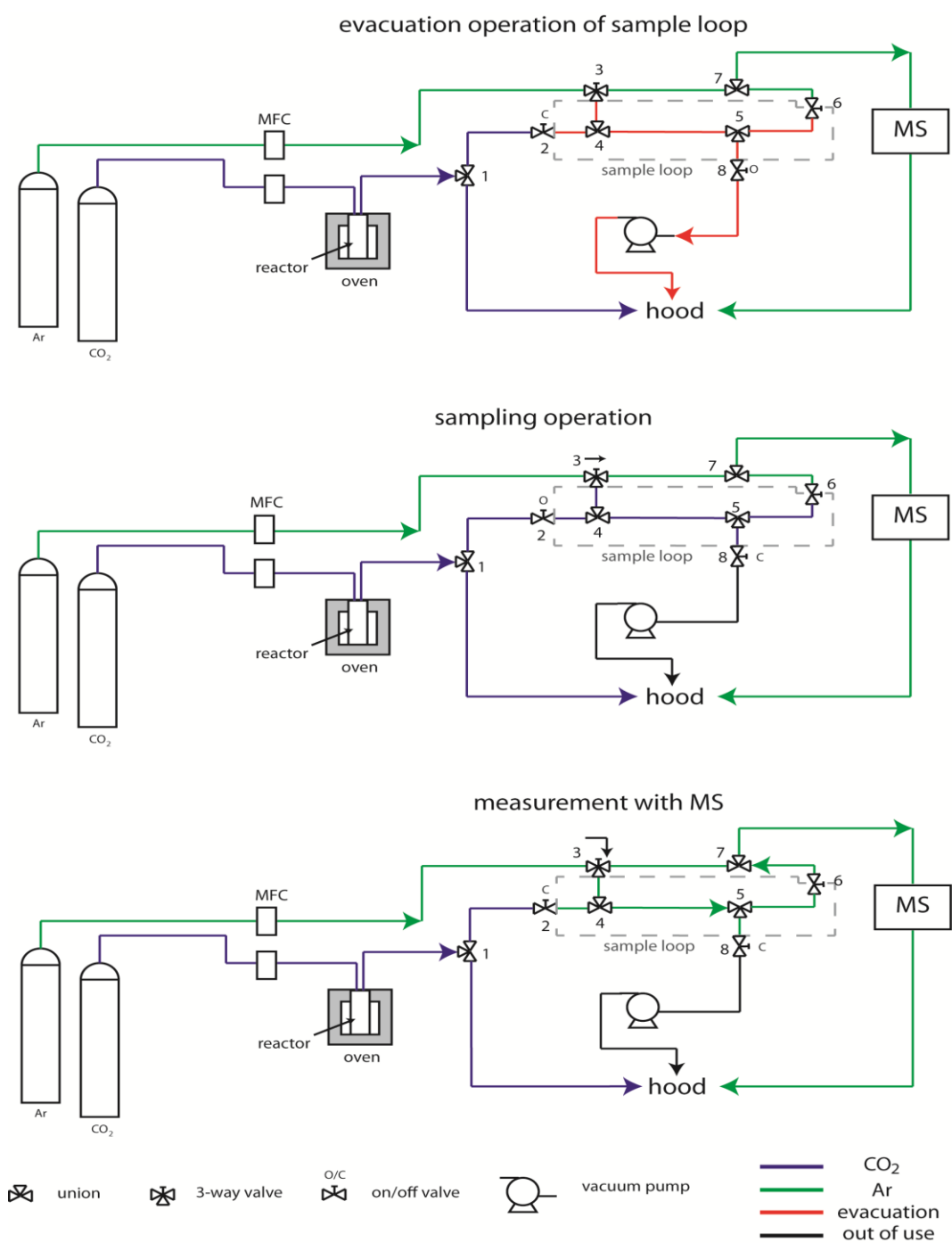


Figure F 1: MS setup for discontinuous experiment

2. Results

2.1. CO₂ Reduction

16 samples were taken during the experiment between 250°C to 800°C. Sample chamber pressure of MS was tried to be stabilized between 1.5E-5torr and 2.8E-5torr range. Obtained raw data was integrated by using Simpson's 1/3 rule. Then, concentration ratio of each sampled gas is calculated by estimated area under the curves. Results are shown in Figure F2.

It is hard to find a quantitative conclusion from MS calculations. Nevertheless, it definitely gives an idea about CO and CO₂ trendlines. It is found that as lead can reduce CO₂ to oxidize itself. In addition, CO becomes more favorable as temperature increases. Break-even point was observed at ~500°C (~780K). In addition, decrease in CO₂ concentration which is missing link of FT-IR analysis was observed.

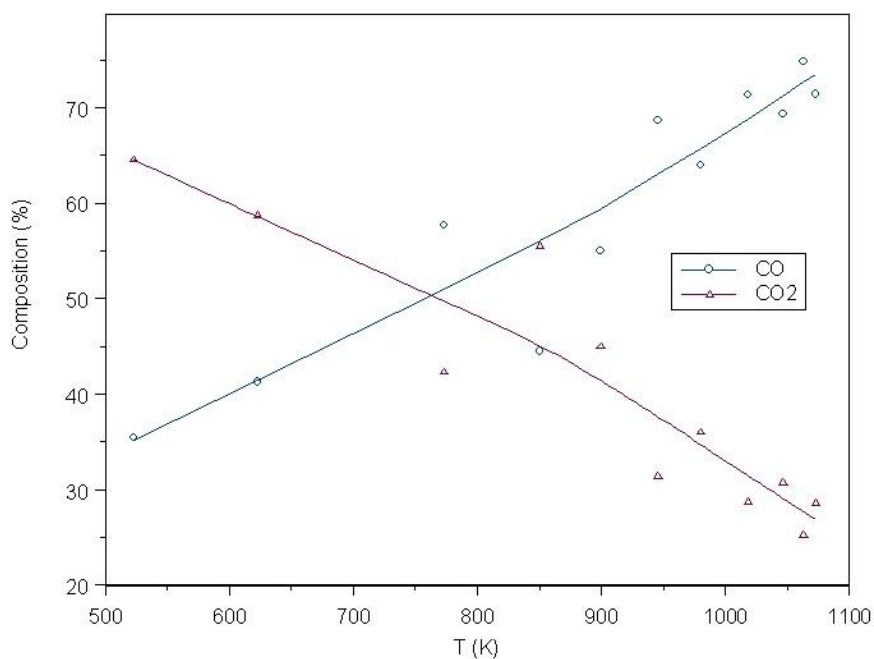


Figure F 2: CO₂ reduction as temperature increases.

Results of CO₂ reduction experiments conclude that lead oxidation by CO₂ reduction can be achieved as temperature increases. The CO formation mainly becomes favorable after 600°C. These main conclusions verify that as temperature increases metallic lead can reduce CO₂ to oxidize itself in thermodynamic point of view.

2.2. Thermal Decomposition of Lead Oxide

22 samples were taken during the experiment between 100°C to 920°C. Sample chamber pressure were tried to be stabilized around ~1.8E-5torr. Obtained raw data analyzed by using Simpson's 1/3 rule. Then, concentration ratio of each sampled gas is calculated by estimated area under the curves. Results are shown in Figure F3. As stated in thermodynamic analysis section, thermal decomposition temperatures for PbO₂ is around 290°C while 370°C for Pb₂O₃. O₂ ratio in product stream increases between 250°C and 400°C. Nevertheless, same is not true for PbO since decomposition temperature is around 1470°C. Previous visual experiments showed that as the temperature gets closer to melting temperature of PbO, surface relaxation during phase transformation from solid to liquid results with decomposition. Therefore, concentration variance after 800°C can be explained by thermal decomposition of PbO to metallic Pb.

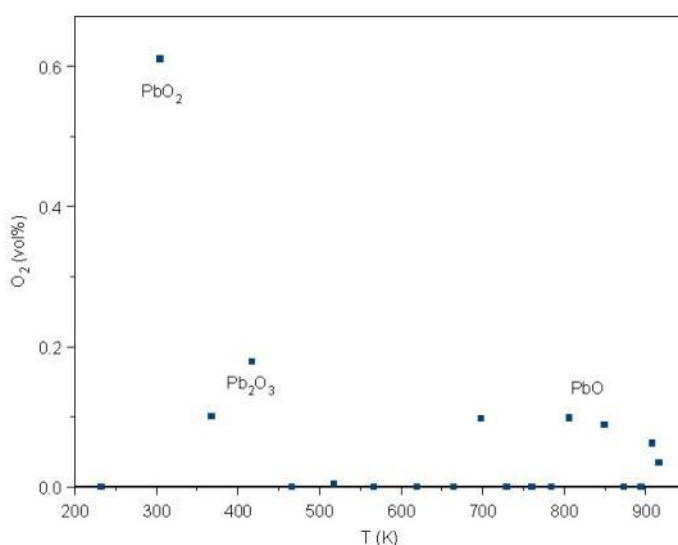


Figure F 3: Thermal Decomposition of lead oxide formed by CO₂ reduction experiment.

APPENDIX G

TPD ANALYSIS

Various materials were synthesized. Their characterization results were shown in Figure G1 and G2. Oxygen release behaviors were observed using a thermal conductivity detector up to 850°C. During the experiment, it was assumed that studied materials are pure metal oxides forms. Therefore, all signal changes were due to thermal decomposition of metal oxides.

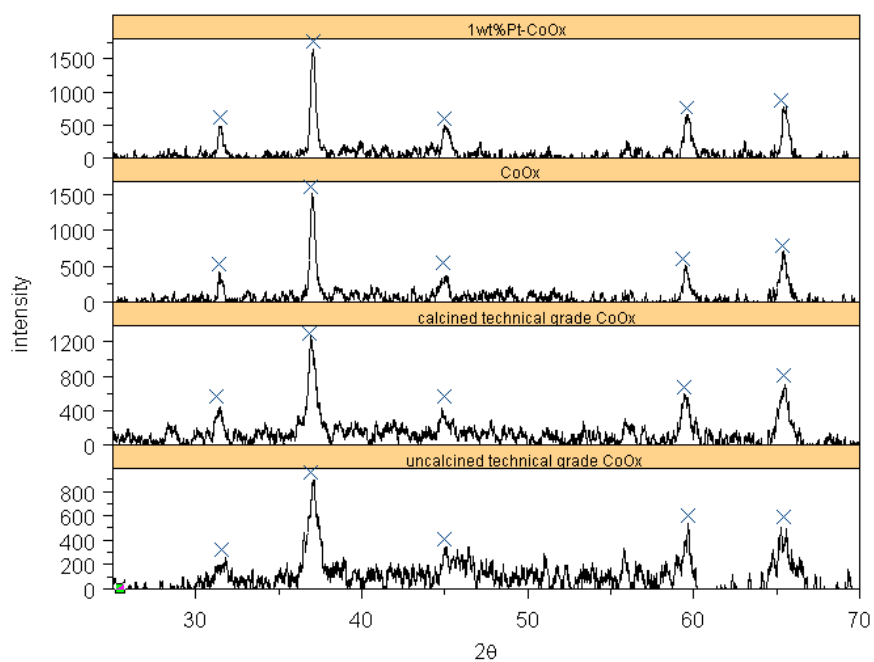


Figure G 1: X-ray diffraction data of technical grade and synthesize cobalt oxides.

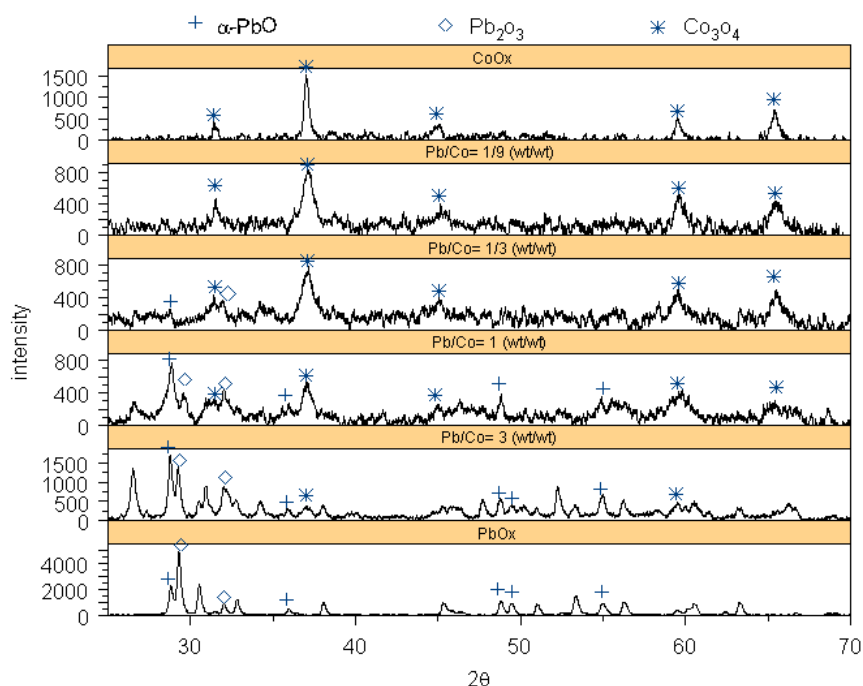


Figure G 2: X-ray diffraction data of synthesized lead oxide, cobalt oxide and their mixed oxides.

Thermal decomposition performance of cobalt oxides were shown in Figure G3. Technical grade cobalt oxide supplied from EgeFerro was examined as uncalcined and calcined forms. It was found that increase in absorbance at low temperatures were mainly due to organic impurities that technical grade has. Therefore, absorbance in this region was neglected for further calculations. When moderate temperature zone was mainly concerned, it was seen that CoOx addition to Al₂O₃ decreased decomposition temperature. This behavior can be explained by formation cobalt aluminates. In addition, this temperature can be further decreased by addition of Pt due to the increase in active sites. At high temperature zone between 700°C and 850°C, sharp peaks were observed. Highest peak was observed CoOx synthesized from cobalt nitrates. Then, by addition of Pt on this CoOx a small decrease in decomposition temperature was observed. It was also seen that calcined and uncalcined technical grade cobalt oxides showed nearly same peak decomposition temperatures but relatively low peaks.

Cobalt and lead mixed oxides were analyzed by same decomposition experimental setup. Arbitrary mixing ratios were determined and materials were synthesized. Thermal decomposition results are shown in Figure G4. Pure lead oxide which was directly synthesized from lead acetate started to decompose at lower temperatures. Nevertheless, its decomposition rate did not give any peak temperature. By addition of cobalt into lead oxide, an increase in absorbance was observed at higher temperatures as compared with PbOx due to possible synergetic effect. Mixed material graphs were smooth mixture of pure PbOx and CoOx graphs. Thus, no distinct phase separation was observed.

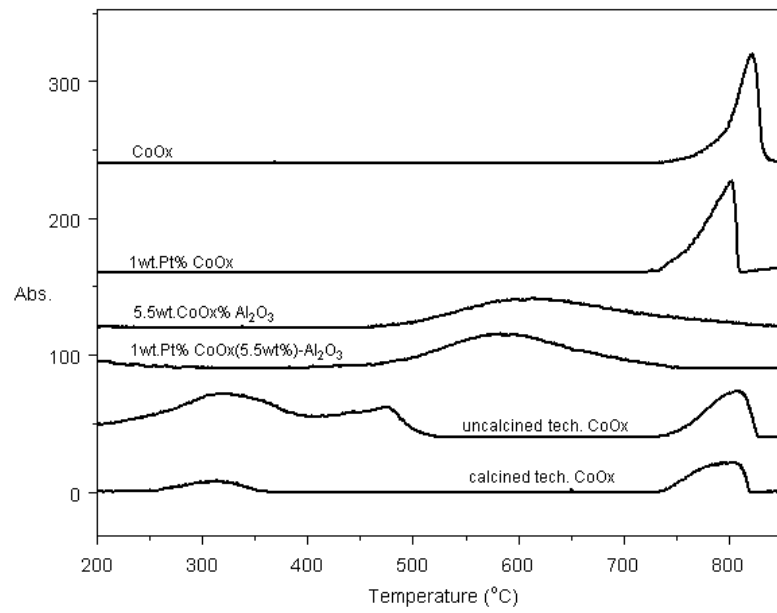


Figure G 3: Thermal decomposition of synthesized cobalt based looping material.

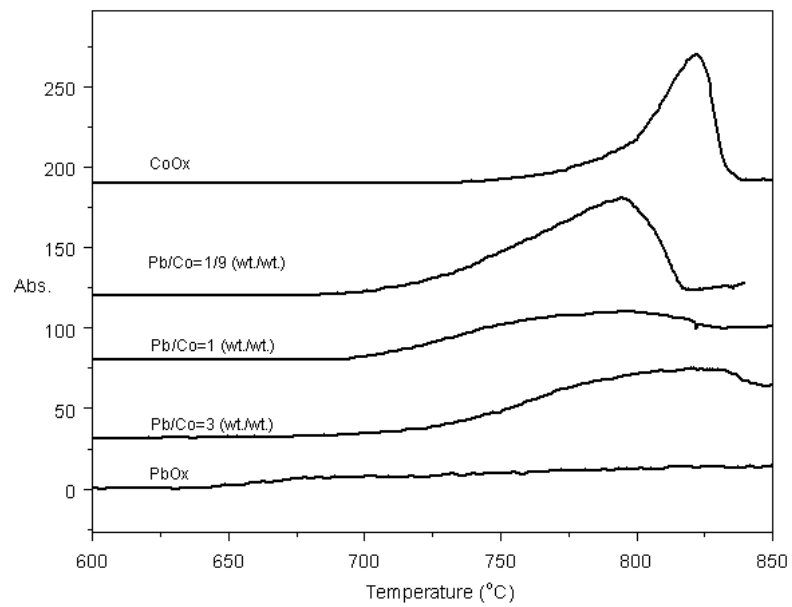


Figure G 4: Thermal decomposition of synthesized Pb/Co mixed looping material.

Important points about the tendency of thermal decomposition performance of studied materials were shown in Figure G3 and G4. Nevertheless, these provided data should be converted to comparable levels in order to find the best material when decomposition was the concern. Therefore, areas under the curve for all graphs were calculated by Simpson's rule and their absorbance value was divided to available oxygen in the material. As it was seen from Table G2, lead oxide was better when oxygen release was concerned. In addition, pure lead oxide supplied three times higher oxygen when compared with cobalt oxide. Presence of the synergetic effect after mixing cobalt and lead oxides was also observed from Table G2. High synergy was achieved when Pb/Co=3 (wt./wt.) whereas lowest one was at Pb/Co=1/9 (wt./wt.).

Table G 1: Performance analysis of all looping material

Looping Material	Peak Temperature (°C)	Amount of Oxygen available, mg(A)	O₂ peak area (a.u) (PA)	(PA)/(A)
PbO _x	NA	5.19	5139	990
Pb/Co=1 (wt./wt.)	790	8.43	7734	917
Pb/Co=3 (wt./wt.)	820	6.01	11163	1857
Pb/Co=1/9 (wt./wt.)	790	12.31	7409	602
Uncalcined tech. CoO _x	800	13.28	3462	261
Calcined tech. CoO _x	800	13.28	3374	254
5.5wtCoO _x % Al ₂ O ₃	600	22.97	8334	363
1wtPt% CoO _x (5.5wt%)-Al ₂ O ₃	575	22.51	8544	657
CoO _x	820	13.28	4976	375
1wtPt% CoO _x	780	13.01	5003	377